KAZAN FEDERAL UNIVERSITY
INSTITUTE OF PHYSICS
Radioelectronics department

DIELECTRIC RELAXATION PHENOMENA IN COMPLEX SYSTEMS

Tutorial

Yu. Feldman, Yu.A. Gusev, M.A.Vasilyeva

Kazan
2012

Печатается по решению Редакционно-издательского совета ФГАОУВПО «Казанский (Приволжский) федеральный университет»

методической комиссии Института физики
Протокол № __ от «__» _____ 2012 г.

заседания кафедры радиоэлектроники
Протокол № 2 от «01» октября 2012 г.

Авторы-составители
Yu. Feldman, Yu.A. Gusev, M.A.Vasilyeva

Научный редактор
д.ф.-м.н., проф. М.Н. Овчинников
Рецензент
д.х.н., проф. Ю.Ф. Зуев
Рецензент
к.ф.-м.н., доц. И.А. Насыров

Title: Dielectric Relaxation Phenomena in Complex Systems: Tutorial / Yu. Feldman, Yu.A. Gusev, M.A.Vasilyeva. – Kazan: Kazan University, 2012. – p. 134.

In the writing of this tutorial we have not sought to cover every aspect of the dielectric relaxation of complex materials. The aim of this work to demonstrate the usefulness of dielectric spectroscopy for such systems, using its application on select examples as illustrations. This tutorial will be helpful to students, graduate students and others who are interested in the dielectric spectroscopy of complex systems.

Contents

1 Introduction

Recent years have witnessed extensive research of soft condensed matter physics to investigate the structure, dynamics, and macroscopic behavior of *complex systems* (*CS*). *CS* are a very broad and general class of materials that are typically non-crystalline. Polymers, biopolymers, colloid systems (emulsions and microemulsions), biological cells, porous materials, and liquid crystals can all be considered as *CS*. All of these systems exhibit a common feature: the new "*mesoscopic*" length scale, intermediate between molecular and macroscopic. The dynamic processes occurring in *CS* include different length and time scales. Both fast and ultra-slow molecular rearrangements take place within the microscopic, mesoscopic and macroscopic organization of the systems. A common theme in *CS* is that while the materials are disordered at the molecular scale and homogeneous at the macroscopic scale, they usually possess a certain amount of order at an intermediate, so-called mesoscopic, scale due to a delicate balance of interaction and thermal effects. Simple exponential relaxation law and the classical model of Brownian diffusion cannot adequately describe the relaxation phenomena and kinetics in such materials. This kind of non-exponential relaxation behavior and anomalous diffusion phenomena is today called “strange kinetics” [1,2]. Generally, the complete characterization of these relaxation behaviors requires the use of a variety of techniques in order to span the relevant ranges in frequency. In this approach, *Dielectric Spectroscopy* (*DS*) has its own advantages. The modern *DS* technique may overlap extremely wide frequency (10^{-6} to 10^{12} Hz), temperature (- 170 °C to +500 °C) and pressure ranges [3-5]. *DS* is especially sensitive to intermolecular interactions and is able to monitor cooperative processes at the molecular level. Therefore, this method is more appropriate than any other to monitor such different scales of molecular motions. It provides a link between the investigation of the properties of the individual constituents of the complex material via molecular spectroscopy and the characterization of its bulk properties.

This tutorial concentrates on the results of *DS* study of the structure, dynamics, and macroscopic behavior of complex materials. First, we present an introduction to the basic concepts of dielectric polarization in static and time dependent fields, before the Dielectric Spectroscopy technique itself is reviewed both for frequency and time domains. This part has three sections, i.e. Broad Band Dielectric Spectroscopy, Time Domain Dielectric Spectroscopy and a section where different aspects of data treatment and fitting routines are discussed in detail. Then, some examples of dielectric responses observed in various disordered materials are presented. Finally, we will consider the experimental evidence of

non-Debye dielectric responses in several complex disordered systems such as microemulsions, porous glasses, porous silicon, H-bonding liquids, aqueous solutions of polymers and composite materials.

2 Dielectric Polarization, Basic Principles

2.1 Dielectric Polarization in Static Electric Fields

When placed in an external electric field $\boldsymbol{E}$, a dielectric sample acquires a non-zero *macroscopic dipole moment*. This means that the dielectric is polarized under the influence of the field. The *polarization* $\boldsymbol{P}$ of the sample, or dipole density, can be presented in a very simple way

$$\boldsymbol{P} = \frac{\langle \boldsymbol{M} \rangle}{V}, \tag{2.1}$$

where $<\boldsymbol{M}>$ is the macroscopic dipole moment of the whole sample volume V, which is formed by the permanent micro dipoles (i.e. coupled pairs of opposite charges) as well as by dipoles that are not coupled pairs of micro charges within the electro neutral dielectric sample. The brackets < > denote ensemble average. In a linear approximation the macroscopic polarization of the dielectric sample is proportional to the strength of the applied external electric field $\boldsymbol{E}$ [6]:

$$P_i = \varepsilon_0 \chi_{ik} E_k \ , \tag{2.2}$$

where χ_{ik} is *the tensor of the dielectric susceptibility* of the material and ε_0 =8.854·10^{-12} [F·m^{-1}] is the dielectric permittivity of the vacuum. If the dielectric is isotropic and uniform, χ is a scalar and equation (2.2) will be reduced to the more simple form:

$$\boldsymbol{P} = \varepsilon_0 \chi \boldsymbol{E} \ . \tag{2.3}$$

According to the macroscopic Maxwell approach, matter is treated as a continuum, and the field within the matter in this case is the direct result of electrical displacement (electrical induction) vector $\boldsymbol{D}$, which is the electric field corrected by polarization [7]:

$$\boldsymbol{D} = \varepsilon_0 \boldsymbol{E} + \boldsymbol{P}. \tag{2.4}$$

For an uniform isotropic dielectric medium, the vectors $\boldsymbol{D}, \boldsymbol{E}, \boldsymbol{P}$ have the same direction, and the susceptibility is coordinate-independent, therefore

$$\boldsymbol{D} = \varepsilon_0(1+\chi)\boldsymbol{E} = \varepsilon_0\varepsilon\boldsymbol{E} \quad , \tag{2.5}$$

where $\varepsilon = 1+\chi$ is the relative ***dielectric permittivity***. Traditionally, it is also called the dielectric constant, because in a linear regime it is independent of the field strength. However, it can be a function of many other variables. For example in the case of time variable fields it is dependent on the frequency of the applied electric field, sample temperature, sample density (or pressure applied to the sample), sample chemical composition, etc.

2.1.1 Types of Polarization

For uniform isotropic systems and static electric fields, from (2.3)-(2.5) we have

$$\boldsymbol{P} = \varepsilon_0(\varepsilon - 1)\boldsymbol{E} \quad . \tag{2.6}$$

The applied electric field gives rise to a dipole density through the following mechanisms:

Deformation polarization: It can be divided in the two independent types:

Electron polarization - the displacement of nuclei and electrons in the atom under the influence of an external electric field. As electrons are very light they have a rapid response to the field changes; they may even follow the field at optical frequencies.

Atomic polarization - the displacement of atoms or atom groups in the molecule under the influence of an external electric field.

Orientation polarization: The electric field tends to direct the permanent dipoles. The rotation is counteracted by the thermal motion of the molecules. Therefore, the orientation polarization is strongly dependent on the frequency of the applied electric field and on the temperature.

Ionic Polarization: In an ionic lattice, the positive ions are displaced in the direction of an applied field while the negative ions are displaced in the opposite direction, giving a resultant dipole moment to the whole body. The ionic polarization demonstrates only weak temperature dependence and determines mostly by the nature of the interface where the ions can accumulate. Many cooperative processes in heterogeneous systems are connected with ionic polarization.

To investigate the dependence of the polarization on molecular quantities it is convenient to assume the polarization $\boldsymbol{P}$ to be divided into two parts: the induced polarization

$\boldsymbol{P}_{\alpha}$, caused by translation effects, and the dipole polarization $\boldsymbol{P}_{\mu}$, caused by the orientation of the permanent dipoles. Note that in the case of ionic polarization the transport of charge carriers and their trapping can also create induced polarization.

$$\boldsymbol{P}_{\alpha} + \boldsymbol{P}_{\mu} = \varepsilon_0(\varepsilon - 1)\boldsymbol{E} \quad . \tag{2.7}$$

We can now define two major groups of dielectrics: polar and non-polar. A *polar dielectric* is one in which the individual molecules possess a permanent dipole moment even in the absence of any applied field, i.e. the center of positive charge is displaced from the center of negative charge. A *non-polar dielectric* is one where the molecules possess no dipole moment unless they are subjected to an electric field. The mixture of these two types of dielectrics is common in the case of complex liquids and the most interesting dielectric processes occur at their phase borders or liquid-liquid interfaces.

Due to the long range of the dipolar forces an accurate calculation of the interaction of a particular dipole with all other dipoles of a specimen would be very complicated. However, a good approximation can be made by considering that the dipoles beyond a certain distance, say some radius *a*, can be replaced by a continuous medium having the macroscopic dielectric properties. Thus, the dipole, whose interaction with the rest of the specimen is being calculated, may be considered as surrounded by a sphere of radius *a* containing a discrete number of dipoles. To make this approximation the dielectric properties of the whole region within the sphere should be equal to those of a macroscopic specimen, i.e. it should contain a sufficient number of molecules to make fluctuations very small [7,8]. This approach can be successfully used also for the calculation of dielectric properties of ionic self-assembled liquids. In this case the system can be considered as a monodispersed consisting of spherical polar water droplets dispersed in a non-polar medium [9].

Inside the sphere where the interactions take place, the use of statistical mechanics is required. To represent a dielectric with dielectric constant ε, consisting of polarizable molecules with a permanent dipole moment, Fröhlich [6] introduced a continuum with dielectric constant ε_{∞} in which point dipoles with a moment $\boldsymbol{\mu}_d$ are embedded. In this model $\boldsymbol{\mu}_d$ has the same non-electrostatic interactions with the other point dipoles as the molecule had, while the polarizability of the molecules can be imagined to be smeared out to form a continuum with dielectric constant ε_{∞} [7].

In this case, the induced polarization is equal to the polarization of the continuum with the ε_{∞}, so that one can write:

$$\boldsymbol{P}_{\alpha} = \varepsilon_0(\varepsilon_{\infty} - 1)\boldsymbol{E} \,. \tag{2.8}$$

The orientation polarization is given by the dipole density due to the dipoles $\boldsymbol{\mu}_d$. If we consider a sphere with volume V containing dipoles, one can write:

$$\boldsymbol{P}_{\mu} = \frac{1}{V} < \boldsymbol{M}_d > \tag{2.9}$$

where $\boldsymbol{M}_d = \sum_{i=1}^{N} (\boldsymbol{\mu}_d)_i$ is the average component in the direction of the field of the moment due to the dipoles in the sphere.

In order to describe the correlations between the orientations (and also between the positions) of the i-th molecule and its neighbors, Kirkwood [7] introduced a correlation factor g, which was accounted as $g = \sum_{j=1}^{N} < \cos\theta_{ij} >$, where θ_{ij} denotes the angle between the orientation of the i-th and the j-th dipole. An approximate expression for the Kirkwood correlation factor can be derived by taking only nearest-neighbor interactions into account. It reads as follows:

$$g = 1 + z < \cos\theta_{ij} > . \tag{2.10}$$

In this case the sphere is shrunk to contain only the i-th molecule and its z nearest neighbors. Correlation factor g will be different from 1 when $< \cos\theta_{ij} > \neq 0$, i.e. when there is a correlation between the orientations of neighboring molecules. When the molecules tend to direct themselves with parallel dipole moments, $< \cos\theta_{ij} >$ will be positive and $g > 1$. When the molecules prefer to arrange themselves with anti-parallel dipoles, then $g < 1$. Both cases are observed experimentally [6-8]. If there is no specific correlation then $g = 1$. If the correlations are not negligible, detailed information about the molecular interactions is required for the calculations of g.

For experimental estimation of the correlation factor g the Kirkwood-Fröhlich equation [7]

$$g\mu_d^{\,2} = \frac{\varepsilon_0 9 k_B T V}{N} \frac{(\varepsilon - \varepsilon_{\infty})(2\varepsilon + \varepsilon_{\infty})}{\varepsilon(\varepsilon_{\infty} + 2)^2} \tag{2.11}$$

is used, which gives the relation between the dielectric constant ε, the dielectric constant of induced polarization ε_{∞}. Here $k_B = 1.381 \cdot 10^{-23}$ [J·K^{-1}] is the Boltzmann constant, T is absolute

temperature. The correlation factor is extremely useful in understanding the short-range molecular mobility and interactions in self assembled systems [10].

2.2 Dielectric Polarization in Time - Dependent Electric Fields

When an external field is applied to a dielectric, polarization of the material reaches its equilibrium value, not instantaneously, but rather over a period of time. By analogy, when the field is suddenly removed, the polarization decay caused by thermal motion follows the same law as the relaxation or decay function of dielectric polarization $\phi(t)$:

$$\phi(t) = \frac{\boldsymbol{P}(t)}{\boldsymbol{P}(0)}, \tag{2.12}$$

where $\boldsymbol{P}(t)$ is a time dependent polarization vector. The relationship for the dielectric displacement vector $\boldsymbol{D}(t)$ in the case of time dependent fields may be written as follows [6,11]:

$$\mathbf{D}(t) = \varepsilon_0 \left[\varepsilon_\infty \mathbf{E}(t) + \int_{-\infty}^{t} \dot{\Phi}(t') \mathbf{E}(t - t') dt' \right]. \tag{2.13}$$

In (2.13) $\boldsymbol{D}(t) = \varepsilon_0 \boldsymbol{E}(t) + \boldsymbol{P}(t)$, and $\Phi(t)$ is the dielectric response function $\Phi(t) = (\varepsilon_S - \varepsilon_\infty)[1 - \phi(t)]$, where ε_s and ε_∞ are the low and high frequency limits of the dielectric permittivity respectively. The complex dielectric permittivity $\varepsilon^*(\omega)$ (where ω is the angular frequency) is connected with the relaxation function by a very simple relationship [6,11]:

$$\frac{\varepsilon^*(\omega) - \varepsilon_\infty}{\varepsilon_S - \varepsilon_\infty} = \hat{L}\left[-\frac{d}{dt}\phi(t) \right], \tag{2.14}$$

where $\hat{L}$ is the operator of the Laplace transform, which is defined for the arbitrary time-dependent function $f(t)$ as:

$$\hat{L}[f(t)] \equiv F(\omega) = \int_0^\infty e^{-pt} f(t) dt, \qquad p = x + i\omega, \text{ where } x \to 0 \text{ and } i \text{ is an imaginary unit}. \tag{2.15}$$

Relation (2.14) shows that the equivalent information on dielectric relaxation properties of the sample being tested both in frequency and time domain. Therefore the dielectric response might be measured experimentally as a function of frequency or time, providing data in the form of a dielectric spectrum $\varepsilon^*(\omega)$ or the macroscopic relaxation function $\phi(t)$. For example, when macroscopic relaxation function obeys the simple exponential law

$$\phi(t) = \exp(-t/\tau_m), \tag{2.16}$$

where τ_m represents the characteristic relaxation time, the well-known Debye formula for the frequency dependent dielectric permittivity can be obtained by substitution (2.16) into (2.15) [6-8,11]:

$$\frac{\varepsilon^*(\omega)-\varepsilon_\infty}{\varepsilon_S-\varepsilon_\infty} = \frac{1}{1+i\omega\tau_m}. \tag{2.17}$$

For many of the systems being studied, the relationship above does not sufficiently describe the experimental results. The Debye conjecture is simple and elegant. It enables us to understand the nature of dielectric dispersion. However, for most of the systems being studied, the relationship above does not sufficiently describe the experimental results. The experimental data is better described by non-exponential relaxation laws. This necessitates empirical relationships, which formally take into account the distribution of relaxation times.

2.2.1 Dielectric response in Frequency and Time Domains

In the most general sense non-Debye dielectric behavior can be described in terms of a continuous distribution of relaxation times, $G(\tau)$ [11]. This implies that the complex dielectric permittivity can be presented as follows:

$$\frac{\varepsilon^*(\omega)-\varepsilon_\infty}{\varepsilon_S-\varepsilon_\infty} = \int_0^\infty \frac{G(\tau)}{1+i\omega\tau}d\tau, \tag{2.18}$$

where the distribution function $G(\tau)$ satisfies the normalization condition

$$\int_0^\infty G(\tau)d\tau = 1 \qquad (2.19)$$

.

The corresponding expression for the decay function is

$$\phi(t) = \int_0^\infty G(\tau)\exp\left(-\frac{t}{\tau}\right)d\tau \qquad (2.20)$$

.

It must be clearly understood that by virtue of the univalent relationship (2.14) between frequency and time representation the $G(\tau)$ calculation does not provide in itself anything more than another way of describing the dynamic behavior of dielectrics in time domain [12]. Moreover, such a calculation is a mathematically ill-posed problem [13,14], which leads to additional mathematical difficulties.

In most cases of non-Debye dielectric spectrum has been described by the so-called Havriliak-Negami (*HN*) relationship [8,11,15]:

$$\varepsilon^*(\omega) = \varepsilon_\infty + \frac{\varepsilon_S - \varepsilon_\infty}{\left[1+(i\omega\tau_m)^\alpha\right]^\beta}, \qquad 0 \le \alpha, \beta \le 1 . \qquad (2.21)$$

Here α and β are empirical exponents. The specific case α=1, β=1 gives the Debye relaxation law, β=1, $\alpha\neq$1 corresponds to the so-called Cole-Cole (*CC*) equation [16], whereas the case α=*1*, $\beta\neq$*1*, corresponds to the Cole-Davidson (*CD*) formula [17]. The high and low frequency asymptotic of relaxation processes are usually assigned to Jonscher's power-law wings $(i\omega)^{(n-1)}$ and $(i\omega)^m$ (0<*n*, *m*≤1 are Jonscher stretch parameters) [18,19]. Notice that the real part $\varepsilon'(\omega)$ of the complex dielectric permittivity is proportional to the imaginary part $\sigma''(\omega)$ of the complex *ac* conductivity $\sigma^*(\omega)$, $\varepsilon'(\omega) \propto -\sigma''(\omega)/\omega$, and the dielectric losses $\varepsilon''(\omega)$ are proportional to the real part $\sigma'(\omega)$ of the *ac* conductivity, $\varepsilon''(\omega) \propto \sigma'(\omega)/\omega$. The asymptotic power law for $\sigma^*(\omega)$ has been termed "*universal*" due to its appearance in many types of disordered systems [20, 21]. Progress has been made recently in understanding the physical significance of the empirical parameters α, β and exponents of Jonscher wings [22-26].

An alternative approach to *DS* study is to examine the dynamic molecular properties of a substance directly in time domain. In the linear response approximation, the fluctuations of polarization caused by thermal motion are the same as for the macroscopic rearrangements

induced by the electric field [27,28]. Thus, one can equate the relaxation function $\phi(t)$ and the macroscopic dipole correlation function (*DCF*) $\Psi(t)$ as follows:

$$\phi(t) \cong \Psi(t) = \frac{\langle \boldsymbol{M}(0)\boldsymbol{M}(t)\rangle}{\langle \boldsymbol{M}(0)\boldsymbol{M}(0)\rangle}, \tag{2.22}$$

where $\boldsymbol{M}(t)$ is the macroscopic fluctuating dipole moment of the sample volume unit, which is equal to the vector sum of all the molecular dipoles. The rate and laws governing the *DCF* are directly related to the structural and kinetic properties of the sample and characterized the macroscopic properties of the system under study. Thus, the experimental function Φ(t) and hence $\phi(t)$ or $\Psi(t)$ can be used to obtain information on the dynamic properties of the dielectric under investigation.

The dielectric relaxation of many complex systems deviates from the classical exponential Debye pattern (2.16) and can be described by the Kohlrausch-Williams-Watts (*KWW*) law or the "*stretched exponential law*" [29,30]

$$\phi(t) = \exp\left\{-\left(\frac{t}{\tau_m}\right)^{\nu}\right\} \tag{2.23}$$

with a characteristic relaxation time τ_m and empirical exponent $0 < \nu \leq 1$. The *KWW* decay function can be considered as a generalization of Eq.(2.16) that becomes Debye's law when ν=1. Another common experimental observation of *DCF* is the asymptotic power law [18,19]

$$\phi(t) = A\left(\frac{t}{\tau_1}\right)^{-\mu}, \quad t \geq \tau_1 , \tag{2.24}$$

with an amplitude *A*, an exponent $\mu > 0$ and a characteristic time τ_1 which is associated with the effective relaxation time of the microscopic structural unit. This relaxation power law is sometimes referred by the literature as describing anomalous diffusion when the mean square displacement does not obey the linear dependency $\langle R^2\rangle \sim t$. Instead, it is proportional to some power of time $\langle R^2\rangle \sim t^{\gamma}$ ($0<\gamma<2$) [31-33]. In this case, the parameter τ_1 is an effective relaxation time required for the charge carrier displacement on the minimal structural unit size. A number of approaches exists to describe such kinetic processes: Fokker-Planck

equation [34], propagator representation [35,36], different models of dc- and ac-conductivity [20,25], etc.

In frequency domain, Jonscher's power-law wings, when evaluated by *ac* conductivity measurements, sometimes reveal a dual transport mechanism with different characteristic times. In particular, they treat anomalous diffusion as a random walk in fractal geometry [31] or as a thermally activated hopping transport mechanism [37].

An example of a phenomenological decay function that has different short- and long-time asymptotic forms (with different characteristic times) can be presented as follows [38,39]

$$\phi(t) = A\left(\frac{t}{\tau_1}\right)^{-\mu} \exp\left\{-\left(\frac{t}{\tau_m}\right)^{\nu}\right\}. \tag{2.25}$$

This function is the product of *KWW* and power-law dependencies. The relaxation law (2.25) in time domain and the *HN* law (2.21) in frequency domain are rather generalized representations that lead to the known dielectric relaxation laws. The fact that these functions have the power-law asymptotic has inspired numerous attempts to establish a relationship between their various parameters [40,41]. In this regard, the exact relationship between the parameters of (2.25) and the *HN* law (2.21) should be a consequence of the Laplace transform according to (2.14) [11,12]. However, there is currently no concrete proof that this is indeed so. Thus, the relationship between the parameters of equations (2.21) and (2.25) seems to be valid only asymptotically.

In summary, we must say that unfortunately there is as yet no generally acknowledged opinion about the origin of the non-Debye dielectric response. However, there exist a significant number of different models which have been elaborated to describe non-Debye relaxation in some particular cases. In general these models can be separated into three main classes:

a. The models in the first class are based on the idea of relaxation times distribution and regarded non-Debye relaxation as a cumulative effect arising from the combination of a large number of microscopic relaxation events obeying the appropriate distribution function. These models such as the concentration fluctuations model [42], the mesoscopic mean-field theory for supercooled liquids [43], or the recent model for *ac* conduction in disordered media [20], are derived and closely connected to the microscopic background of the relaxation process. However, they cannot answer the question about the origin of very elegant empiric equations of (2.21) or (2.25).

b. The second type of models are based on the idea of Debye's relaxation equation with the derivatives of non-integer order (for example [22,26,44,45]). This approach is immediately able to reproduce all known empirical expressions for non-Debye relaxation. However, they are rather formal models and they are missing the link to the microscopic relaxations.

c. In a certain sense the third class of models provides the bridge between the two previous cases. From one side they are based on the microscopic relaxation properties and, from another side reproduced the known empirical expressions for non-Debye relaxation. The most famous and definitely most elaborate example of such a description is the application of the continuous random walk theory to the anomalous transport problem (see the very detailed review of this problem in [31]).

Later, we will discuss in detail two examples of such models: The model of Relaxation Peak Broadening which describes a relaxation of the Cole-Cole type [46] and the model of Coordination Spheres for relaxations of the *KWW* type [47].

2.3 Relaxation kinetics

It was already mentioned that the properties of a dielectric sample are a function of many experimentally controlled parameters. In this regard, the main issue is the temperature dependency of the characteristic relaxation times, i.e. relaxation kinetics. Historically, the term "kinetics" was introduced in the field of Chemistry for the temperature dependency of chemical reaction rates. The simplest model, which describes the dependency of reaction rate k on temperature T, is the so-called Arrhenius law [48]:

$$k = k_0 \exp\left(-\frac{E_a}{k_B T}\right), \tag{2.26}$$

where E_a is the activation energy and k_0 is the pre- exponential factor corresponding to the fastest reaction rate at the limit $T \to \infty$. In his original paper [48] Arrhenius deduced this kinetic law from transition state theory. The basic idea behind (2.26) addressed the single particle transition process between two states separated by the potential barrier of height E_a.

The next development of the chemical reaction rate theory was provided by Eyring [49-51] who suggested a more advanced model

$$k = \frac{k_B T}{\hbar} \exp\left(\frac{\Delta S}{k_B} - \frac{\Delta H}{k_B T} \right), \tag{2.27}$$

where ΔS is activation entropy, ΔH is activation enthalpy, and $\hbar = 6.626 \cdot 10^{-34}$ [J · s] is Plank's constant. As in the case of (2.26) the Eyring law (2.27) is based on the idea of a transition state. However, in contrast to the Arrhenius model (2.26), the Eyring Eq. (2.27) is based on more accurate evaluations of the equilibrium reaction rate constant, producing the extra factor proportional to temperature.

The models (2.26) and (2.27) used to explain the kinetics of chemical reaction rates, were also found to be very useful for other applications. Taking into account the relationship $\tau \sim 1/k$, these equations can describe the temperature dependency of relaxation time τ for dielectric or mechanical relaxations provided by the transition between the initial and final states separated by an energy barrier.

The relaxation kinetics of the Arrhenius and Eyring types were found for an extremely wide class of systems in different aggregative states [7,52-54]. Nevertheless, in many cases, these laws cannot explain the experimentally observed temperature dependences of relaxation rates in different systems. Thus, to describe the relaxation kinetic, especially for amorphous and glass-forming substances [55-59], many authors have used the Vogel-Fulcher-Tammann (*VFT*) law:

$$\ln\left(\frac{\tau}{\tau_0} \right) = \frac{E_{VFT}}{k_B (T - T_{VFT})}, \tag{2.28}$$

where T_{VFT} is the *VFT* temperature and E_{VFT} is the *VFT* energy. This model was first proposed in 1921 by Vogel [60]. Shortly afterwards it was independently discovered by Fulcher [61] and then utilized by Tammann and Hesse [62] to describe their viscosimetric experiments. It is currently widely held that *VFT* relaxation kinetics has found its explanation in the framework of the Adam and Gibbs model [63]. This model is based on the Kauzmann concept [64,65], which states that the configurational entropy is supposed to disappear for an amorphous substance at temperature T_k. Thus, the coincidence between the experimental data and *VFT* law is usually interpreted as a sign of cooperative behavior in a disordered glass-like state.

An alternative explanation of the *VFT* model (2.28) is based on the free volume concept introduced by Fox and Floury [66-68] to describe the relaxation kinetics of polystyrene. The main idea behind this approach is that the probability of movement of a

polymer molecule segment is related to the free volume availability in a system. Later, Doolittle [69] and Turnbull and Cohen [70] applied the concept of free volume to a wider class of disordered solids. They suggested similar relationship

$$\ln\left(\frac{\tau}{\tau_0}\right) = \frac{v_0}{v_f} \quad , \tag{2.29}$$

where v_0 is the volume of a molecule (a mobile unit) and v_f is the free volume per molecule (per mobile unit). Thus, if the free volume grows linearly with temperature $v_f \sim T - T_k$ the *VFT* law (2.28) is immediately obtained.

Later, the *VFT* kinetic model was generalized by Bendler and Shlesinger [71]. Starting from the assumption that the relaxation of an amorphous solid is caused by some mobile defects, they deduced the relationship between τ and *T* in the form

$$\ln\left(\frac{\tau}{\tau_0}\right) = \frac{B}{(T - T_k)^{3/2}} \quad , \tag{2.30}$$

where *B* is a constant dependent on the defect concentration and the characteristic correlation length of the defects space distribution [71]. Model (2.30) is not as popular as the *VFT* law, however it has been found to be very useful for some substances [72,73].

Another type of kinetics pattern currently under discussion is related to the so-called Mode-Coupling Theory (*MCT*) developed by Götze *et al.* [74]. In the *MCT* the cooperative relaxation process in supercooled liquids and amorphous solids is considered to be a critical phenomenon. The model predicts the dependency of relaxation time versus temperature for such substances in the form

$$\tau \sim (T - T_c)^{-\gamma} \quad , \tag{2.31}$$

where T_c is a critical temperature and γ is the critical *MCT* exponent. Relation (2.31) was introduced for the first time by Bengtzelius *et al.* [75] to discuss the temperature dependency of viscosity for methyl-cyclopean and later was utilized for a number of other systems [76,77].

Beside monotonous relaxation kinetics, which is usually treated within the framework of one of the above models, there is experimental evidence of non-monotonous relaxation kinetics [78]. Some of these experimental examples can be described by the model

$$\ln\left(\frac{\tau}{\tau_0}\right) = \frac{E_a}{k_B T} + C\exp\left(-\frac{E_b}{k_B T}\right), \quad (2.32)$$

which can be applied to the situation when dielectric relaxation occurs within a confined geometry. In this case the parameters of (2.32) are the 'confinement factor', *C*, (a small value of *C* denotes weak confinement) and two characteristic activation energies of relaxation process: E_a, which is the activation energy of the process in the absence of confinement, and E_b, which characterizes the temperature dependency of free volume in a confined geometry [78]. In contrast to the *VFT* equation, which is based on the assumption of linear growth of sample free volume with temperature, the above Eq. (2.32) implies that due to the confinement free volume shrinks out with temperature increase.

3 Basic Principles of Dielectric Spectroscopy and Data Analyses

The *DS* method occupies a special place among the numerous modern methods used for physical and chemical analysis of material, because it enables investigation of relaxation processes in an extremely wide range of characteristic times (10^5 - 10^{-13} s). Although the method does not possess the selectivity of *NMR* or *ESR* it offers important and sometimes unique information about the dynamic and structural properties of substances. *DS* is especially sensitive to intermolecular interactions, therefore cooperative processes may be monitored. It provides a link between the properties of the bulk and individual constituents of a complex material (See Figure 1).

However, despite its long history of development, this method is not widespread for comprehensive use because the wide frequency range (10^{-6} - 10^{12} Hz), overlapped by discrete frequency domain methods, have required a great deal of complex and expensive equipment. Also, for various reasons, not all frequency ranges have been equally available for measurement. Thus, investigations of samples with variable properties over time (for example, non-stable emulsions or biological systems) have been difficult to conduct. In addition, low frequency measurements of conductive systems were strongly limited due to electrode polarization. All these reasons mentioned above led to the fact that reliable information on dielectric characteristics of a substance could only be obtained over limited

frequency ranges. As a result the investigator had only part of the dielectric spectrum at his disposal to determine the relaxation parameters.

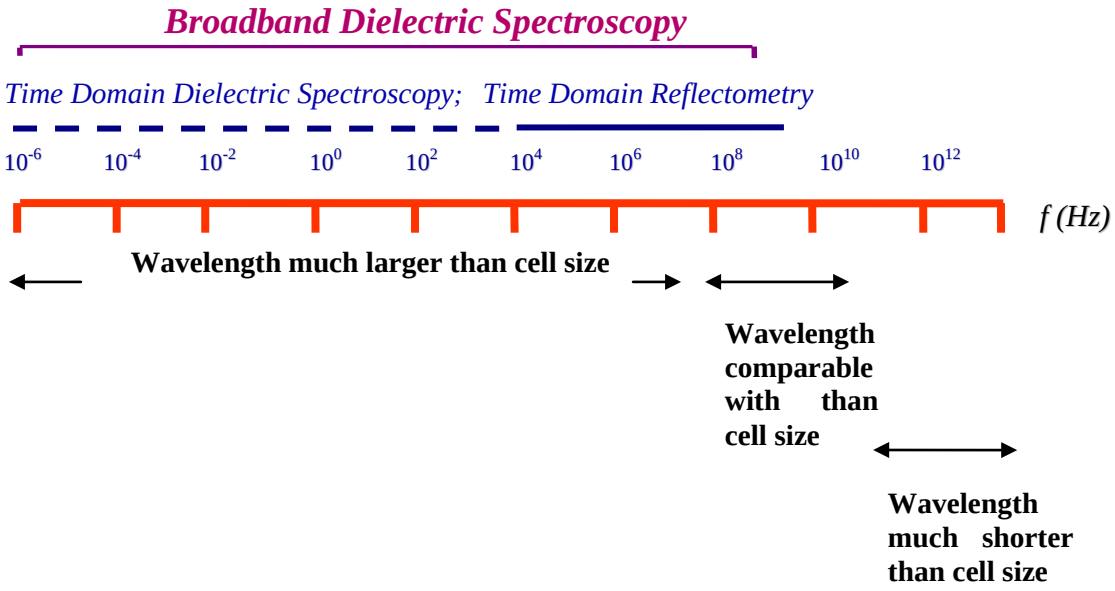

Figure 1. The frequency band of Dielectric spectroscopy.

The successful development of the time domain dielectric spectroscopy method (generally called time domain spectroscopy - *TDS*) [79-86] and Broadband Dielectric Spectroscopy (*BDS*) [3,87-90] have radically changed the attitude towards *DS*, making it an effective tool for investigation of solids and liquids on the macroscopic, mesoscopic and, to some extent, on microscopic levels.

3.1 The Basic Principles of the BDS Methods

As mentioned previously, the complex dielectric permittivity $\varepsilon^*(\omega)$ can be measured by *DS* in the extremely broad frequency range 10^{-6} - 10^{12} Hz (See Figure 1). However, no single technique can characterize materials over all frequencies. Each frequency band and loss regime requires a different method. In addition to the intrinsic properties of dielectrics, their aggregate state, dielectric permittivity and losses, the extrinsic quantities of the measurement tools must be taken into account. In this respect, most dielectric measurement methods and sample cells fall into three broad classes [3,4,91]:

a) Those in which the dielectric properties are measured by means of impedance, *Z*, or admittance, *Y*, where the sample in a measuring cell is treated as a parallel or serial circuit of an ideal (plate or cylindrical) capacitor and an active resistor. All these methods may be called Lumped-Impedance Methods and are largely used at low frequencies (*LF*) (10^{-6}-10^{7}Hz) and in the radio frequency (*RF*) range of the spectrum up to 1 GHz. The *EM* wavelength in these methods is much larger than the sample cell size (See Figure 1). To cover the frequency range $10^{-6} – 10^{7}$ Hz, dielectric analyzers that consist of a Fourier correlation analysis in combination with dielectric converters or impedance analyzers ($10 – 10^{7}$ Hz) are used [3,4,90]. At higher frequencies ($10^{6} – 10^{9}$ Hz) *RF*-reflectometry or spectrum analyzers are applied [3,92].
b) Those in which the dielectric is interacted with travelling and standing electromagnetic waves and can be called "Wave Methods" (10^{9}-10^{11} Hz) [3,4,8]. In this frequency range both network analyzers as well as waveguide and cavity techniques can be applied. The wavelength in these methods is comparable to the sample cell size (See Figure 1).
c) Those (10^{10}-10^{12} Hz) in which the wavelengths are much shorter than the sample cell size (See Figure 1). In these cases quasioptical set-ups like interferometers or oversized cavity resonators are applied [3,4,93]. At sufficiently high frequencies quasioptical methods essentially become optical methods.

The *LF* measurements (a) are provided by means of impedance/admittance analyzers or automatic bridges. Another possibility is to use a frequency response analyzer. In lumped-impedance measurements for a capacitor, filled with a sample, the complex dielectric permittivity is defined as [3]

$$\varepsilon^*(\omega) = \varepsilon'(\omega) - i\varepsilon''(\omega) = \frac{C^*(\omega)}{C_0}, \tag{3.1}$$

where $C^*(\omega)$ is the complex capacitance and C_0 is the vacuum capacitance respectively. Applying a sinusoidal electric voltage $U^*(\omega) = U_0 \exp(i\omega t)$ to the capacitor, the complex dielectric permittivity can be derived by measuring the complex impedance $Z^*(\omega)$ of the sample as follows

$$\varepsilon^*(\omega) = \frac{1}{i\omega\varepsilon_0 Z^*(\omega) C_0}, \tag{3.2}$$

where $Z^*(\omega) = U^*(\omega) / I^*(\omega)$, and $I^*(\omega)$ is the complex current through the capacitor. However, the measuring cells require correction for the residual inductance and capacitance

arising from the cell itself and the connecting leads [4,94]. If a fringing field at the edges of parallel plate electrodes causes a serious error, the three-terminal method is effective for its elimination [95].

In general, the "Wave Methods" (b) may be classified in two ways [4,8,91,96]:

a) They may be travelling-wave or standing wave methods.
b) They may employ a guided-wave or a free–field propagation medium. Coaxial line, metal and dielectric waveguide, microstrip line, slot line, co-planar waveguide and optical-fiber transmission lines are examples of guided-wave media while propagation between antennas in air uses a free-field medium.

In guided-wave propagating methods the properties of the sample cell are measured in terms of Scattering parameters or "*S*-parameters" [4,97], which are the reflection and transmission coefficients of the cell, defined in relation to a specified characteristic impedance, Z_0. In general, Z_0 is the characteristic impedance of the transmission line connected to the cell (50 Ω for most coaxial transmission lines). Note that *S*-parameters are complex number matrices in the frequency domain, which describe the phase as well as the amplitude of travelling waves. The reflection *S*-parameters are usually given by the symbols $S^*_{11}(\omega)$ for the multiple reflection coefficients and S^*_{12} for the forward multiple transmission coefficients. In the case of single reflection $S^*_{11}(\omega)=\rho^*(\omega)$ the simplest formula gives the relationship between the reflection coefficient $\rho^*(\omega)$ and impedance of the sample cell terminated by a transmission line with characteristic impedance Z_0:

$$\rho^*(\omega) = \frac{Z^*(\omega) - Z_0}{Z^*(\omega) + Z_0} \tag{3.3}$$

In all wave methods the transmission line is ideally matched except the sample holder. If the value of $Z^*(\omega)$ is differ from Z_0, one can observe the reflection from a mismatch of the finite magnitude. A similar type of wave analysis also applies in free space and in any other wave systems, taking into account that in free space $Z_0 \approx 377$ Ω for plane waves.

Several comprehensive reviews on the *BDS* measurement technique and its application were published [3,4,95,98] and the details of experimental tools, sample holders for solids, powders, thin films and liquids were described there. Note that in the frequency range 10^{-6}-$3\cdot10^{10}$ Hz the complex dielectric permittivity $\varepsilon^*(\omega)$ can be also evaluated from the time domain measurements of dielectric relaxation function $\phi(t)$ which is related to $\varepsilon^*(\omega)$ by (2.14). In the frequency range 10^{-6}-10^5 Hz the experimental approach is simple and less time-

consuming than measurement in the frequency domain [3,99-102]. However, the evaluation of complex dielectric permittivity in frequency domain requires the Fourier transform. The details of this technique and different approaches including electrical modulus $M^*(\omega) = 1/\varepsilon^*(\omega)$ measurements in the low frequency range were presented recently in a very detailed review [3]. Here we will concentrate more on the time domain measurements in the high frequency range 10^5-$3 \cdot 10^{10}$ Hz, usually called Time Domain Reflectometry (*TDR*) methods. These will still be called *TDS* methods.

3.2 The Basic Principles of the *TDS* Methods

TDS is based on transmission line theory in the time domain that aids in the study of heterogeneities in coaxial lines according to the change of the shape of a test signal [79-86]. As long as the line is homogeneous the shape of this pulse will not change. However, in the case of a heterogeneity in the line (the inserted dielectric, for example) the signal is partly reflected from the interface and partly passes through it. Dielectric measurements are made along a coaxial transmission line with the sample mounted in a sample cell that terminates the line. The simplified block diagram of the setup common for most TDS methods (except transmission techniques) is presented in Figure 2. Main differences include the construction of the measuring cell and its position in the coaxial line. These lead to different kinds of expressions for the values that are registered during the measurement and the dielectric characteristics of the objects under study. A rapidly increasing voltage step $V_0(t)$ is applied to the line and recorded, along with the reflected voltage $R(t)$ returned from the sample and delayed by the cable propagation time (Figure 3). Any cable or instrument artefacts are separated from the sample response due to the propagation delay, thus making them easy to identify and control. The entire frequency spectrum is captured at once, thus eliminating drift and distortion between frequencies.

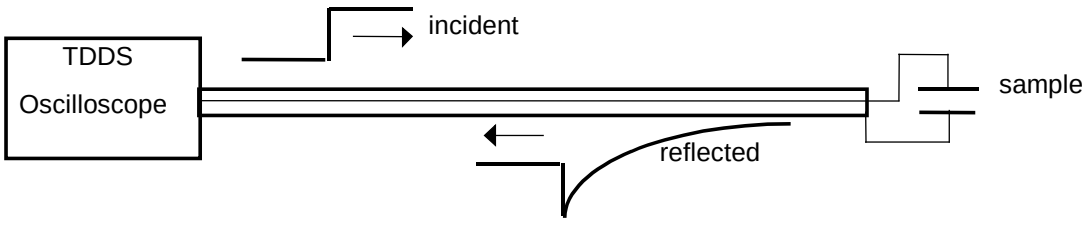

Figure 2. Illustration of the basic principles of the TDS system. (Reproduced with permission from Ref. 113. Copyright 2000, Marcel Dekker, Inc.)

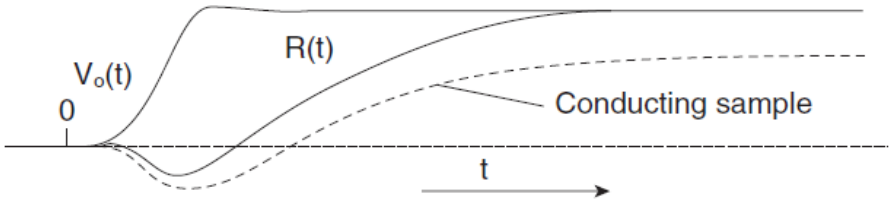

Figure 3. Characteristic shape of the signals recorded during a TDS experiment, $V_0(t)$, incident pulse; $R(t)$, reflected signal. (Reproduced with permission from Ref. 86. Copyright 1996, American Institute of Physics.)

The complex permittivity is obtained as follows: For non-disperse materials (frequency-independent permittivity), the reflected signal follows the exponential response of the *RC* line-cell arrangement; for disperse materials, the signal follows a convolution of the line-cell response with the frequency response of the sample. The actual sample response is found by writing the total voltage across the sample as follows

$$V(t) = V_0(t) + R(t) \quad , \tag{3.4}$$

and the total current through the sample [80,86,103]

$$I(t) = \frac{1}{Z_0}[V_0(t) - R(t)] \quad , \tag{3.5}$$

where the sign change indicates direction and Z_0 is the characteristic line impedance. The total current through a conducting dielectric is composed of the displacement current $I_D(t)$, and the low-frequency current between the capacitor electrodes $I_R(t)$. Since the active resistance at zero frequency of the sample-containing cell is [86] (Figure 3):

$$r = \lim_{t\to\infty}\frac{V(t)}{I(t)} = Z_0 \lim_{t\to\infty}\frac{V_0(t)+R(t)}{V_0(t)-R(t)} \quad , \tag{3.6}$$

the low-frequency current can be expressed as:

$$I_R(t) = \frac{V(t)}{r} = \frac{V_0(t)+R(t)}{Z_0}\lim_{t\to\infty}\frac{V_0(t)-R(t)}{V_0(t)+R(t)} \tag{3.7}$$

Thus relation (3.5) can be written as:

$$I_D(t) = \frac{1}{Z_0}\left\{[V_0(t) - R(t)] - [V_0(t) + R(t)]\lim_{t\to\infty}\frac{V_0(t) - R(t)}{V_0(t) + R(t)}\right\} \tag{3.8}$$

Relations (3.4) and (3.8) present the basic equations that relate *I(t)* and *V(t)* to the signals recorded during the experiment. In addition, (3.8) shows that *TDS* permits one to determine the low-frequency conductivity σ of the sample directly in time domain [84-86]:

$$\sigma = \frac{\varepsilon_0}{Z_0 C_0}\lim_{t\to\infty}\frac{V_0(t) - R(t)}{V_0(t) + R(t)} \tag{3.9}$$

Using *I(t),V(t)* or their complex Fourier transforms *i(ω)* and *v(ω)* one can deduce the relations that will describe the dielectric characteristics of a sample being tested either in frequency or time domain. The final form of these relations depends on the geometric configuration of the sample cell and its equivalent representation [79-86].

The admittance of the sample cell terminated to the coaxial line is then given by

$$\mathrm{Y}(\omega) = \frac{i(\omega)}{v(\omega)}\ , \tag{3.10}$$

and the sample permittivity can be presented as follows:

$$\varepsilon(\omega) = \frac{\mathrm{Y}(\omega)}{i\omega C_0}\ . \tag{3.11}$$

To minimize line artefacts and establish a common time reference, (3.10) is usually rewritten in differential form, to compare reflected signals from the sample and a calibrated reference standard and thus eliminate $V_0(t)$ [79-86].

If one takes into account the definite physical length of the sample and multiple reflections from the air-dielectric or dielectric-air interfaces, relation (3.11) must be written in the following form [79-84,103]:

$$\varepsilon^*(\omega) = \frac{c}{i\omega(\gamma d)}Y(\omega)X\cot X\ , \tag{3.12}$$

where $X = (\omega d / c)\sqrt{\varepsilon^*(\omega)}$, d is the length of the inner conductor, c is the velocity of light, and γ is the ratio between the capacitance per unit length of the cell to that of the matched coaxial cable. Equation (3.12) in contrast to (3.11) is a transcendental one, and its exact solution can be obtained only numerically [79-84]. The key advantage of TDS methods in

comparison with frequency methods is the ability to obtain the relaxation characteristics of a sample directly in time domain. Solving the integral equation one can evaluate the results in terms of the dielectric response function *Φ(t)* [86,103,104]. It is then possible to associate $\varphi(t) = \Phi(t) + \varepsilon_\infty$ with the macroscopic dipole correlation function *Ψ(t)* [2,105,106] in the framework of linear response theory.

3.2.1 Experimental Tools

3.2.1.1 Hardware

The standard time-domain reflectometers used to measure the inhomogeneities of coaxial lines [80, 86,107,108] are the basis of the majority of modern *TDS*-setups. The reflectometer consists of a high-speed voltage step generator and a wide-band registering system with a single or double-channel sampling head. In order to meet the high requirements of *TDS* measurements such commercial equipment must be considerably improved. The main problem is due to the fact that the registration of incident *V(t)* and reflected *R(t)* signals is accomplished by several measurements. In order to enhance the signal - noise ratio one must accumulate all the registered signals. The high level of drift and instabilities during generation of the signal and its detection in the sampler are usually inherent to the serial reflectometry equipment.

The new generation of digital sampling oscilloscopes [109-111] and specially designed time domain measuring set-ups [86] offer comprehensive, high precision, and automatic measuring systems for *TDS* hardware support. They usually have a small jitter-factor (< 1.5 ps), important for rise time; small flatness of incident pulse (<0.5 % for all amplitudes) and in some systems a unique option for parallel time non-uniform sampling of the signal [86].

The typical *TDS* set-up consists of a signal recorder, a 2-channel sampler and a built-in pulse generator. The generator produces 200 mV pulses of 10 μs duration and short rise time (~30 ps). Two sampler channels are characterized by an 18 GHz bandwidth and 1.5 mV noise (*RMS*). Both channels are triggered by one common sampling generator that provides their time correspondence during operation. The form of the voltage pulse thus measured is digitized and averaged by the digitizing block of Time Domain Measurement System (*TDMS*). The time base is responsible for the major metrology *TDMS* parameters. The block diagram of the described *TDS* set-up is presented in Figure (4) [86].

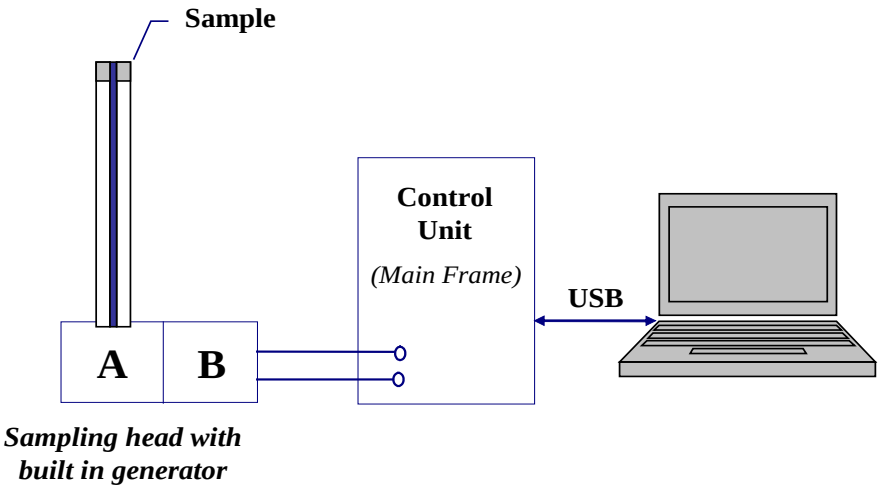

Figure 4. Circuit diagram of a TDS setup. Here A and B are two sampler channels.

3.2.1.2 Non-uniform Sampling

In highly disordered complex materials, the reflected signal *R(t)* extends over wide ranges of time and cannot be captured on a single time scale with adequate resolution and sampling time. In an important modification of regular *TDR* systems, a non-uniform sampling technique (parallel or series), has been developed [86,112].

In the series realization consecutive segments of the reflected signal on an increasing time scale are registered and linked into a combined time scale. The combined response is then transformed using a running Laplace transform to produce the broad frequency spectra [112].

In the parallel realization a multi-window sampling time scale is created [86]. The implemented time scale is the piecewise approximation of the logarithmic scale. It includes $nw \subseteq 16$ sites with a uniform discretization step determined by the following formula:

$$\delta_{nw} = \delta_1 \times 2^{nw}, \tag{3.13}$$

where δ_1=5 ps is the discretization step at the first site, and the number of points in each step except for the first one is equal to npw=32. At the first site, the number of points npw_1=2**npw*. The doubling of the number of points at the first site is necessary in order to have the formal zero time position, which is impossible in the case of the strictly logarithmic structure of the scale. In addition, a certain number of points located in front of the zero time position are added. They serve exclusively for the visual estimation of the stability of the time position of a signal and are not used for the data processing.

The described structure of the time scale allows the overlapping of the time range from 5 ps to 10 μs during one measurement, which results in a limited number of registered readings. The overlapped range can be shortened, resulting in a decreasing number of registered points and thus reducing the time required for data recording and processing.

The major advantage of the multi-window time scale is the ability to get more comprehensive information. The signals received by using such a scale contain information within a very wide time range and the user merely decides which portion of this information to use for further data processing. Also, this scale provides for the filtration of registered signals close to the optimal one already at the stage of recording.

3.2.1.3 Sample Holders

Unfortunately, a universal sample holder that can be used for both liquid and solid samples in both the low and high frequency regions of the *TDS* as well as *BDS* methods is not yet available. The choice of a sample holder configuration depends on the method, value of dielectric permittivity, dc-conductivity and dielectric losses, state of the substance (liquid, solid, powder, film, etc) and data treatment procedure. In the framework of the lumped capacitor approximation one can consider three main types of sample holders [86,103,113] (See Figure 5):

(a) A cylindrical capacitor filled with sample. This cell (a cut-off cell) can also be regarded as a coaxial line segment with the sample having an effective γd length characterized in this case by the corresponding propagation parameters. This makes it possible to use practically identical cells for various *TDS* and *BDS* method modification [114]. For the total reflection method the cut-off cell is the most frequent configuration [79-85]. The recent theoretical analysis of the cut-off sample cell (Figure 5a) showed that a lumped-element representation enables the sample cell properties to be accurately determined over a wide frequency range [114].

(b) Another type of sample holder that is frequently used is a plate capacitor terminated to the central electrode on the end of the coaxial line (Figure 5b) [86, 103, 114-116].

(c) The current most popular sample holder for different applications is an open-ended coaxial line sensor (Figure 5c) [117-125].

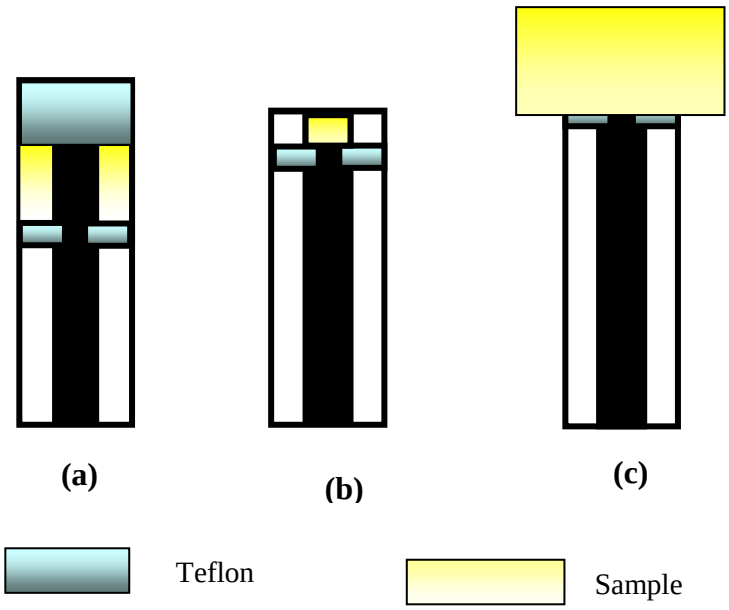

Figure 5. Simplified drawings of sample cells. (a) Open coaxial line cell; (b) lumped capacitance cell; (c) open-ended coaxial cell. (Reproduced with permission from Ref. 113. Copyright 2000, Marcel Dekker, Inc.)

In the case of lumped capacitance approximation the configurations in (See Figures 5a-b) have high frequency limitations and for highly polar systems one must take into account the finite propagation velocity of the incident pulse [82-86,113]. The choice of sample cell shape is determined to a high extent by the aggregate condition of the system under study. While cell (a) is convenient to measure liquids, configuration (b) is more suitable for the study of solid disks, crystals [115,126] and films. Both cell types can be used to measure powder samples. While studying anisotropic systems (liquid crystals, for instance) the user may replace a coaxial line by a strip line or construct the cell with the configuration providing measurements under various directions of the applied electric field [84,85]. The (c) type cell is used only when it is impossible to put the sample into the (a) or (b) cell types [86,121-125,127-129]. The fringing capacity of the coaxial line end is the working capacity for such a cell. This kind of cell is widely used now for investigating the dielectric properties of biological materials and tissues [122-125], petroleum products [119], constructive materials [110], soil [129] and numerous other non-destructive permittivity and permeability measurements. Theory and calibration procedures for such open-coaxial probes are well developed [129-131] and the results meet the high standards of other modern measuring systems.

3.2.2 Data Processing

Measurement procedures, registration, storage, time referencing and data analyses are carried out automatically in the modern *TDS* systems. The process of operation is performed in an on-line mode and the results can be presented in both frequency and time domain [86]. There are several features of the modern software that control the process of measurement and calibration. One can define the time windows of interest that may be overlapped by one measurement. During the calibration procedure the precise determination of the front edge position is carried out and the setting of an internal auto centre on these positions applies to all subsequent measurements. The precise determination and settings of horizontal and vertical positions of calibration signals are also carried out. All parameters may be saved in a configuration file, allowing for a complete set of measurements using the same parameters without additional calibration.

The data processing software includes the options of signal correction, correction of electrode polarization and dc-conductivity, and different fitting procedures both in time and frequency domain [86].

3.3 Data analysis and fitting problems

The principle difference between the *BDS* and *TDS* methods is that *BDS* measurements are fulfilled directly in frequency domain while the *TDS* operates in time domain. In order to avoid unnecessary data transformation it is preferable to perform data analysis directly in the domain, where the results were measured. However, nowadays there are no principle difficulties to transform data from one domain to another by direct or inverse Fourier transform. Below we will concentrate on the details of data analysis only in the frequency domain.

3.3.1 The continuous parameter estimation problem

Dielectric relaxation of complex materials over wide frequency and temperature ranges in general may be described in terms of several non-Debye relaxation processes. A quantitative analysis of the dielectric spectra begins with the construction of a fitting function in selected frequency and temperature intervals, which corresponds to the relaxation processes in the spectra. This fitting function is a linear superposition of the model functions (such as *HN*, Jonscher, dc-conductivity terms, See Paragraph 2.2.1) that describes the frequency

dependence of the isothermal data of the complex dielectric permittivity. The temperature behavior of the fitting parameters reflects the structural and dynamic properties of the material.

However, there are several problems in selecting the proper fitting function, such as the limited frequency and temperature ranges of the experiment, distortion influences of the sample holder and the overlapping of several physical processes with different amplitudes in the same frequency and temperature ranges. The latter is the most crucial problem, because some of the relaxation processes are "screened" by the others. For such a "screened" process, the confidence in parameter estimations can be very small. In this case, the temperature functional behavior of the parameters may be inconsistent. Despite these discontinuities, there may still be some trends in the parameter behavior of the "screened" processes which may reflect some tendencies of the physical processes in the system. Therefore, it is desirable to obtain a continuous solution of the model parameters via temperature. This solution is hardly achievable if the estimation of the parameters is performed independently for the different temperature points on the selected fitted range. Post-fitted parameter smoothing can spoil the quality of the fit. A new procedure for smooth parameter estimation, named the "global fit", was proposed recently [132]. It obtains a continuous solution for the parameter estimation problem. In this approach, the fitting is performed simultaneously for all the temperature points. The smoothness of the solution is obtained by the addition of some penalty term to the cost function in the parameter minimization problem. Coupled with a constraint condition for the total discrepancy measure between the data and the fit function [132], the desired result is achieved.

The penalized functional approach for obtaining a continuous solution of the minimization problem is a well-known regularization technique in image restoration problems such as image de-noising or image de-blurring [133].

In the field of dielectric spectroscopy such regularization procedures have been used by Schäfer *et al*. [14] for extracting the logarithmic distribution function of relaxation times, $G(\tau)$. In contrast to the parametric description of the broadband dielectric spectra considered in our work, the approach of Schäfer *et al* is essentially non-parametric. These authors used a regularization technique for the construction of the response function through the Fredholm integral equation solution. The approach proposed in [132] deals with the problem of finding fitting parameters that describe dielectric data in the frequency domain in a wide frequency band, to obtain a continuous estimation of the fitting parameters via temperature, or any other external parameters.

3.3.2 dc-Conductivity problems

The dielectric spectroscopy study of conductive samples is very complicated because of the need to take into account the effect of dc-conductivity. The dc-conductivity σ_0 contributes, in frequency domain, to the imaginary part of the complex dielectric permittivity as an additional function $\sigma_0/(\varepsilon_0\omega)$. The presence of dc-conductivity makes it difficult to analyze relaxation processes especially when the contribution of the conductivity is much greater than the amplitude of the process. The correct calculation of the dc-conductivity is important in terms of the subsequent analysis of the dielectric data. Its evaluation by fitting of the experimental data does not always give correct results, especially when relaxation processes are present in the low frequency range. In particular, the dc-conductivity function has frequency power-law dependence similar to the Jonscher terms in the imaginary part of the complex dielectric permittivity and this makes computation of dc-conductivity even more difficult.

It is known that in some cases the modulus representation $M^*(\omega)$ of dielectric data is more efficient for dc-conductivity analysis, since it changes the power law behavior of the dc-conductivity into a clearly defined peak [134]. However, there is no significant advantage of the modulus representation when the relaxation process peak overlaps the conductivity peak. Moreover, the shape and position of the relaxation peak will then depend on the conductivity. In such a situation, the real component of the modulus, containing the dc-conductivity as an integral part, does not help to distinguish between different relaxation processes.

Luckily, the real and imaginary parts of the complex dielectric permittivity are not independent of each other and are connected by means of the Kramers–Kronig relations [11]. This is one of the most commonly encountered cases of dispersion relations in linear physical systems. The mathematical technique used by the Kramers–Kronig relations is the Hilbert transform. Since dc-conductivity enters only the imaginary component of the complex dielectric permittivity the static conductivity can be calculated directly from the data by means of the Hilbert transform.

3.3.3 Continuous Parameter Estimation Routine

The complex dielectric permittivity data of a sample, obtained from *DS* measurements in a frequency and temperature interval can be organized into the matrix data massive $\boldsymbol{\varepsilon} \equiv \left[\varepsilon_{i,j} \right]$ of size $M \times N$, where $\varepsilon_{i,j} \equiv \varepsilon(\omega_i, T_j)$, M is the number of measured frequency points and N is the number of measured temperature points. Let us denote by $f = f(\omega; \mathbf{x})$ the fitting function of *n* parameters $\mathbf{x} = \{x_1, x_2, ..., x_n\}$. This function is assumed to be a linear superposition of the model descriptions (such as the Havriliak-Negami function or the Jonscher function, considered in section 2.2.1). The dependence of *f* on temperature *T* can be considered to be via parameters only: $f = f(\omega; \mathbf{x}(T))$. Let us denote by $X \equiv \left[x_i(T_j) \right]$ the $n \times N$ matrix of *n* model parameters x_i, computed at *N* different temperature points T_j.

The classical approach to the fit parameter estimation problem in dielectric spectroscopy is generally formulated in terms of a minimization problem: finding values of *X* which minimize some discrepancy measure $S(\boldsymbol{\varepsilon}, \hat{\boldsymbol{\varepsilon}})$ between the measured values, collected in the matrix $\boldsymbol{\varepsilon}$ and the fitted values $\hat{\boldsymbol{\varepsilon}} = [f(\omega_i, \mathbf{x}(T_j))]$ of the complex dielectric permittivity. The choice of $S(\boldsymbol{\varepsilon}, \hat{\boldsymbol{\varepsilon}})$ depends on noise statistics [132].

3.3.4 Computation of the dc-conductivity using Hilbert transform

The coupling between real and imaginary components of the complex dielectric permittivity $\varepsilon^*(\omega)$ is provided by the Kramers-Kronig relations, one of the most general cases of dispersion relations in physical systems. The mathematical technique used by the Kramers-Kronig relations, which allows one component to be defined through another, is the Hilbert transform since $\varepsilon'(\omega)$ and $\varepsilon''(\omega)$ are Hilbert transform pairs. Performing a Hilbert transform of $\varepsilon'(\omega)$ and subtracting the result from $\varepsilon''(\omega)$, the dc-conductivity, $\sigma_0 / (\varepsilon_0 \omega)$, can be computed directly from the complex dielectric permittivity data. The simulated and experimental examples show very good accuracy for calculating dc-conductivity by this method.

The Kramers-Kronig dispersion relations between imaginary and real parts of dielectric permittivity can be written as follows [11]:

$$\varepsilon'(\omega) = \varepsilon_\infty + \frac{1}{\pi}\hat{P}\int_{-\infty}^{\infty}\frac{\hat{\varepsilon}''(\omega')}{\omega' - \omega}d\omega' \tag{3.14}$$

,

$$\hat{\varepsilon}''(\omega) = \varepsilon''(\omega) - \frac{\sigma_0}{\varepsilon_0\omega} = \frac{1}{\pi}\hat{P}\int_{-\infty}^{\infty}\frac{\varepsilon'(\omega')}{\omega' - \omega}d\omega' \tag{3.15}$$

,

where the symbol $\hat{P}$ denotes the Cauchy principal value of the integral. The Hilbert transform $H[g]$ of a real function $g(t)$ is defined as:

$$H[g] = -\frac{1}{\pi}P\int_{-\infty}^{\infty}\frac{g(\xi)}{\xi - \omega}d\xi \tag{3.16}$$

Therefore the conductivity term in the second dispersion relation (3.15) can be presented as follows:

$$\frac{\sigma_0}{\varepsilon_0\omega} = \varepsilon''(\omega) - \hat{\varepsilon}''(\omega) \tag{3.17}$$

.

The result shows that dc-conductivity can be computed by using the Hilbert transform applied to the real components of the dielectric permittivity function and subtracting the result from its imaginary components. The main obstacle to the practical application of the Hilbert transform is that the integration in equation (3.16) is performed over infinite limits; however, a DS spectroscopy measurement provides values of $\varepsilon^*(\omega)$ only over some finite frequency range. Truncation of the integration in the computation of the Hilbert Transform can yield a serious computational error in calculating $H[\varepsilon'(\omega)]$ in the measured frequency range. This problem cannot be overcome unless the "missing" dielectric data is supplied. However, the computational error can be reduced by extending $\varepsilon'(\omega)$ into a frequency domain outside the measuring frequency range. Although this is a rather crude data treatment, computer simulations show that computational error due to the truncation of the measuring frequency range is greater near the borders of the range. Far from the borders of the frequency range the relative error is much smaller and is of the order of 10^{-4}.

While our method works well with most situations, it is limited when $\varepsilon'(\omega)$ exhibits a low frequency tail. Such a situation is characteristic of percolation, electrode polarization or other low-frequency process, where the reciprocal of the characteristic relaxation time for the process is just below our frequency window. In this case aliasing effects distort the transform result.

Practically, the Numerical Hilbert Transform can be computed by means of the well-known Fast Fourier Transform (*FFT*) routine. It is based on the following property of the Hilbert Transform [135]. If

$$g(t) = \frac{1}{\pi}\int_0^{\infty}\left[a(\omega)\cos\omega t + b(\omega)\sin\omega t\right]d\omega \tag{3.18}$$

is the Fourier transform of a real function $g(t)$, then the Fourier-transform of the function $H[g]$ is the following:

$$H[g] = \frac{1}{\pi}\int_0^{\infty}\left[b(\omega)\cos\omega t - a(\omega)\sin\omega t\right]d\omega \tag{3.19}$$

.

Thus, by performing the Fourier transform of the data with an *FFT* algorithm, the Hilbert transform is computed by inverse-*FFT* operation to the phase-shifting version of the Fourier transform of the original data. Such an approach was realized in the work of Castro and Nabet [136], where the real component of the dielectric permittivity was calculated from its imaginary component, using the Hilbert transform. For the Hilbert transform computation, the authors used a procedure included in the MATLAB package. This methodology was also based on the *FFT* technique, requiring uniform sampling over the frequency interval. If the data are not measured uniformly, it should be interpolated to frequency points, evenly spaced with an incremental frequency equal to or less than the start frequency. However, this routine cannot be used for a wide spectral range. For example, in order to cover an interval of 12 decades with an incremental frequency equal to the start frequency 10^{12} points are required. This, of course, is not practical. To overcome this limitation, a procedure based on a moving frequency window has been developed, where the scale inside the window is linear, but the window jump is logarithmic. This kind of methodology employing moving windows with *FFT* has been used in the past [137].

3.3.5 Computing software for data analysis and modeling

Software for dielectric data treatment and modeling in frequency domain has been developed recently [132]. This program (MATFIT) was built around the software package MATLAB (Math Works Inc.) and its functionality is available through an intuitive visual interface. Key features of the program include:

• Advanced data visualization and pre-processing tools for displaying complex dielectric permittivity data and selecting appropriate frequency and temperature intervals for modeling;
• A library of standard relaxation fit functions;
• Simultaneous fit of both real and imaginary components of the complex dielectric permittivity data;
• Linear and nonlinear fitting methods, from least-squares and logarithmic to fitting procedures based on the entropy norm;
• Global fit procedure on all selected temperature ranges for continuous parameter estimation;
• Hilbert transform for computing dc-conductivity;
• Parameter visualization tool for displaying fitting parameter functions via temperature and subsequent analysis of the graphs.

The methodology described above, utilized in the presented program [132], and reduces the problem of dielectric data analysis to choosing the appropriate model functions and an estimation of their model parameters. The penalized maximum likelihood approach for obtaining these parameters as a function of temperature has proven to be a consistent method for accurately obtaining the global minimum in this estimation. This methodology is a phenomenological approach to obtaining the underlying temperature dependence of the parameter space, while not presupposing a particular physical model. The risk is present that such a regularization routine may perturb the result if used excessively. For this reason a regularization parameter is used to control the smoothing term. However, this risk is far less than the risk of *a priori* conclusion of the result according to the researcher's personal belief in a preferred analytical model.

4 Dielectric response in some disordered materials

In this contribution we are presenting some concepts of modern dielectric spectroscopy. We are going to illustrate these ideas by experimental examples related to different complex systems. In many cases we will refer different features of dielectric response observed in the same samples. Parallel with the description of morphology for each system, the phenomenological identification of the relaxation processes and their relation to dynamic of structural units is established. In spite of the structural and dynamic differences, the general features of the relaxation processes will be indicated.

4.1 Microemulsions

Microemulsions are thermodynamically stable, clear fluids, composed of oil, water, surfactant and sometimes co-surfactant that have been widely investigated during recent years because of their numerous practical applications. The chemical structure of surfactants may be low-molecular weight as well as polymeric, with nonionic or ionic components [138-141]. In the case of a water/oil-continuous (W/O) microemulsion, at low concentration of the dispersed phase, the structure is that of spherical water droplets surrounded by a monomolecular layer of surfactant molecules whose hydrophobic tails are oriented towards the continuous oil phase (See Figure 6). When the volume fractions of oil and water are high and comparable, random bicontinuous structures are expected to form.

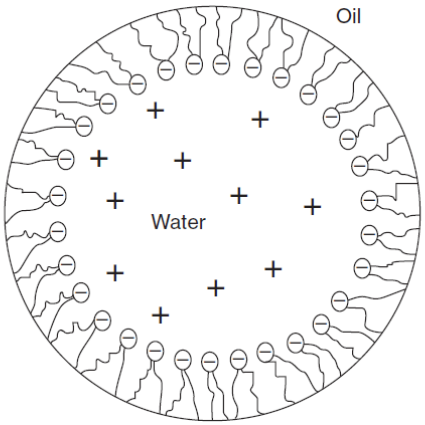

Figure 6. Schematic presentation of spherical water droplet surrounded by a monomolecular layer of ionic surfactant molecules.

The structure of the microemulsion depends on the interaction between droplets. In the case of repulsive interaction, the collisions of the droplets are short and no overlapping occurs between their interfaces. However, if the interactions are attractive, transient random droplet clusters are formed. The number and sizes of such clusters are increasing with the temperature, the pressure, or the water to surfactant ratio, leading to a percolation in the system [113,142-145].

The majority of the different chemical and physical properties, as well as the morphology of microemulsions, is determined mostly by the micro-Brownian motions of its components. Such motions cover a very wide spectrum of relaxation times ranging from tens of seconds to a few picoseconds. Given the complexity of the chemical makeup of microemulsions, there are many various kinetic units in the system. Depending on their nature, the dynamic processes in the microemulsions can be classified into three types:

The first type of relaxation processes reflects characteristics inherent to the dynamics of single droplet components. The collective motions of the surfactant molecule head groups at the interface with the water phase can also contribute to relaxations of this type. This type can also be related to various components of the system containing active dipole groups, such as cosurfactant, bound and free water. The bound water is located near the interface, while "free" water, located more than a few molecule diameters away from the interface, hardly influenced by the polar or ion groups. In the case of ionic microemulsions, the relaxation contributions of this type are expected to be related to the various processes associated with the movement of ions and/or surfactant counterions relative to the droplets and their organized clusters and interfaces [113,146];

For percolating microemulsions, *the second* and the *third types* of relaxation processes characterize the collective dynamics in the system and are of a *cooperative nature*. The dynamics of the *second type* may be associated with the transfer of an excitation caused by the transport of electrical charges within the clusters in the percolation region. The relaxation processes of the *third type* are caused by rearrangements of the clusters and are associated with various types of droplet and cluster motions, such as: translations, rotations, collisions, fusion and fission [113,143].

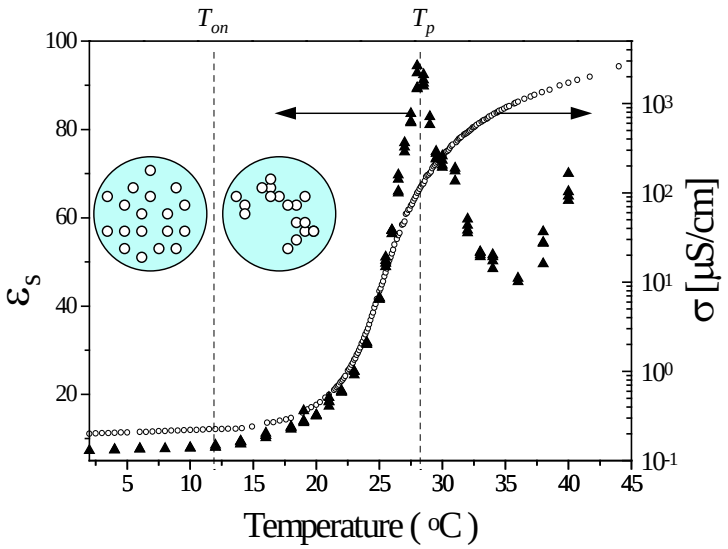

Figure 7. The percolation behavior in AOT–water–decane microemulsion (17.5:21.3:61.2 vol%) is manifested by the temperature dependences of the static dielectric permittivity ε_s (▲ left axis) and conductivity σ (○ right axis). T_{on} is the temperature of the percolation onset; T_p is the temperature of the percolation threshold. Insets are schematic presentations of the microemulsion structure far below percolation and at the percolation onset. (Reproduced with permission from Ref. 149. Copyright 1998, Elsevier Science B.V.)

Dielectric Spectroscopy can be successful in providing unique information about the dynamics and structure of microemulsions on various spatial and temporal scales. Being sensitive to percolation, *DS* is expected to provide unambiguous conclusions concerning the stochastic type, the long time scale cooperative dynamics and the imposed geometric restrictions of molecular motions before, during and after the percolation threshold in microemulsions. It also can give valuable information about fractal dimensions and sizes of the percolation clusters.

The percolation behavior is manifested by the rapid increase in the dc-electrical conductivity σ and the static dielectric permittivity ε_s as the system approaches the percolation threshold (Figure 7).

The dielectric relaxation properties in a sodium bis(2-ethylhexyl) sulfosuccinate (*AOT*) - water - decane microemulsion near the percolation temperature threshold have been investigated in a broad temperature region [47,143,147]. The dielectric measurements of ionic microemulsions were carried out using the *TDS* in a time window with a total time interval of ~ 1μs. It was found that the system exhibits a complex non-exponential relaxation behavior that is strongly temperature dependent (Figure 8).

An interpretation of the results was done in the framework of the dynamic percolation model [148]. According to this model, near the percolation threshold, in addition *to the fast relaxation* related to the dynamics of droplet components ($\tau_1 \cong 1$ ns) [149], there are at least

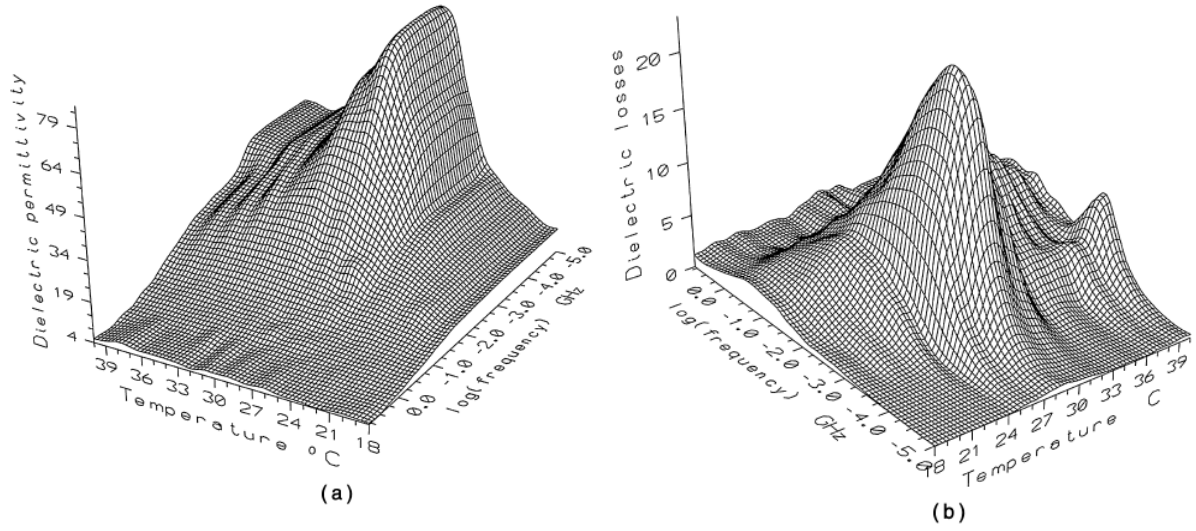

Figure 8. Three-dimensional plots of the frequency and temperature dependence of the dielectric permittivity ε' *(a)* and dielectric losses ε'' *(b)* for AOT–water–decane microemulsion. (Reproduced with permission from Ref. 143. Copyright 1995, The American Physical Society.)

two much longer characteristic time scales. *The longest process* has a characteristic relaxation time greater than a few microseconds and is associated with the rearrangement of the typical percolation cluster. The temporal window of the intermediate process is a function of temperature. This *intermediate process* reflects the *cooperative relaxation phenomenon* associated with the transport of charge carriers along the percolation cluster [148,150,151]. Thus, due to the cooperative nature of relaxation, the *DCF* decay behavior (See Figure 9) contains information regarding the transient cluster morphology at the mesoscale that reflects the dynamical character of percolation.

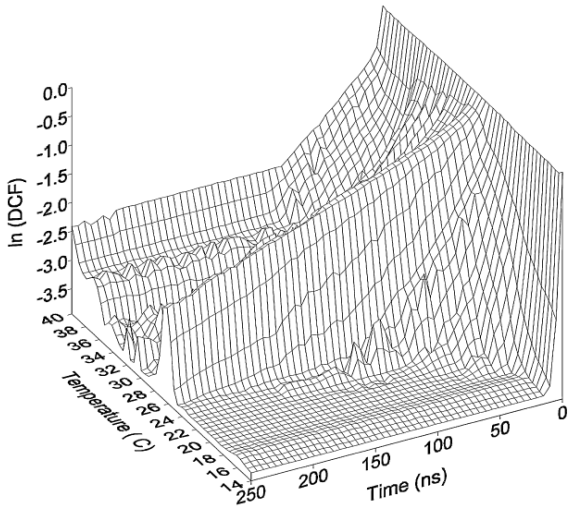

Figure 9. The three-dimensional plot of experimental dipole correlation function versus time and temperature. The percolation threshold temperature T_p=26.5°C. (Reproduced with permission from Ref. 47. Copyright 1996, The American Physical Society.)

The type of the relaxation law seen in time domain is strongly dependent on the distance from the percolation threshold. Figure 10 shows in log-log coordinates that at the percolation onset temperature (~14°C) the relaxation follows a fractional power law: $\Psi(t) \sim (t/\tau_1)^{-\mu}$. By the same token, in the coordinates $\log\Psi$ versus $\log(t/\tau_1)$ in the close vicinity of the percolation threshold T_p=26.5°C, the relaxation law changes from power law to stretched exponential behavior, i.e., $\Psi(t) \sim exp[-(t/\tau_m)^{\nu}]$ (See Figure 11). In the crossover region the relaxation law is considered to be a product of both the power law and stretched exponential terms described by (2.25). The results of the fitting of the experimental dipole correlation functions to Eq.(2.25) are shown in Figure 12 and Figure 13.

One can see (Figure 12) that the magnitude of parameter μ decreases to almost zero as the temperature approaches that of the percolation threshold. This effect confirms the statement mentioned above that at the percolation threshold temperature the behavior of the

dipole correlation function is of the *KWW* type. The stretched parameter ν changes its value from ~0.2 near the percolation onset to ~0.8 in the vicinity of the percolation threshold.

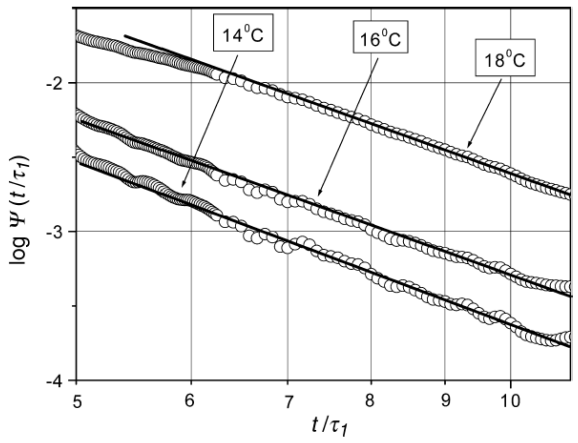

Figure 10. The dipole correlation function $\psi(t/\tau_1)$ demonstrates power-law behavior for the temperature region near the percolation onset (T_{on} = 12°C). (Reproduced with permission from Ref. 2. Copyright 2002, Elsevier Science B.V.)

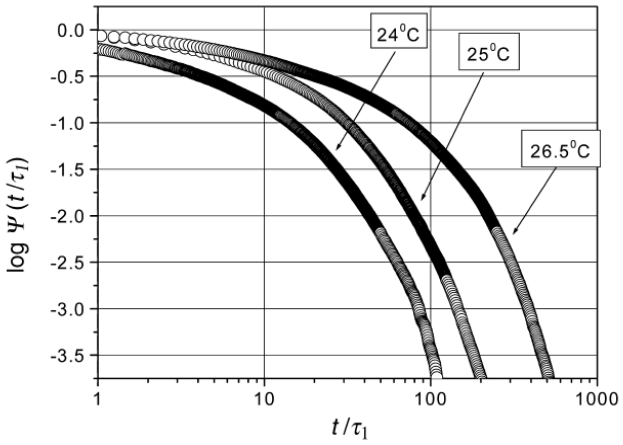

Figure 11. The dipole correlation function $\psi(t/\tau_1)$ demonstrates *KWW* behaviour near the temperature of the percolation threshold (T_p = 26.5°C). (Reproduced with permission from Ref. 2. Copyright 2002, Elsevier Science B.V.)

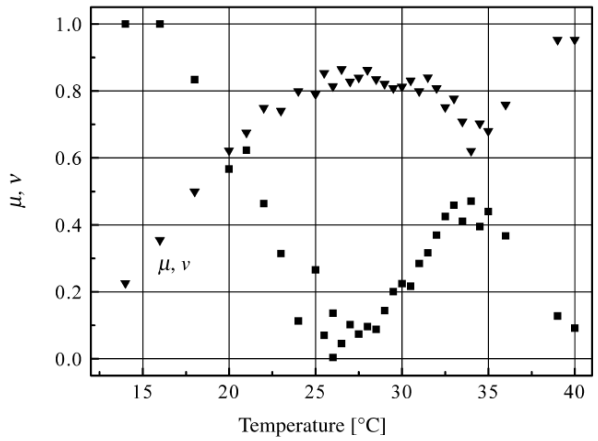

Figure 12. The temperature dependence of the exponents μ (▼) and ν (■) illustrate the transformation of the dipole correlation function $\psi(t/\tau_1)$ from the power-law pattern to the *KWW* behavior at the percolation threshold. (Reproduced with permission from Ref. 2. Copyright 2002, Elsevier Science B.V.)

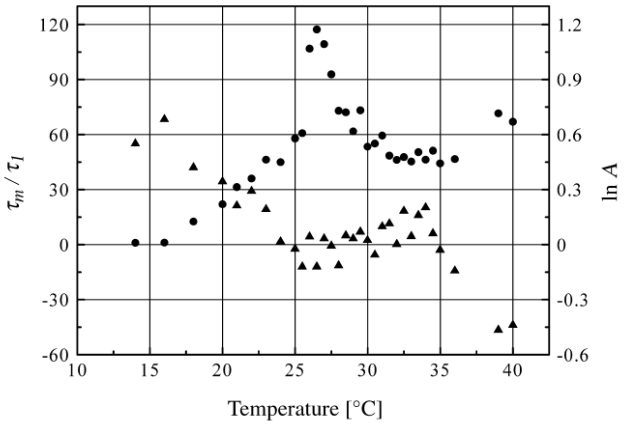

Figure 13. The temperature dependence of the parameter τ_m (● left axis) and A (▲ right axis), obtained by the fitting of the relaxation law (25) to the experimental data. (Reproduced with permission from Ref. 2. Copyright 2002, Elsevier Science B.V.)

Notwithstanding that the value of ν is not equal to zero at percolation onset, note that the stretched exponential term with $\nu = 0.2$ changes insignificantly in the considerable time interval (~1μs) and the decay of the *DCF* $\psi(t)$ is governed mainly by the power law. Figure 13 plots the relaxation times ratio, τ_m / τ_1 and the amplitude A corresponding to the macroscopic relaxation time of the decay function determined by (2.25). Near the percolation threshold, τ_m / τ_1 exhibit a maximum and reflect the well-known *critical slowing down* effect [152]. The description of the mechanism of the cooperative relaxation in the percolation region will be presented in section 5.2.

4.2 Porous materials

Non-Debye dielectric relaxation in porous systems is another example of the dynamic behavior of complex systems on a mesoscale. The dielectric properties of various complex multi-phase systems (borosilicate porous glasses [153-156], sol-gel glasses [157,158], zeolites [159] and porous silicon [160,161]) were studied and analyzed in terms of cooperative dynamics. The dielectric response in porous systems will be considered here in detail using two quite different types of the materials namely: porous glasses and porous silicon.

4.2.1 Porous glasses

The porous silica glasses obtained from sodium borosilicate glasses are defined as bicontinuous random structures of two interpenetrating percolating phases, the solid and the pore networks. The pores in the glasses are connected to each other and the pore size distribution is narrow. The characteristic pore spacing depends on the method of preparation, and can be between 2 and 500 nm [156,162]. A rigid SiO_2 matrix represents the irregular structure of porous glasses. Water can be easily adsorbed on the surface of this matrix. The dielectric relaxation properties of two types of silica glasses have been studied intensively over broad frequency and temperature ranges [153-156]. The typical spectra of the dielectric permittivity and losses associated with the relaxation of water molecules of the adsorptive layer for the studied porous glasses versus frequency and temperature are displayed in Figure 14.

Figure 14 shows that the complex dielectric behavior can be described in terms of the four distributed relaxation processes as follows:

The first relaxation process, which is observed in the low temperature region from –100°C to +10°C is due to the reorientation of the water molecules in ice-like water cluster structures. It was shown that the hindered dynamics of the water molecules located within the pores reflects the interaction of the absorptive layer with the inner surfaces of the porous matrix [153,155];

The second relaxation process has a specific saddle-like shape and is well marked in the temperature range of –50°C to +150°C. This relaxation process is thought to be a kinetic transition due to water molecule reorientation in the vicinity of a defect [155];

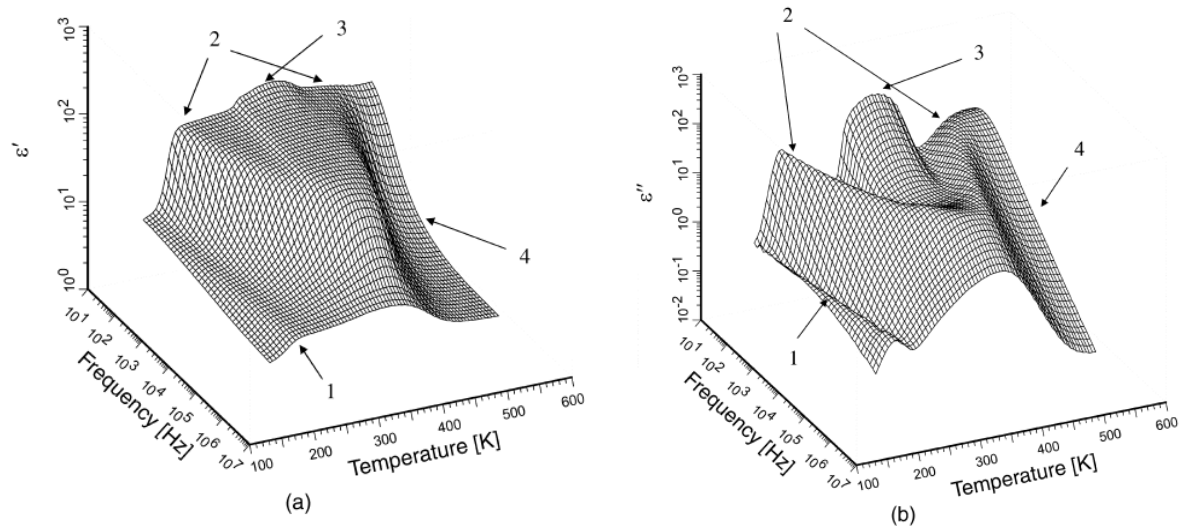

Figure 14. The typical three-dimensional plot of the complex dielectric permittivity real ε' *(a)* and imaginary part ε'' *(b)* versus frequency and temperature for porous glass (sample *E*). All the details of different sample preparation and their properties are presented in Ref. 156. (Reproduced with permission from Ref. 2. Copyright 2002, Elsevier Science B.V.)

The third relaxation process is located in the low-frequency region and the temperature interval 50°C to 100°C. The amplitude of this process essentially decreases when the frequency increases, and the maximum of the dielectric permittivity versus temperature has almost no temperature dependence (Figure 15). Finally, the low-frequency ac-conductivity σ demonstrates an *S-shape* dependency with increasing temperature (Fig. 16), which is typical of percolation [2,143,154]. Note in this regard that at the lowest-frequency limit of the covered frequency band the ac-conductivity can be associated with dc-conductivity σ_0 usually measured at a fixed frequency by traditional conductometry. The dielectric relaxation process here is due to percolation of the apparent dipole moment excitation within the developed

fractal structure of the connected pores [153,154,156].This excitation is associated with the self-diffusion of the charge carriers in the porous net. Note that in distinction from dynamic percolation in ionic microemulsions the percolation in porous glasses appears via the transport of the excitation through the geometrical static fractal structure of the porous medium.

The fourth relaxation process is observed in the high temperature region, above 150°C, where the glasses become remarkably electrically conductive and show an increase of dielectric constant and dielectric losses in the low frequency limit. This relaxation process is most probably related to the interface polarization process as a result of the trapping of free charge carriers at the matrix-air interface inside the sample. It causes a build-up of macroscopic charge separation or space charge with a relatively long temperature independent relaxation time. As shown [153,156], the value of the relaxation time is well correlated to the pore sizes: the larger the pores, the slower the relaxation process. The description of the mechanism of cooperativity in confinement (Process II) and relaxation in the percolation region (Process III) will be presented below.

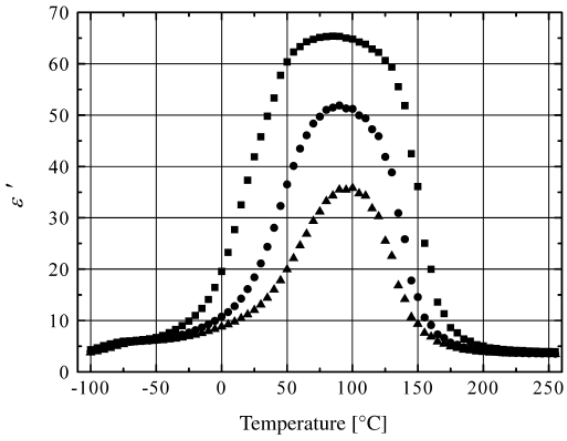

Figure 15. Typical temperature dependence (for sample *E* [156]) of the complex dielectric permittivity of the real part of different frequencies (■ 8.65 kHz; ● 32.4 kHz; ▲ 71.4 kHz). (Reproduced with permission from Ref. 2. Copyright 2002, Elsevier Science B.V.)

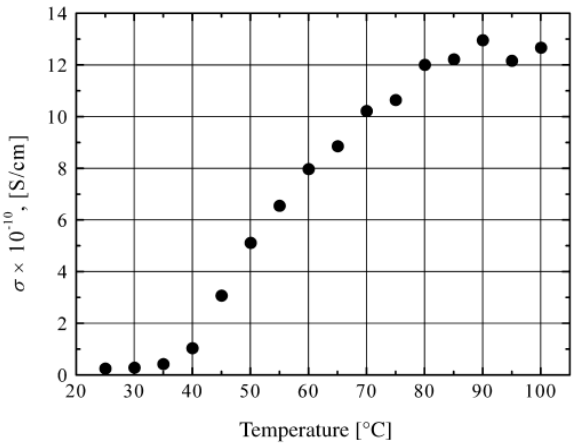

Figure 16. Typical temperature dependence of the low frequency *ac*-conductivity σ of the porous glass sample *E*. (Reproduced with permission from Ref. 2. Copyright 2002, Elsevier Science B.V.)

4.2.2 Porous Silicon

Non-Debye dielectric relaxation was also observed in porous silicon (*PS*) [25, 160,161]. *PS* has attracted much attention, mainly due to its interesting optical and electro-optical properties that can be utilized for device applications [164,165]. So far, most of the activity in this field has focused on the intense visible photoluminescence (*PL*) from nano-*PS* and the underlying physical mechanism that is responsible for the generation of light. In addition, transport and dielectric relaxation phenomena in *PS* have also attracted considerable attention for injection-type *PS* devices. It was mentioned in the previous section that the correlation between the morphology of porous media and their dielectric properties has already been studied [153,154,166]. In many porous media, dielectric response is directly related to the fractality and the nano- and meso-structural properties of these disordered systems [153,156-159]. In principle, one would expect to find a similar correlation between the micro-geometry and the dielectric properties of *PS* media. For example, dc-conductivity measurements demonstrate a dual transport mechanism that has been assigned to thermally activated hopping and exited charged carrier tunneling [167]. As a result, carriers excited to the band tail would give rise to a thermally activated dc-conduction with activation energy of about 0.5 eV [163,168]. This activation energy is less than half the optical band-gap of *PS* deduced from *PL* experiments [164]. The ac-conductivity measurements in *PS* revealed complex transport properties due to a random walk in fractal geometry and thermally activated hopping, as in the case of dc-conductivity [163]. Therefore, it is commonly accepted that both the nano-geometry, the nature of the Si nanocrystallites that form the *PS* medium and their surfaces as well as the host matrix all contribute to the electrical and optical properties of *PS*.

The dielectric relaxation properties in nano-*PS* with different thicknesses have been investigated in broad frequency and temperature regions [160,161]. The dielectric properties of the *PS* samples were measured in the 20 Hz to 1MHz frequency range and in the 173 to 493 K temperature interval. For all the dielectric measurements, the amplitude of a sinusoidal *ac* voltage source was kept constant at 1V so that the average electric field across our sample was about hundreds V/cm depending on the sample thickness. It was verified that the response was linear with respect to the ac voltage amplitude such that a linear response analysis could be utilized for our sample.

Three-dimensional plots of both the measured real part ε' and the imaginary part ε'' of the complex dielectric permittivity versus frequency and temperature for 20 μm thickness *PS*

sample are shown in Figure 17a, b. From the figure one can identify three distinct processes, marked by I, II and III, defined as follows:

Low temperature process I: This process extends over the low temperatures (170 to 270 K). Despite the fact that both the real and imaginary parts of the dielectric function display this process, it can be appreciated most by looking at ε'' at high frequencies and low temperatures where the local maximum, which shifted to higher frequencies with increasing temperature, can be easily detected.

Process I represents an existence of additional groups of exited states in *PS*, which contribute to a thermally activated transport processes [160].

Mid temperature process II: This process extends over the mid-range temperatures (300 to 400K) and over low to moderate frequencies (up to 10^5 Hz). The mid temperature process was associated with the percolation of charge excitation within the developed fractal structure of connected pores at low frequencies and with an activated hopping conductivity between neighboring Si crystallites at high-frequency tail [160].

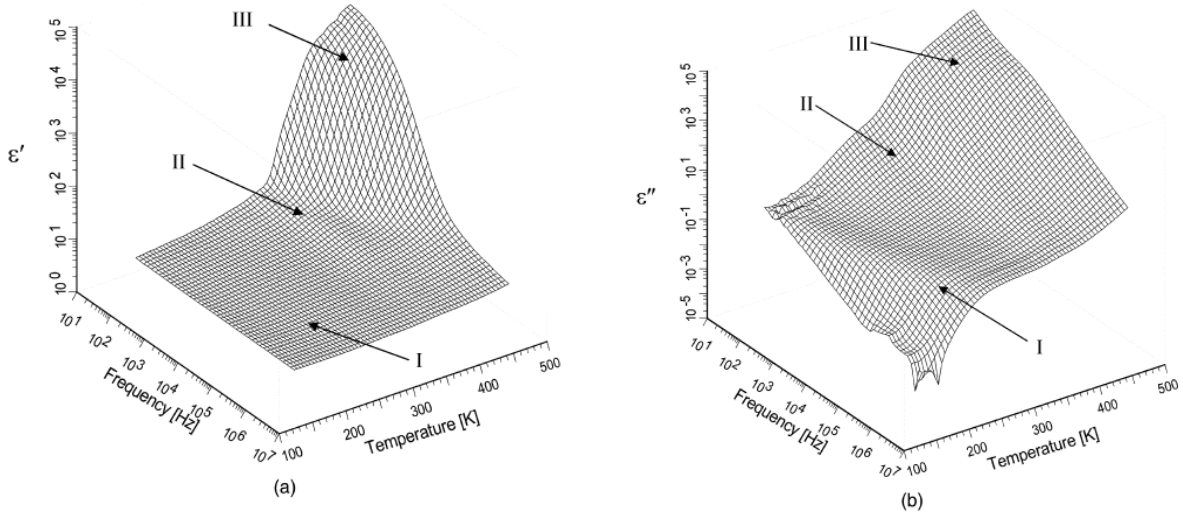

Figure 17. Three-dimensional plots of the frequency and temperature dependence of the real ε' (a) and imaginary part ε'' (b) of the complex dielectric permittivity for the 20 μm *PS* sample. (Reproduced with permission from Ref. 2. Copyright 2002, Elsevier Science B.V.)

High temperature process III: This process is very significant at high temperatures (>400 K). Its amplitude increases very rapidly with decreasing frequency for both the real and the imaginary part of the dielectric function. One of the sources of its behavior is a large dc-conductivity of the sample that appears at high-temperatures.

Similar processes were also observed for the 30 μm thickness samples. The detailed description of the mechanism of the mid temperature process in the percolation region and porosity determination in PS will be presented below.

4.3 Ferroelectric crystals

Amongst the perovskite family of ferroelectrics KTN crystals ($KTa_{1-x}Nb_xO_3$) have attracted great interest both as model systems and for their optical properties. They were first systematically studied in 1959 [169] and a complete microscopic description of the ferroelectric phase transition was given in 2001 [170]. They display both displacive-like and order disorder-like properties [171-174]. For niobium (Nb) concentrations of $x > 0.2$ the ferroelectric phase transition is of the first order and follows the linear rule for ferroelectric phase transition temperature $T_c \approx 682x$ [175]. At the ferroelectric phase transition the crystal structure is transformed from cubic to tetragonal. Further cooling incurs two additional structural transitions: tetragonal to orthorhombic, and orthorhombic to rhombohedral [175]. It was recently shown that the interaction of the off-centre Nb ion with the soft mode phonon of the crystal in fact governs the phase transition [170]. At the phase transition the distortion of the crystal lattice caused by the off-centre position of the Nb ion leads to the creation of virtual dipoles in the crystal lattice which are randomly distributed throughout the crystal. The resultant local fields strongly polarize the lattice leading to long-range cooperativity, frequently of length scales 1000-10000 Å [176], indicative of the ferroelectric phase. The addition of transition metal ions to this system leads to further novel properties. Of particular interest is the addition of small quantities of copper (Cu) ions. Copper, in small concentrations, approximately 1.5×10^{-4} molar concentration, is known to greatly enhance the photorefractive effect in these crystals [177], leading to important electroholographic applications [178]. Generally Cu ions occupy the potassium site in the lattice and sit off-centre. This virtual dipole is the source of further relaxations in the crystal.

The dielectric behavior of copper-doped and pure KTN crystals were compared in wide temperature and frequency ranges in order to study the effect of such small Cu ion concentrations on the dielectric landscape [179]. The two studied KTN crystals were grown using the top seeded solution growth method [180]. The Ta/Nb ratio in both crystals was estimated by Perry's linear relation [175] linking T_c, to the concentration of Nb, $T_c = 682x + 33.2$, and was found to be approximately 62/38 per mole. The first crystal (crystal #1) was doped with copper. The doping level was 2% in the flux yielding approximately

1.5×10^{-4} per mole in the grown crystal. The second crystal (crystal #2) was a pure KTN crystal. Samples of 1x1x2 mm^3 were cut from the grown bole along the crystallographic [001] axes. The x-y faces of the samples (perpendicular to the growth direction z) were polished and coated with gold electrodes. Cu concentration was established by using Inductively Coupled Plasma Optical Emission Spectrometry (ICP-OES) [181] on similarly grown crystals with the same flux concentrations of Cu. It was found that 2% Cu in the flux produced a nearly constant concentration of 1.5×10^{-4} per mole independent of the ratios of other constituents, with an accuracy of 0.2%.

Dielectric measurements were carried out in the frequency range of $10^{-2} – 10^{6}$ Hz and the temperature interval 133 K to 473 K [179]. The crystals were cooled from 297 K to 190 K with a temperature step of 4 K. In the region of the phase transition, 292 K to 297 K, the temperature step was reduced to 0.5 K. Reheating from 190 K to 440 K was done with a step of 5 K. As before, in the region of the ferroelectric phase transition the step was reduced to 0.5 K. The dielectric landscape of crystal #1 is presented in Figure 18.

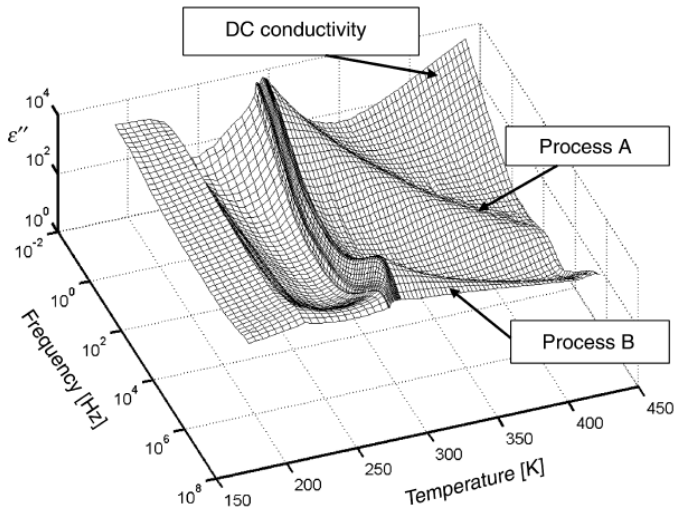

Figure 18. The dielectric losses, *ε''*, for crystal #1. The three phase transitions are evident at T=295.6 K, 291.1 K and 230 K respectively. (Reproduced with permission from Ref. 179. Copyright 2004, The American Physical Society.)

The complex dielectric response of crystal #1 can be described in terms of a number of distributed dynamic processes separated by different frequency and temperature ranges. The ferroelectric phase transition is observed at 295.6 K. It is followed by tetragonal to rhombohedral transitions occurring at 291.1 K and 230 K respectively. A comparison of these transition temperatures with the undoped crystal #2 revealed that the second and third

transitions (tetragonal to orthorhombic and orthorhombic to rhombohedral) were shifted by approximately 40 K towards the lower temperatures (See Figure 19).

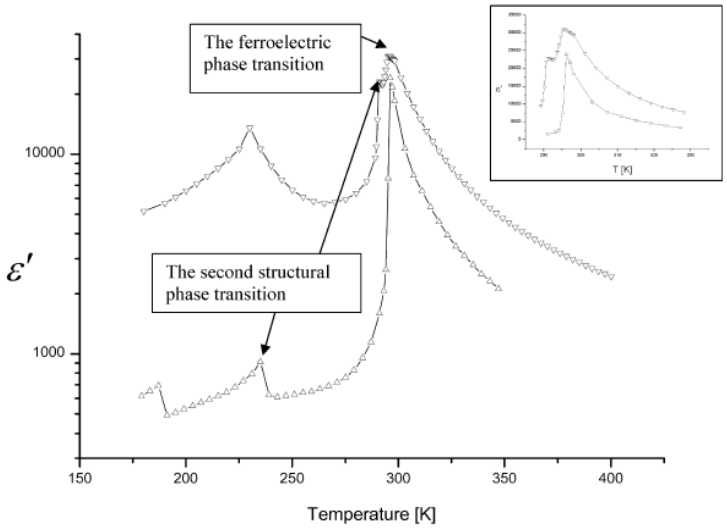

Figure 19. The dielectric permittivity of crystals #1(∇) and #2 (Δ) measured at 12 Hz. The shift in the second and third phase transition temperatures, due to Cu ion doping, is clearly evident. The insert shows the detail of the ferroelectric phase transition in both crystals. (Reproduced with permission from Ref. 257. Copyright 2005, Elsevier Science B.V.)

In the paraelectric phase, above 295 K, there is a thermally activated process (process **A**) starting in the low frequencies at the phase transition and shifting towards higher frequencies as the temperature increases. The quantitative nature of Process **A** was established by examining the temperature dependence of τ^A, obtained as the inverse value of the characteristic frequency $f_m(T)$ along the crest representing process A in the $\varepsilon''(T,f)$ landscape [6]. It was found to be Arrhenius in nature with activation energy of $E_a^A = 0.94 \pm 0.01\, eV$ and the high temperature limit of the relaxation time τ_0^A=1.7±0.4 x 10^{-15} s. Additionally, it was found to be correlated with the well-pronounced dc-conductivity. The dc-conductivity, σ, was found to follow Arrhenius behavior, namely, $\sigma = \sigma_0 \exp(-E_\sigma / k_B T)$, with an activation energy of E_σ =0.9±0.01 eV and the high temperature limit of conductivity σ_0 = 42 ± 7 sm^{-1}. The similarity in nature and activation energy of Process **A** and the dc-conductivity suggests that they originate from the same physical mechanism, most likely electron mobility. While Process **A** was observed in both crystal #1 and crystal #2, Process **B** was observed only in crystal # 1 (see Fig. 20). Process **B** was observed to pass through all three phase transitions and it was found to be non-Arrhenius with distinct changes in its relaxation behavior

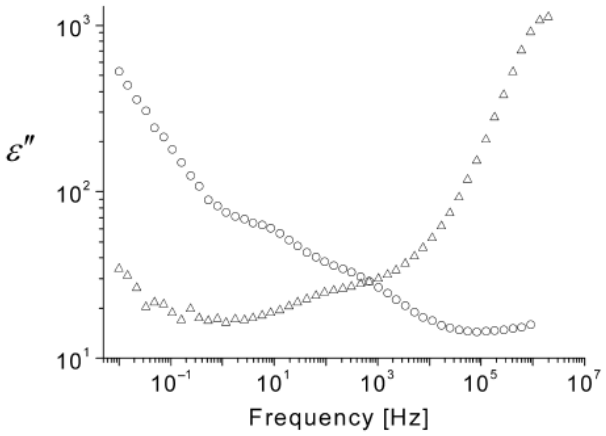

Figure 20. A comparison of the dielectric losses measured at T=250 K: Δ represents crystal #1 (KTN doped with Cu ions) and ○ represents crystal #2 (pure KTN). (Reproduced with permission from Ref. 179. Copyright 2004, The American Physical Society.)

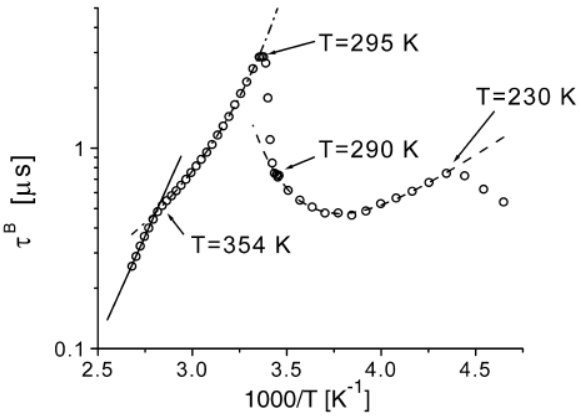

Figure 21. The characteristic relaxation times for Process **B**. On the figure are marked the three phase transitions and the critical cross-over temperature, T=354 K, between Ahrrenius and VFT behaviours. The circles are the experimental data and the lines are the fitting functions; Ahrrenius, VFT and "Saddle-like" [78,179]. (Reproduced with permission from Ref. 257. Copyright 2005, Elsevier Science B.V.)

delineated by the phase transitions. In the same manner as for Process **A** relaxation time τ^B was extracted from the peak maximum of the dielectric losses, *ε"(ω,T),* (Figure 21).

In the high temperature range, above 354K, Process **B** exhibits Arrhenius behavior with an activation energy E_a^B=0.37 ± 0.01 eV and τ_0^B = 2.8 ± 0.9 x 10^{-12} s. Below T_x=354K Process **B** obeys a Vogel-Fulcher-Tammann (*VFT*) relaxation in which τ^B is given by (2.28) $\ln(\tau^B) = \ln(\tau_0^B) + \frac{E_{VFT}}{k_B(T - T_{VFT})}$ with T_{VFT}=228K, and E_{VFT} = 0.02 eV. Following the onset of the ferroelectric phase transition at T_c=295.6 K, τ^B decreases until it reaches a minimum at 264K, exhibiting a small cusp at the second (tetragonal to orthorhombic) phase transition. Upon further cooling τ^B increases until it reaches a maximum at the third (orthorhombic to rhombohedral) transition at 230K, exhibiting a "saddle" [78] that will be discussed in detail below.

4.4 H-bonding Liquids

The study of slow dynamics in glass forming liquids is currently a significant challenge in the research field of soft condensed matter science [182-186]. Hydrogen bonding liquids and their mixtures occupy a special place among complex systems due to existence of directed H-bonds (in contrast to van der Waals and ionic systems) that can be rearranged relatively easily (in contrast to covalent bonds). Although an enormous amount of literature exists which relates to the investigation of hydrogen-bonding systems (See for example [3,183,185]) there is still a lack of clear understanding of their dynamics, structure and glass transitions. Among them, glycerol ($C_3H_8O_3$) [17,74,187-189] and its mixtures with water [190] is widely used as excellent model to study their cooperative dynamics.

Usually, glycerol exists only in liquid, supercooled, or glassy states. However, after special treatment pure dehydrated glycerol can be crystallized [191,192]. Uncrystallized glycerol is a common system used for studying glass-forming dynamics [3,184,187-189,193-195] while crystallized glycerol, until now, has not been investigated.

Under normal conditions glycerol does not undergo crystallization but rather during cooling it becomes a supercooled liquid which can be vitrified [184,187,196,197] at T_g=190 K. In contrast, anhydrous glycerol, cooled down below the glass transition point T_g and then slowly heated up, can be crystallized. However, crystallization of glycerol is a very unusual and unstable process, which depends on the temperature history and impurities of the sample. The main features of glycerol crystallization were studied [186] by comparing the glass-forming dynamics of anhydrous glycerol (Sample A) with those of glycerol that was not specially treated to prevent water absorption (Sample B). To reach crystallization, sample *A* was cooled from room temperature to 133 K. Then measurements of the complex dielectric permittivity $\varepsilon^*(\omega)$ were performed by a Novocontrol Alpha Analyzer in the frequency interval 0.01 Hz - 3 MHz and the temperature range 133 K - 325 K (See Figure 22). Thus, overall experimental time was 30 h and average heating rate was about 0.1K min^{-1}. Considerable changes in $\varepsilon^*(\omega)$ behavior in the measured frequency range are observed in the temperature interval from 263 K to 293 K. The transition at 293 K is known as the glycerol melting point [198]. Thus, the transition near 263 K is thought to be attributed to the glycerol crystallization.

Note that the relaxation process (I) of the supercooled glycerol in this temperature interval disappears and the relaxation process (II), with a reduced strength, appears in the low frequency region.

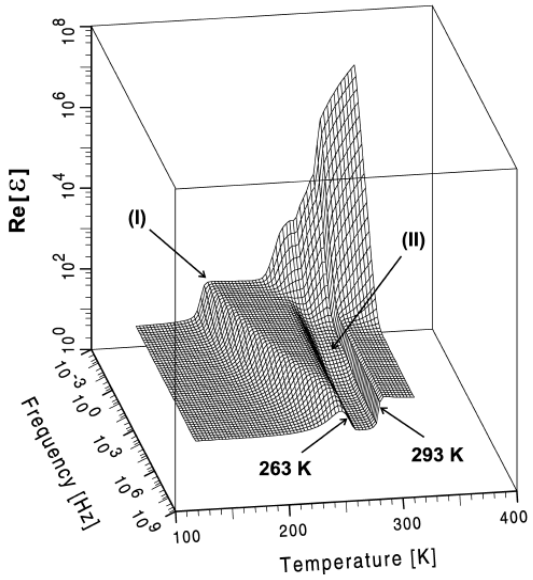

Figure 22. A three-dimensional plot representing the real part of $\varepsilon'(\omega)$ for sample *A*. The arrows mark the crystallization temperature (T_x =263 K), the melting point (T_m=293 K), and the principal relaxation process, before (I) and after (II) the crystallization. (Reproduced with permission from Ref. 186. Copyright 2003, The American Physical Society.)

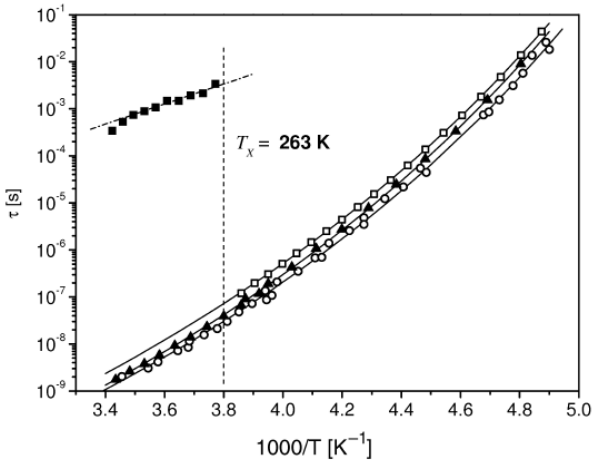

Figure 23. Sample *A* before (unfilled boxes) and after (filled boxes) the crystallization compared with sample *B* (triangles), and literature data [195] (circles). In the supercooled phase all samples obey a VFT law (full lines), while the relaxation process in sample *A* above 263 K obeys an Arrhenius law (dash-dotted line). (Reproduced with permission from Ref. 186. Copyright 2003, The American Physical Society.)

The data presented in Fig.23 were analyzed as a set of isothermal spectra in the framework of (2.21)

$$\varepsilon^*(f) = \varepsilon_\infty + \frac{\varepsilon_s - \varepsilon_\infty}{(1+(i\omega\tau)^\alpha)^\beta}$$

It is remarkable that in the liquid and supercooled phase glycerol exhibits unsymmetrical relaxation peak broadening ($\alpha \approx 1$, $\beta \approx 0.6$) whereas in the case of process (II) the broadening is a rather symmetric one ($0.6 \leq \alpha \leq 0.7$, β =1). The Arrhenius plot in Figure 23 shows that relaxation dynamics in the supercooled glycerol phase before crystallization (I) obey the *VFT* relationship while after crystallization (II) follow Arrhenius law. Note, that in the considered frequency and temperature landscape, another low frequency process related to the crystallization is observed. Unfortunately, it was not resolved properly in the mentioned study [186].

The *VFT* behavior of supercooled glycerol is well known from studies of liquid and supercooled glycerol [3,186-190] while the Arrhenius dependence of dielectric relaxation

time is more relevant for crystals. For example, the temperature dependence of dielectric relaxation time of ice I also obeyes Arrhenius law with the activation energy about 60 kJ·mol^{-1}[198,199].

Therefore, the observed process (I) could be related to cooperative dynamics of glycerol in the supercooled phase while process (II) is most likely related to the crystalline phase of glycerol and is the result, similar to water, of the mobility of defects in the crystalline lattice [200]. The temperature dependence of the relaxation time for the dehydrated glycerol is compared in Figure 23 with those for the usual behavior of glycerol, which has absorbed some water from the atmosphere.

In Figure 23, we compared temperature dependencies of fitted relaxation time for samples *A* and *B* and data recently published by Lunkenheimer and Loidl [195]. The fitting yields that the process (I) in the supercooled phase for sample *A*, the relaxation in sample *B*, and literature data [195], all obey the *VFT* law $\tau_{\max} = \tau_v \exp\{DT_v/(T - T_v)\}$ where T_v is the Vogel-Fulcher temperature, τ_v is the pre-exponential factor, and *D* is the fragility parameter. From the data presented in Figure 23 one can see that values of the *VFT* temperature T_v and fragility *D* are very close for all the samples where $D = 22\pm2$ and $T_v = 122\pm2$ K, while the preexponential factors τ_v are remarkably different. For the anhydrous sample *A*, $\tau_v = 3.93\times10^{-16}$ s, for sample *B*, $\tau_v = 2.3\times10^{-16}$ s, while for the literature data [195] $\tau_v = 1.73\times10^{-16}$ s. Taking into account the fact that sample *A* was specially protected from water absorption, it is strongly suspected that this significant difference in τ_v is caused by the water absorbed from the atmosphere. This observation signifies that even very small water content can result in significantly different dynamics in the supercooled phase for the anhydrous glycerol and for the glycerol samples usually studied [186].

As mentioned above, the frequency dependence of complex dielectric permittivity (ε^*) of the main relaxation process of glycerol [17,186] can be described by the Cole-Davidson (*CD*) empirical function (See (2.21) with $\alpha = 1$, $0 < \beta_{CD} \leq 1$). In that case τ_{CD} is the relaxation time which has non-Arrhenius type temperature dependence for glycerol (See Figure 23). Another well known possibility is to fit the *BDS* spectra of glycerol in time domain using the *KWW* relaxation function (2.23) $\phi(t)$ (See Figure 24).

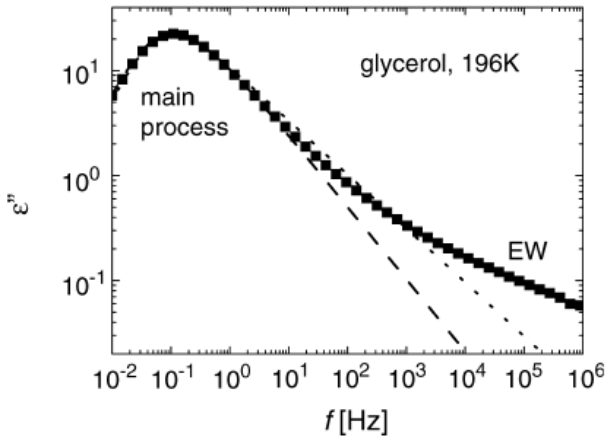

Figure 24. The imaginary parts of the dielectric spectrum for anhydrous glycerol in the supercooled state at 196 K [186]. The dotted and dashed line show descriptions of the main relaxation process by CD [Eq. (21)] with τ_{CD} = 2.61 s, $\Delta\varepsilon$ = 63.9 and β_{CD} = 0.51) and KWW [Eq. (23)] with τ_K = 1.23 s, $\Delta\varepsilon$ = 62.0 and β_K = 0.69) functions, respectively. (The half-width of the loss curve were fixed for both CD and KWW functions.) (Reproduced with permission from Ref. 208. Copyright 2005, American Chemical Society.)

The *CD* function predicts the dielectric loss (ε") of glycerol to follow the power law ε"~ $f^{\beta_{CD}}$ towards the high frequencies ($f >> f_{\max}$), where f_{max} is the frequency corresponding to the dielectric loss peak. However, the high frequency experimental data in Figure 24 demonstrate a significant deviation from the expected asymptotic behavior both for *CD* and *KWW* functions. The finding of ε" values larger than predicted by the spectral function of the main relaxation are known as the excess wing (*EW*). Although there is no unique interpretation of the *EW*, it is known that this phenomenon is a property of many glass-forming systems [195,201-203]. Note that deviations from a power law slope for ε" were also observed for pure water [204-206]. These features were treated as an additional Debye type relaxation process without any relation to glass-forming properties. However, with given glass forming properties of water, they can be discussed as the *EW* feature as well. There is some discussion [201] that the *EW* is most probably a Johari-Goldstein (*JG*) [207] mode. However, there are still open questions because analysis of pressure and temperature effects leads to the conclusion that *EW* and *JG* modes "cannot be treated on the same footing" [202]. The non-Arrhenius temperature dependence of the *EW* found recently [203] is in contradiction to the original idea of Johari and Goldstein who argued, "the Arrhenius plots in the secondary relaxation region are linear" [207]. Thus the relaxation mechanism of the *EW* is still unclear, and it would be helpful to study how the water concentration in glycerol

influences the relaxation dynamics of the mixture, since the *EW* could be related to the feature of H-bond networks of glycerol that are being affected by the presence of water.

The typical results of recent *BDS* studies of glycerol-water mixtures of 75 mol% of glycerol at different temperatures are presented in Figure 25 [208]. Figure 26 shows that the temperature dependencies of the main relaxation process in the terms of $\tau_{\max} = 1/(2\pi f_{\max})$ for concentrations from 100 to 40 mol% of glycerol were well described by the *VFT* law.

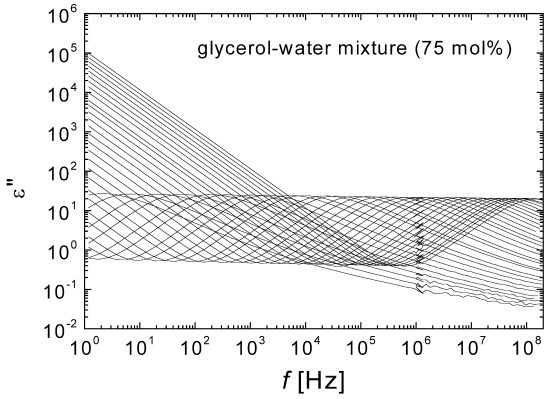

Figure 25. The imaginary parts of the dielectric spectra for a glycerol–water mixture (75 mol%) at various temperatures from 197 to 290 K with an interval of 3 K. (Reproduced with permission from Ref. 208. Copyright 2005, American Chemical Society.)

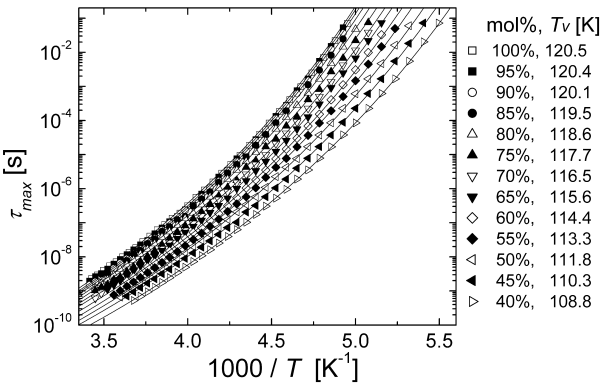

Figure 26. Temperature dependence of $\tau_{\max} = 1/(2\pi f_{\max})$ for a glycerol sample and its mixtures with water. The solid curves show the description by the VFT model, where values of the Vogel–Fulcher temperature (T_v) are shown with the legend. The preexponential factor (τ_v) is almost independent with concentration: ln (τ_v) = –35.9 for 100 mol% of glycerol, –36.1 for 95 to 65%, –36.2 for 60%, –36.3 for 60 to 45% and –36.4 for 40 mol% of glycerol–water mixtures. D = 22.7 for all concentrations presented here. (Reproduced with permission from Ref. 208. Copyright 2005, American Chemical Society.)

It is worth noting that value of D was the same for all concentrations presented in Figure 26 and values of τ_v were also almost the same in this concentration range.

Let us start the examination of the dynamics of glycerol-water mixtures with an inspection of the main dielectric loss peak $\varepsilon"_{max} = \varepsilon"(f_{max})$ with f_{max} as the characteristic frequency that was observed in the considered experimental ranges for glycerol and its mixtures with water. Figure 27 presents a so-called "master plot" that presents the normalized plots of $\varepsilon"(f) / \varepsilon"_{max}$ versus the dimensionless variable f / f_{max}. Namely, each data point in the dielectric spectrum was normalized by only one point such as the loss peak. It is remarkable

that for all temperatures, the dielectric spectra of glycerol traced the same single curve (Figure 27a). This indicates that both the *EW* and low frequency contribution of dc-conductivity follow the same *VFT* temperature dependence of the main relaxation process (Figure 25). In the case of glycerol-water mixtures for concentrations from 60 up to 95 mol% of glycerol (e.g., Figure 27b), the master plots are similar to those presented in Figure 27a for glycerol. These results demonstrate that the *EW* and the main dielectric relaxation process have the same dependency on the composition of the glycerol-water mixture over the comparatively wide range of concentrations: from 60 to 100 mol%. This observation indicates that the *EW*, the main relaxation process and dc-conductivity in these mixtures most probably have the same origin.

Further decrease of glycerol content caused the universality in the master plot to disappear. At 55 mol% or lower concentrations of glycerol, a different behavior of the main

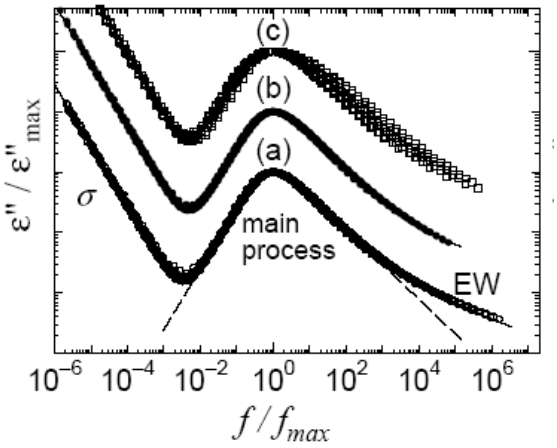

Figure 27. Master plots of the imaginary parts of the dielectric spectra for 100 mol% (a), 75 mol% (b), and 35 mol% (c) of glycerol measured in the temperature intervals 202–292 K, 197–290 K, and 176–221 K, respectively. The dashed line represents CD law with β_{CD} = 0.58. (Reproduced with permission from Ref. 208. Copyright 2005, American Chemical Society.)

dielectric relaxation and the *EW* was observed (e.g., Figure 27c). This region with small glycerol molar content has been investigated in detail by Sudo et al. [190] who ascribed the main and secondary relaxation processes to the relaxation dynamics of the so-called cooperative domains of glycerol and water, respectively. The consideration of the mesoscopic dynamics and glycerol and water glycerol-water mixtures results will be discussed in detail in later sections.

5 Cooperative dynamic and scaling phenomena in disordered systems

Following the general plan of our tutorial, we will discuss here a universal view of scaling which is widely employed in modern dielectric spectroscopy. We will show how this concept can be applied to the description of disordered materials and how these ideas can be useful in the determination of the topological parameters of these systems.

5.1 Static percolation in porous materials, Fractal concept and porosity determination

In this section, we will consider in more detail the non-Debye dielectric response associated with percolation in porous disordered materials: silica glasses and porous silicon where the pores form topologically connected pore channels. The movement of charge carriers along the inner pore surface results in a transfer of the electric excitation within the channels along random paths [154]. Note that in the general case such transfers through the porous medium can occur even in the case of closed pores, which are topologically not connected one to another. However, the distance between the neighboring pores filled with the dielectric or conductive material should be small enough in order to provide “physical” pore coupling via the electric interaction.

It was shown that disordered porous media can been adequately described by the fractal concept, where the self–similar fractal geometry of the porous matrix and the corresponding paths of electric excitation govern the scaling properties of the *DCF* $\Psi(t)$ (See Relationship (2.22)) [154,209]. In this regard we will use the theory of electronic energy transfer dynamics developed by Klafter, Blumen and Shlesinger [210,211], where a transfer of the excitation of a donor molecule to an acceptor molecule in various condensed media through many parallel channels was considered.

A detailed description of the relaxation mechanism associated with an excitation transfer based on a recursive (regular) fractal model was introduced earlier [47], where it was applied for the cooperative relaxation of ionic microemulsions at percolation.

According to this model, an elementary act of the excitation transfer along the length L_j is described by the microscopic relaxation function $g(z/z_j)$, where L_j is the "effective" length of a channel of the relaxation in the j-th stage of self-similarity. In this function, z_j is a dimensional variable characterizing the j-th stage of the self-similarity of the fractal system

considered, z is the dimensionless time, $z = t/\tau$, where the parameter τ is the minimal relaxation time needed for an excitation to hop from one excitation center to its nearest neighbor.

The following assumption is invoked: $z_j = aL_j$, where a is a coefficient of proportionality. For each stage of the self-similarity j, the time of relaxation $\tau_j = \tau z_j$ is proportional to the length L_j. From fractal geometry [212,213] L_j can be expressed as

$$L_j = lk^j, \tag{5.1}$$

where l is the minimal scale and k is a scaling factor ($k > 1$). We assume that the total number of activation centers located along the segment L_j also obeys the scaling law

$$\boldsymbol{n_j = n_0\ p^j}, \tag{5.2}$$

where p is the scaling factor ($p > 1$), and n_0 is the number of the nearest neighbors near the selected center (i.e., $j = 0$).

The macroscopic correlation function can be expressed as a product of the relaxation functions $g(z/z_j)$ for all stages of self-similarity of the fractal system considered [47,154]

$$\Psi(z) = \prod_{j=0}^{N}\left[g\left(z / z_j\right)\right]^{n_j} = \prod_{j=0}^{N}\left[g\left(Z\xi^j\right)\right]^{n_0 p^j}, \tag{5.3}$$

where $Z = t/al\tau$; $\xi = 1/k$ and $N = \frac{1}{\ln k}\ln(L_N / l)$. Here L_N is the finite geometrical size of the fractal cluster and N refers to the last stage of self-similarity.

The estimations of the product (5.3) for various values of $\xi < 1$ and $p > 1$ are given in Ref.47. The results of the calculations may be written in the form of a modified Kohlrausch-Williams-Wats (*KWW*) stretched-exponential relaxation law:

$$\Psi(Z)/\Psi(0) = \exp\left[-\Gamma(\nu)Z^{\nu} + B(\nu)Z\right], \tag{5.4}$$

where the parameters $\Gamma(\nu)$ and $B(\nu)$ are given by

$$\Gamma(\nu) = \frac{n_0}{\ln(1/\xi)} \int_0^\infty y^{-\nu} \left| \frac{g'(y)}{g(y)} \right| dy \quad , \tag{5.5}$$

$$B(\nu) = \frac{n_0 a_1}{ln(1/\xi)(1-\nu)} \varepsilon^{1-\nu} \quad . \tag{5.6}$$

Here

$$\nu = \ln p / \ln(1/\xi) \tag{5.7}$$

with $0 < \nu < 1$, and for $\varepsilon = \xi^N << 1$. We note that the parameter Γ depends on the relaxation function g and affects the macroscopic relaxation time $\tau_M = \tau\, al\Gamma^{-1/\nu}$, and the term $B(\nu)Z$ in the exponent corrects the *KWW* function at large times.

The temporal boundaries of the applicability of (5.4) are determined by the expression:

$$\left| \frac{A_1 n_0}{\bar{g}} \left(\frac{1}{2} - \frac{1}{ln(1/\xi)(1+\nu)} \right) \right| << \frac{t}{al\tau} << \left| \left(\frac{2ln(1/\xi)(2-\nu)}{n_0(2a_2 - a_1^2)\varepsilon^{2-\nu}} \right)^{1/2} \right| \quad . \tag{5.8}$$

The parameters $\bar{g}$, A_1, a_1, and a_2 in (5.4)-(5.8) are related to the asymptotic properties of the elementary relaxation function *g(y)*:

$$g(y) = 1 - a_1 y + a_2 y^2 + \ldots, \qquad \text{for} \quad y << 1 \quad , \tag{5.9}$$

$$g(y) = \bar{g} + A_1 / y + A_2 / y^2 + \ldots, \qquad \text{for} \quad y >> 1 \quad . \tag{5.10}$$

The relationship between the exponent ν, ($\nu = \frac{ln\, p}{ln\, k}$), and the fractal dimension D_p of the paths of excitation transfer may be derived from the proportionality and scaling relations by using an assumption that the fractal is isotropic and has spherical symmetry. The number of pores that are located along a segment of length L_j on the *j*-th step of the self-similarity is $n_j \sim p^j$. The total number of pores in the cluster is $S \sim n_j^d \sim (p^j)^d$, where *d* is the Euclidean dimension, ($d = 3$). The similarity index, η, which determines by how much the linear size of the fractal is enlarged at step *j*, is $\eta \sim L_j \sim k^j$. In this case, we obtain the simple relationship between ν and the fractal dimension D_p as

$$D_p = \ln S / \ln \eta = 3j \ln p / j \ln k = 3\nu \,. \tag{5.11}$$

Further we will focus our attention only on the time dependant behavior of the dipole correlation function $\Psi(t)$ defined by (5.4), that is given by

$$\Psi(t) \approx C(t) \exp[-(t/\tau)^{\nu}] \,, \tag{5.12}$$

where $C(t)$ is the slow growing function of time. By taking into account (5.11) and ignoring the slow variation with time of $C(t)$, we obtain the asymptotic stretched-exponential term

$$\Psi(t) \sim \exp[-(t/\tau)^{D_p/3}] \tag{5.13}$$

that can be further fitted to the experimental correlation functions in order to determine the value of the fractal dimension of the paths of excitation transfer within the porous medium. If the fractal dimension of these paths coincides with the fractal dimension of the pore space, then it can be used in the asymptotic equations derived below for the porosity determination.

5.1.1 Porous glasses

The dielectric relaxation at percolation was analyzed in time domain since the theoretical relaxation model described above is formulated for the dipole correlation function $\Psi(t)$. For this purpose the complex dielectric permittivity data were expressed in terms of the *DCF* using (2.14) and (2.25). Figure 28 shows typical examples of the *DCF*, obtained from the frequency dependence of the complex permittivity at the percolation temperature, corresponding to several porous glasses studied recently [153-156].

As mentioned earlier the typical three-dimensional plots of ε' and ε'' versus frequency and temperature (see Figure 14) indicates the superposition of two processes (percolation and saddle-like) in the vicinity of the percolation. Therefore, in order to separate the long-time percolation process, the *DCF* was fitted as a sum of two functions.

The *KWW* function (5.13) was used for fitting the percolation process and the product (2.25) of the power law and the stretched exponential function (as a more common representation of relaxation in time domain) was applied for the fitting of the additional short-time process.

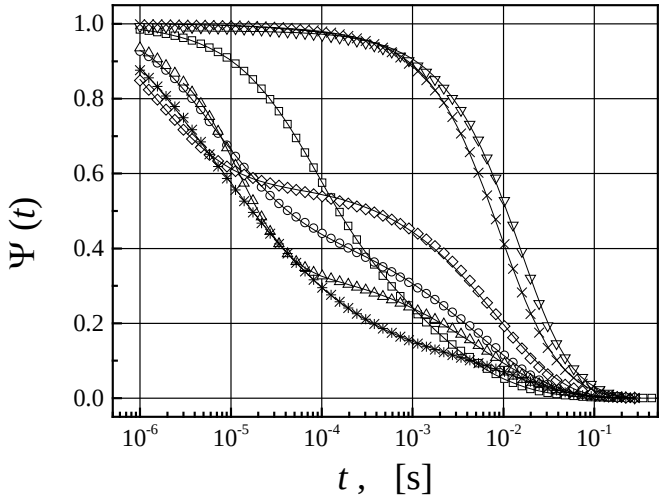

Figure 28. Semilog plot of the dipole correlation $\psi(t)$ of all the samples studied at the temperature corresponding to percolation (□ sample A; ○ sample B; Δ sample C; ∇ sample D; ◊ sample E; × sample F; ∗ sample G). The solid lines are the fitting curves of the sum of the *KWW* and the product of *KWW* and the power-law relaxation function. (Reproduced with permission from Ref. 2. Copyright 2002, Elsevier Science B.V.)

The values obtained for D_p of different porous glasses are presented in the Table 1. The glasses studied differed in their preparation method, which affects the size of the pores, porosity and availability of second silica and ultra-porosity [153-156].

One can see that the fractal dimension of the excitation paths in sample A is close to unity. Topologically, this value of D_p corresponds to the propagation of the excitation along a linear path that may correspond to the presence of second silica within the pores of the sample A. Indeed, the silica gel creates a subsidiary tiny scale matrix with an enlarged number of hydration centers within the pores. Since these centers are distributed in the pore volume, the excitation transmits through the volume and is not related to the hydration centers located on the pore surface of the connective pores. Due to the large number of hydration centers, and the short distance between the neighboring centers, the path can be approximated by a line with a fractal dimension close to unity (See Figure 29a).

Table 1. The values of KWW exponent ν, fractal dimension D_p, porosity Φ_m obtained from the relative mass decrement (A, B, C and D glasses) and BETA (E, F and G glasses) measurements and average porosity $\langle \Phi_p \rangle$ estimated from dielectric spectra for porous glasses samples. *Source*: Reproduced with permission from Ref. 2. Copyright 2002, Elsevier Science B.V.

Sample	ν	D_p	Φ_m	$\langle \Phi_p \rangle$
A	0.33	0.99	0.38	0.33
B	0.63	1.89	0.48	0.47
C	0.44	1.31	0.38	0.37
D	0.83	2.50	0.50	0.68
E	0.65	1.96	0.27	0.49
F	0.80	2.40	0.43	0.63
G	0.73	2.20	0.26	0.56

The fractal dimensions of the excitation paths in samples B, C, and E have values between 1 and 2. In contrast with sample A, the silica gel in these samples has been leached out, i.e. water molecules are adsorbed on the inner pore surface (See the details of different porous glass preparations in ref.156). The values of D_p observed in samples B, C, and E can be explained in one of two ways. On one hand, the surface can be defractalized upon deposition of an adsorbed film of water, which results in the "smoothing" of the surface. On the other hand, the transfer of the excitation in these samples occurs along the inner pore surface from one hydration center to another. The distance between the centers is significantly larger than the small-scale details of the surface texture (See Figure 29b). Therefore, the fractal dimension observed is that of the chords connecting the hydration centers and should be less than 2, which is in agreement with the data obtained from the energy-transform measurements [214,215].

The fractal dimensions of the excitation paths in samples D, F, and G are in the range between 2 and 3. Thus, percolation of the charge carriers (protons) is also moving through the SiO_2 matrix because of the availability of an ultra small porous structure that occurs after special chemical and temperature treatment of the initial glasses [156]. Note that the fractal dimensions discussed here are the fractal dimensions of the excitation transfer paths connecting the hydration centers located on the inner surface of the pores. Due to the low humidity, all of the water molecules absorbed by the materials are bound to these centers.

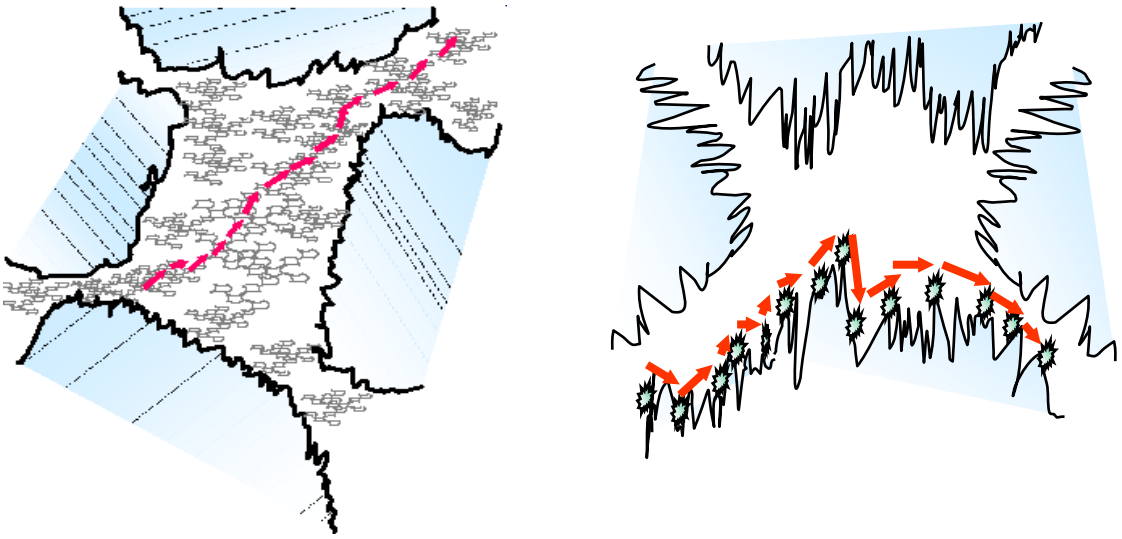

(a) (b)

Figure 29. The schematic presentation of the percolation pass in porous glasses; (a) The glass whose porous are filled with second silica; (b) The porous glasses where the silica gel is leached out.

The paths of the excitation transfer span along the fractal pore surface and "depict" the backbone of clusters formed by the pores on a scale that is larger than the characteristic distance between the hydration centers on the pore surface. Thus, a fractal dimension of the paths D_p approximates the real surface fractal dimension in the considered scale interval. For random porous structures, D_p can be also associated with the fractal dimension D_r of the porous space: $D_p \cong D_r$. Therefore, the fractal dimension D_p can be used for porosity calculations in the framework of the fractal models of the porosity.

The porosity Φ_p of a two-phase solid-pore system can be defined as the ratio of the volume of the empty space, V_p, to the whole volume, V, of a sample [166]:

$$\Phi_p = \frac{V_p}{V} \quad . \tag{5.14}$$

Disordered porous media have been adequately described by the fractal concept [154,216]. It was shown that if the pore space is determined by its fractal structure, the *regular fractal* model could be applied [154]. This implies that for the volume element of linear size Λ, the volume of the pore space is given in units of the characteristic pore size λ by $V_p = G_g (\Lambda / \lambda)^{D_r}$, where D_r is the regular fractal dimension of the porous space, Λ coincides with the upper limit and λ with the lower limit of the self-similarity. The constant G_g is a

geometric factor. Similarly, the volume of the whole sample is scaled as $V = G_g\,(\Lambda/\lambda)^d$, where d is the Euclidean dimension (d=3). Hence, the formula for the macroscopic porosity in terms of the regular fractal model can be derived from (5.14), and is given by:

$$\Phi_p = \left(\frac{\lambda}{\Lambda}\right)^{d-D_r} . \tag{5.15}$$

In general, in order to include more types of porous media the *random fractal* model can be considered [2,154,216]. Randomness can be introduced in the fractal model of a porous medium by the assumption that the ratio of the scaling parameters $\xi=\lambda/\Lambda$ is random in the interval $[\xi_0, 1]$, but the fractal dimension D in this interval is a determined constant. Hence, after statistical averaging (5.15) reads as

$$\left\langle \Phi_p \right\rangle = \int_{\xi_0}^{1} \Phi_p(\xi, D_r)\, w(\xi) d\xi , \tag{5.16}$$

where ξ_0 is the minimal value of the scaling parameter ξ and $w(\xi)d\xi$ measures the probability to find some scaling parameter in the range from ξ to $\xi+d\xi$.

For a percolating medium the generalized exponential pore-size distribution function of the scale for porous medium can be written as

$$w(\xi) \sim \xi^{\alpha_w} \exp(-a_w \xi^{b_w}) . \tag{5.17}$$

This function accounts for the mesoscale region and comprises most of the listed distribution functions [154]. It includes three empirical parameters, α_w, β_w, and a_w. After ascertaining the relationships between these parameters and the properties of anomalous self-diffusion, fractal morphology, and polydispersity of the finite pore-size, physical significance can be assigned to these parameters in the framework of the percolation models [152].

On the length scale, which is larger than the pore sizes, the morphology of the glass porous space can be modeled as a random-packed assembly of clusters formed by pores connected to each other [203,217]. In order to find the macroscopic porosity in such systems we must assume that the pore structure has a fractal character in a rather narrow scale range. Hence, in the interval $[\xi_0, 1]$ the uniform distribution function, $w(\xi) = w_0$, can be chosen as an approximation of the function derived by (5.16). The value of w_0 is determined from the

normalization condition $\int_{\xi_0}^{1} w(\xi)d\xi = 1$, and reads as $w_0 = \frac{1}{1-\xi_0}$. In this approximation, by substituting this uniform distribution function into integral (5.16) and integrating it, we obtain the relationship for the average porosity as

$$\left\langle \Phi_p \right\rangle = \frac{1}{1+d-D_r} \cdot \frac{1-\xi_0^{1+d-D_r}}{1-\xi_0} \quad . \tag{5.18}$$

Taking into account that $\xi_0 << 1$, and $1+d-D_\gamma > 0$ (since topologically $D_\gamma < 3$, and d = 3), we obtain a simple approximate relationship between the average porosity of a glass and the fractal dimension of the pore space, which reads

$$\left\langle \Phi_p \right\rangle \approx \frac{1}{4-D_r} \quad . \tag{5.19}$$

Note that in our approximation, due to the randomized character of the fractal medium the average porosity of the disordered porous glasses determined by (5.19) depends only on the fractal dimension D_r and does not exhibit any scaling behavior. In general, the magnitude of the fractal dimension may also depend on the length scale of a measurement extending from λ to over Λ, where the minimal scale λ and the maximal scale Λ are determined by the measurement technique.

The results of the porosity calculation for different porous glasses using (5.19) together with the fractal dimension determined from dielectric measurements are shown in the last column of Table 1. These values can be compared with the porosity Φ_m determined from the relative mass decrement (A, B, C and D glasses) and BETA (E, F and G glasses) measurements shown in the same Table 1. Note that the values obtained from dielectric spectroscopy coincide with the porosity data obtained from the relative mass decrement method only for samples A, B and C. The porosity values for the other samples obtained through the dielectric measurements are significantly larger. This correlates with the availability of ultra small porous structures with penetrability for the smallest charge carriers (such as protons) [156]. Thus, in the case of a net of super small open pores, the dielectric response is more sensitive and accurate in the determination of real porosity than any other conventional method.

5.1.2 Porous silicon

The detailed analysis of mid-temperature relaxation processes observed in porous silicon was provided recently by using a superposition of two Jonscher terms of the form, $B_1(i\omega)^{u_1-1} + B_2(i\omega)^{u_2-1}$ [160]. The results of our fitting were in good agreement with those of Ben-Chorin *et al*. [163] that were discussed in terms of the transport of charged carriers at the different scales. The high frequency Jonscher exponent was associated with the typical size of the Si nano-crystallites, while the low-frequency (*LF*) exponent was assigned to the transport of charged carriers across a disordered fractal structure of porous silicon [160,161,218,219]. At the same time the mid temperature process II demonstrates several specific features that are similar to those observed in other porous systems discussed in the previous section [153-156]. The amplitude of this process essentially decreases when the frequency increases (Figure 17a). Furthermore, the maximum of the dielectric permittivity versus temperature has almost no temperature dependence. Finally, the low-frequency *ac*-conductivity increases with the increase in temperature and has an *S*-shaped dependency (Figure 30), which is typical for percolation processes [143,154,161]. Thus, we will analyze

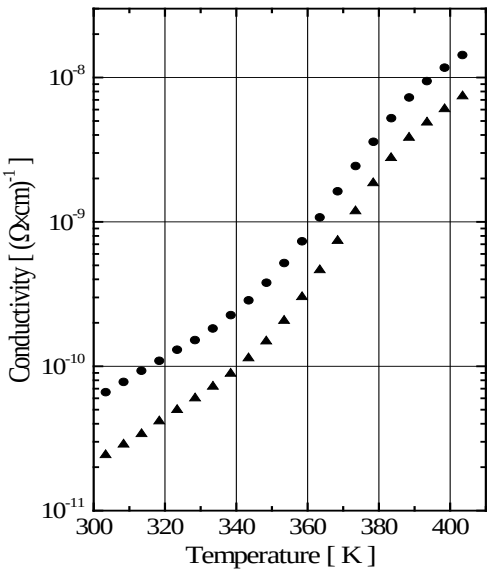

Figure 30. Temperature dependence of the low-frequency conductivity of the 20-μm sample (●), and the 30-μm sample (▲). (Reproduced with permission from Ref. 2. Copyright 2002, Elsevier Science B.V.)

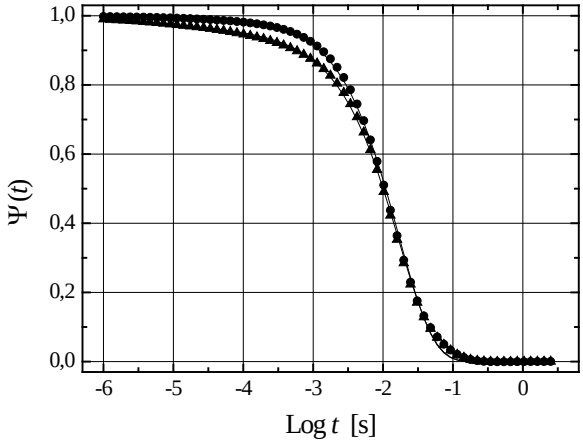

Figure 31. Semilog plot of the macroscopic correlation function of the 20-μm sample (●) and the 30-μm sample (▲) at the temperature corresponding to percolation. The solid lines correspond to the fitting of the experimental data by the KWW relaxation function. (Reproduced with permission from Ref. 2. Copyright 2002, Elsevier Science B.V.)

this process the same way we did for percolation in porous glasses (see section 5.1.1) [2,153-159].

The experimental macroscopic *DCF* for *PS* samples with porous layers of 20 and 30 μm, obtained by inverse Fourier transforms, are shown in Figure 31. The correlation functions then were fitted by *KWW* expression (2.24) with determination of the fractal dimension D_p of the percolation path. Applying the same routine to determine the porosity in other porous systems [154,156-161], the average porosity of the porous silicon was evaluated with the help of relationship (5.19). The results are presented in Table 2. The values of porosity determined from the dipole correlation function analysis are in good agreement with porosity values determined by weight loss measurements during *PS* preparation (before and after the anodization process).

Thus, the non-Debye dielectric behavior in silica glasses and *PS* are similar. These systems exhibit an intermediate temperature percolation process that is associated with the transfer of the electric excitations through the random structures of fractal paths. It was shown that at the mesoscale range the fractal dimension of the complex material morphology (D_r for porous glasses and porous silicon) coincides with the fractal dimension D_p of the path structure. This value can be evaluated by the fitting of the experimental *DCF* to the stretched-exponential relaxation law (5.13).

Table 2. The values of *KWW* exponent ν, fractal dimension D_p, porosity Φ_m obtained from relative mass decrement measurements and average porosity $\langle \Phi_p \rangle$ estimated from dielectric spectra for porous silicon samples of 20 and 30 μm thickness [161]. *Source*: Reproduced with permission from Ref. 2. Copyright 2002, Elsevier Science B.V.

Sample thickness	ν	D_p	Φ_m	$\langle \Phi_p \rangle$
20 μm	0.88	2.64	0.78	0.74
30 μm	0.87	2.61	0.75	0.72

5.2 Dynamic percolation in ionic microemulsions

5.2.1 Dipole correlation function for the percolation process

A description of the percolation phenomenon in ionic microemulsions in terms of the macroscopic DCF will be carried out based on the static lattice site percolation (SLSP) model [152]. In this model the statistical ensemble of various size clusters is described by the distribution function

$$w(s, s_m) = C_w \cdot s^{-\Omega} \exp\left(-\frac{s}{s_m}\right). \tag{5.20}$$

Here C_w is the normalization constant, Ω is a scaling exponent of the probability density "per lattice site" that the site, chosen randomly, belongs to the *s*-cluster (a cluster that consist of *s* lattice sites). The value of s_m is the cut-off cluster size that corresponds to the maximal cluster size. We note that the exponent Ω is related to the exponent τ of the commonly used cluster size distribution by the relationship $\Omega = 1 - \tau$ [152,213,220]. Note that clusters having sizes in the interval of $1 < s < s_m$ are referred to as mesoscopic clusters. The scaling properties of the mesoscopic dipole correlation functions related to the *s*-cluster of the geometrical substrate can be utilized for establishing a link between the static lattice geometrical percolation model and the relaxation functions.

We assumed that the mesoscopic relaxation function has a simple exponential form:

$$g[\bar{z}, \bar{z}_s(s)] = \exp[-\bar{z}/\bar{z}_s(s)]. \tag{5.21}$$

Here the dimensionless time $\bar{z} = t/t_1$ is normalized by the characteristic relaxation time t_1, the time required for a charge carrier to move the distance equal to the size of one droplet, which is associated with the size of the one cell in the lattice of the static site–percolation model. Similarly, we introduce the dimensionless time $\bar{z}_s = t_s/t_1$ where t_s is the effective correlation time of the *s*-cluster, and the dimensionless time $\bar{z}_m = t_m/t_1$. The maximal correlation time t_m is the effective correlation time corresponding to the maximal cluster s_m. In terms of the random walker problem, it is the time required for a charge carrier to visit all the droplets of a maximal cluster s_m. Thus, the macroscopic *DCF* may be obtained by the averaging procedure

$$\Psi\left[\bar{z},\bar{z}_m(s_m)\right]=\int_1^{\infty} g\left[\bar{z},\bar{z}_s(s)\right]\; w(s,s_m)ds \qquad (5.22)$$

.

In the framework of the SLSP model the relationship between the fractal dimension D_s of the maximal percolating cluster, the value of its size s_m and the linear lattice size L is determined by the asymptotic scaling law [152,213,220].

$$\frac{L}{l}=c_1 s_m^{1/D}, \quad (s_m\to\infty\ , D>0), \qquad (5.23)$$

where l is the linear size of the lattice cell and c_1 is a coefficient of proportionality.

Let us assume that on the temporal scale at percolation there is a scaling relationship between the characteristic relaxation time $\bar{z}_m=t_m/t_1$ and the value of its size s_m (similar to space scaling relationship (5.23), i.e.

$$\bar{z}_m=c_2 s_m^{\alpha}, \quad \left(s_m\to\infty,\ \alpha>0\right), \qquad (5.24)$$

where c_2 is a constant. Additionally, we assume that the self-similarity on the temporal scales is maintained also for clusters of size $s<s_m$, i.e.

$$\bar{z}_s(s)=c_2 s^{\alpha}\ , \qquad (s<s_m) \qquad (5.25)$$

Taking into account relationships (5.24) and (5.25), over the long time interval $\bar{z}>>1$ the integration of (5.22) may be performed asymptotically by the saddle-point method [135]. The main term of the asymptotic expansion can be obtained as the product of the power and stretched exponential universal relaxation laws [38]:

$$\Psi(\bar{z})\cong C\bar{z}^{\frac{1-2\Omega}{2(1+\alpha)}}\exp\left[-Q\cdot\left(\frac{\bar{z}}{c_2}\right)^{\frac{1}{1+\alpha}}\right]=A\bar{z}^{-\mu}\exp\left[-\left(\frac{\bar{z}}{\bar{z}_m}\right)^{\nu}\right], \qquad (5.26)$$

where $C=C_w K$, $K=\sqrt{\frac{2\pi}{\alpha(1+\alpha)}}(\alpha s_m)^{\frac{\alpha+2(1-\Omega)}{2(1+\alpha)}}$, and

$$\mu=(2\Omega-1)/2(1+\alpha)\ , \quad \nu=1/(1+\alpha), \quad Q=(\alpha\cdot s_m)^{-\frac{\alpha}{1+\alpha}}(1+\alpha). \qquad (5.27)$$

Thus, theoretically obtained asymptotic behavior (5.26) concurs with the phenomenological power-stretched exponential law (5.25). Using (5.27), it is possible to ascertain the relationship between the structural parameters α, Ω, s_m and the set of fitting phenomenological parameters ν, μ, $\bar{z}_m$ as follows:

$$\alpha = \frac{1}{\nu} - 1, \quad \Omega = \frac{\mu}{\nu} + \frac{1}{2}, \quad s_m = \frac{1}{\alpha}\left(\frac{\bar{z}_m}{c_2}\right)^{\frac{1}{\alpha}} \cdot (1+\alpha)^{\frac{1+\alpha}{\alpha}} \tag{5.28}$$

.

The set of structural parameters obtained by fitting and by using relationship (5.28) allows us to reconstruct the cluster size distribution function $w(s,s_m)$ and to treat the dynamic percolation in ionic microemulsions in terms of the classical static percolation model.

5.2.2 Dynamic hyperscaling relationship

The values of the exponents Ω, D and α in the distribution function (5.20) and scaling laws (5.23)-(5.25) depend on the Euclidean dimension d of the system and satisfy hyperscaling relationships (HSR). The HSRs may be different in the different models describing the various systems [221-225].

For instance, in the case of the SLSP model, a HSR may be obtained by taking into account both the self-similarity of the percolating cluster and the scale invariance of the cluster size distribution function (5.20). By utilizing the renormalization procedure [213], in which the size L of the lattice changes to a new size L_c with a scaling coefficient $b = L_c / L$, the relationship between the distribution function of the original lattice and the lattice with the adjusted size can be presented as $w(s, s_m) = b^{d-\Omega D} w(\tilde{s}, \tilde{s}_m)$, where $s = \tilde{s}^{-D}$ and $s_m = \tilde{s}_m^{-D}$.

The scale invariance condition $b^{d-\Omega D} = 1$, leads to the following static HSR

$$\Omega = \frac{d}{D} \tag{5.29}$$

which is also valid for a hyperlattice with $d>3$.

For the dynamic case, the percolation problem can be considered in hyperspace, where a temporal coordinate is introduced complementary to the Euclidean spatial coordinates. Using this approach we shall obtain the scaling relationships in the case of dynamic percolation and derive the dynamic HSR.

Let us consider a 2D square lattice *OABC* (see Figure 32), where in microemulsion droplets occupy a number of sites. A selected separate charge carrier hosted by the droplet starts its motion from a position on the side *OA* at t=0, and under the combined diffusion-hopping transport mechanism moves within the lattice *OABC*. It is understood that owing to this transport mechanism the trajectory of the individual carrier on the lattice *OABC* may be very intricate, and can even include loops. An example of such trajectories on the lattice *OABC* is shown in Figure 33.

One way to determine the characteristics of these trajectories is by solving a transport equation with different probabilities of hopping of the charge carrier and the corresponding parameters of the diffusion of the host droplet. Another way, which we shall use here, is based on a visualization of the equivalent static cluster structure. This approach allows us to interpret the dynamic percolation process in terms of the static percolation.

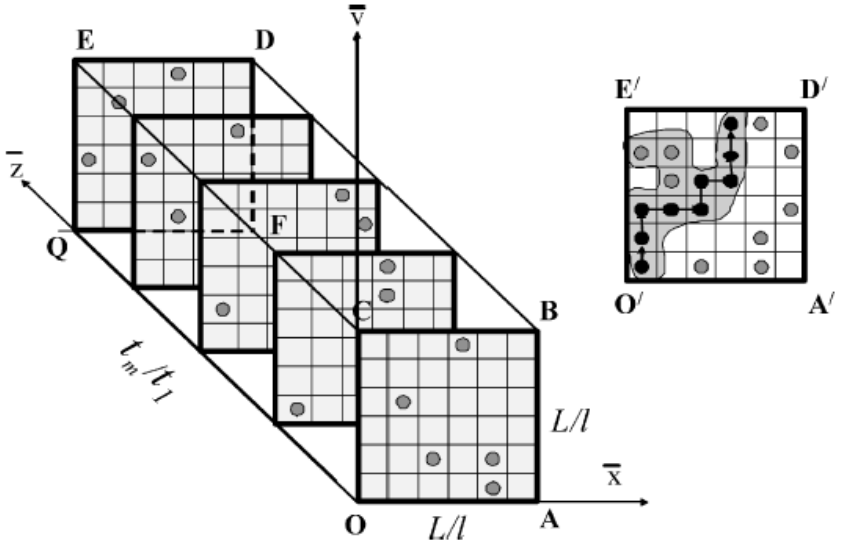

Figure 32. The visualization of dynamic percolation. A set of the realization of the occupied sites in the two-dimensional lattice over time with fixed time increments.

In the static percolation model the trajectory of the charge carrier is passes through a real and visual percolation cluster. While the real cluster in the dynamic percolation is invisible, the charge carrier trajectory can be drawn. In order to visualize the real cluster in the case of dynamic percolation let us assume that the site of trajectory intersections belongs to the equivalent static percolation cluster (ESPC). One must bear in mind that each site in the ESPC may be occupied several times. However, in the static percolation model each site may be occupied only once. In order to exclude the multi-occupation effect we must increase the dimension of the lattice.

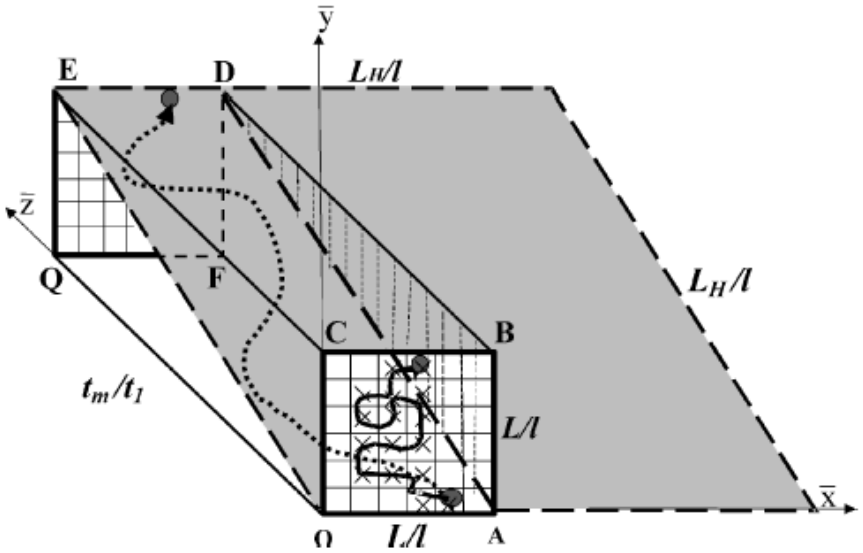

Figure 33. The charge carrier trajectories in the hyperlattice and the new scale L_H/l of the equivalent lattice formation.

A three-dimensional hyperlattice in the hyperspace formed by the spatial and temporal coordinates corresponds to the two-dimensional square lattice of size L, complemented by the time axis (see Figure 33). We use non-dimensional spatial coordinates ($\bar{x} = x/l$ and $\bar{y} = y/l$), which are normalized by the droplet size l. In turn, the non-dimensional temporal coordinate ($\bar{z} = t/t_1$) is normalized by the characteristic time t_1, which is the time needed for a charge carrier to move the distance equal to the size of one droplet. Thus the linear non-dimensional size of the hyperlattice along the two spatial axes is L/l, and the non-dimensional size of the hyperlattice along the temporal axis is $\bar{z}_m = t_m/t_1$. The characteristic time t_m corresponds to the time needed for a charge carrier to visit all the droplets in the maximal cluster s_m [150].

Note that the classic SLSP model for a square lattice *ABCO* would provide a percolation trajectory connecting opposite sites *OA* and *CB* (see Figure 32). On the other hand, for visualization of dynamic percolation we shall consider an effective three-dimensional static representation of a percolation trajectory connecting ribs *OA* and *ED* spaced distance L_H (see Figure 33). Such a consideration allows us to return to the lattice *OEDA*, with the initial dimension d=2, which is non-square and characterized by the two dimensionless sizes L_H/l and L/l. The new lattice size of the system can be determined from the rectangular triangle *OEQ* by

$$L_H / l = \sqrt{(L/l)^2 + (t_m / t_1)^2}\ , \tag{5.30}$$

where $L_H > L$. A projection of the three dimensional trajectory on the non-square plane lattice *OADE* is shown in Figure 33 by the dotted line. According to the conventional static site percolation model which always deals with square, cubic, and multidimensional one-scale lattices, the maximal scale L_H/l needs to be chosen in our case as the new scale of a square lattice (see Figure 33). A transformation from the initial lattice with scale size L/l to the lattice with the new scale size L_H/l may be performed by a renormalization procedure. By the substitution of scaling relationships (5.23) and (5.24) into (5.30) the expansion coefficient b_H for dynamic percolation can be presented as

$$b_H = \frac{L_H}{L} = \sqrt{1 + \left(\frac{c_2}{c_1}\right)^2 \cdot s_m^{2\alpha\left(1 - \frac{1}{\alpha D}\right)}}\ . \tag{5.31}$$

In the case of dynamic percolation the renormalization condition $b_H^{d-\Omega D} = 1$ may be fulfilled under the conventional condition $d - \Omega D = 0$ and under an additional requirement b_H=const, because $s_m \to \infty$. This is equivalent to the condition $s_m^{2\alpha\left(1-\frac{1}{\alpha D}\right)} = const$ and leads to the relationship $1 - \alpha D = 0$.

Thus, the dynamic HSR is expressed in the form of a system of two equations:

$$d - \Omega \cdot D = 0\ , \tag{5.32}$$

$$1 - \alpha \cdot D = 0\ . \tag{5.33}$$

A peculiarity of the dynamic case is the additional equation (5.33) which must be combined with the static HSR (5.32). After simple transformation, the solution of the system can be presented in the following way:

$$\Omega = d \cdot \alpha\ . \tag{5.34}$$

One must bear in mind that the parameter α describes the scaling law (5.24) for the temporal variable and is equal to the inverse dynamic fractal dimension $\alpha = 1/D_d$. Thus, the dynamic HSR (5.34) can be rewritten as

$$\Omega = \frac{d}{D_d} \tag{5.35}$$

and formally coincides with the HSR (5.29) for the static site percolation model.

Note that the dynamic fractal dimension obtained on the basis of the temporal scaling law should not necessarily have a value equal to that of the static percolation. We shall show here that in order to establish a relationship between the static and dynamic fractal dimensions we must go beyond relationships (5.32) and (5.33) for the scaling exponents.

5.2.3 Relationship between the static and dynamic fractal dimensions

Let us consider the hyperlattice anisotropy coefficient Θ_H as the ratio of the hyperlattice temporal to the spatial scale

$$\Theta_H = \frac{(t_m / t_1)}{(L / l)} . \tag{5.36}$$

Taking into account (5.30) and the scaling laws (5.23), (5.24), it is easy to show that when $s_m \to \infty$ the validity of the renormalization procedure is similar to the condition that the extension coefficient b_H must be a constant,

$$\Theta_H = \Theta \cdot s_m^{\alpha\left(1-\frac{1}{\alpha \cdot D}\right)} = const , \tag{5.37}$$

where $\Theta = c_2 / c_1$. In the case of dynamic percolation an additional equation (5.33) leads to the relationship $\Theta_H = \Theta = const$. In general, $\Theta \neq 1$ and the hyperlattice is non-cubic as far as the value of the coefficient Θ depends on the type of dynamics in the complex system.

The validity of (5.37) can be easily proven by an assumption of the existence of the parameter Θ dependency on the fractal dimension D. The derivation of both parts of (5.37) with respect to a variable D leads to the differential equation

$$\frac{d\Theta}{\Theta} = -\ln s_m \frac{dD}{D^2} . \tag{5.38}$$

In order to establish the relationship between the static and dynamic fractal dimensions, the initial conditions of the classical static percolation model must be considered for the solution

of differential equation (5.38) which can be written as $\Theta=\Theta_s=1$ for $D=D_s$. Here the notation "*s*" corresponds to the static percolation model and the condition $\Theta_s=1$ is fulfilled for an isotropic cubic "hyperlattice". The solution of (5.38) with the above-mentioned initial conditions may be written as

$$\ln\Theta = \ln s_m \left(1/D - 1/D_s\right) . \tag{5.39}$$

Taking into account that for dynamic percolation $D=1/\alpha=D_d$ we can easily obtain the relationship between the dynamic and static fractal dimensions, to wit,

$$D_s = \frac{D_d}{1 - D_d \dfrac{\log\Theta}{\log s_m}} . \tag{5.40}$$

Note that as is usual for scaling laws, the fractal dimensions $D_d=1/\alpha$ and D_s do not depend individually on the coefficients c_1 and c_2 entered in the scaling relationships (5.23), (5.24), respectively. However, as follows from (5.40) the relation between D_d and D_s depend on the ratio $\Theta=c_2/c_1$.

In the case of the real experimental set-up, $L=2\cdot10^3$ [86], and $l=5\cdot10^{-9}$ [143], the non-dimensional lattice size is equal to $L/l=4\cdot10^5$.

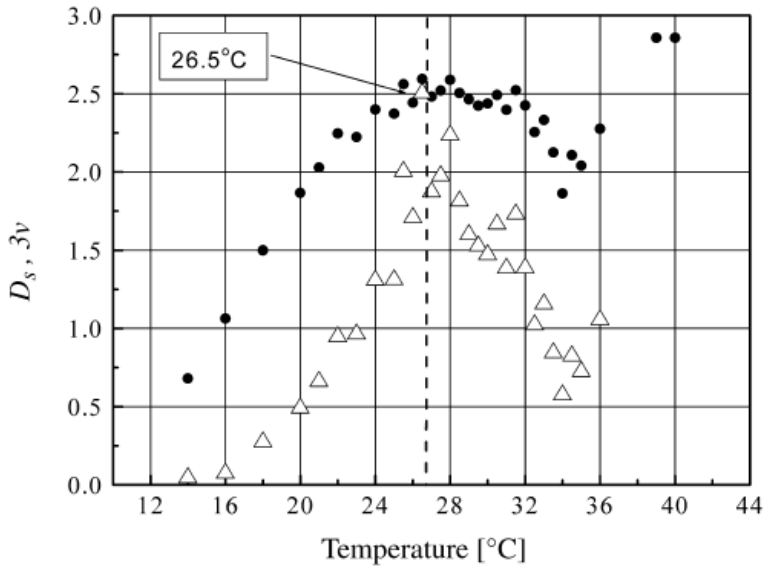

Figure 34. The temperature dependence of the static D_s (Δ) fractal dimensions and the product 3ν (●). At the percolation threshold temperature (T_p=26.5°C) $D_s= 3\nu$. (Reproduced with permission from Ref. 2. Copyright 2002, Elsevier Science B.V.)

Figure 34 shows the temperature dependencies of the static fractal dimensions of the maximal cluster. Note that at percolation temperature the value of the static fractal dimension D_s is extremely close to the classical value 2.53 for a three-dimensional lattice in the static site percolation model [152]. Moreover, the temperature dependence of the stretch parameter ν (see Figure 34) confirms the validity of our previous result (See (5.11)) $D_S = 3\nu$ obtained for the regular fractal model of the percolation cluster [47].

Thus, the non-Debye dielectric behavior in silica glasses, *PS* and *AOT* microemulsions, has similar properties. These systems exhibit an intermediate temperature percolation process that is associated with the transfer of the electric excitations through the random structures of fractal paths. It was shown that at the mesoscale range the fractal dimension of the complex material morphology (D_r for porous glasses and D_s for microemulsions) coincides with the fractal dimension D_p of the path structure. This value can be evaluated by the fitting of the experimental *DCF* to the stretched-exponential relaxation law (2.23).

5.3 Percolation as part of "Strange Kinetic" Phenomena

As shown above, the dielectric percolation phenomena in different systems such as ionic microemulsions, porous silicon, and porous glasses can actually be analyzed in the framework of one universal approach based on the idea of electric excitation transport through the fractal network clusters due to charge carriers' motion. This model describes the growth of the fractal pre-percolation clusters. Nevertheless, the model is applicable only to one particular phenomenon and does not address any basic theories of "strange kinetic" behavior [2]. Obviously, "strange kinetics" is a very wide class of phenomena, which cannot be covered by the limited number of existing models, and has several distinctive features. Most famous among these characteristics is the power-law (or stretched exponent) asymptotic with a fractional exponent for the dipole correlation function in time domain (see (2.23)-(2.25)). Another property of the percolation as part of a "strange kinetic" is that this class of phenomena is inherent to many-particle cooperative systems. Such complex matter cannot be considered as a simple sum of elementary units but rather should be regarded as a whole system due to the interactions between the elementary components. In a wide sense the word "interaction" represents not only the interaction with some kind of physical far-ranging field (say an electromagnetic field) but can also mean a geometrical (or even a quantum) constraint, or other type of coupling.

Since percolation is a property of macroscopic many-particle systems it can be analyzed in terms of statistical mechanics. The basic idea of statistical mechanics is the relaxation of the perturbed system to the equilibrium state. In general the distribution function $\rho(\boldsymbol{p},\boldsymbol{q}; t)$ of a statistical ensemble depends on the generalized coordinates $\boldsymbol{q}$, momentum $\boldsymbol{p}$ and time t. However, in the equilibrium state it does not depend explicitly on time [226-230] and obeys the equation

$$\frac{\partial}{\partial t}\rho(\boldsymbol{p},\boldsymbol{q}; t) = 0 \ . \tag{5.41}$$

The evolution of the distribution function to the equilibrium state is governed by the so-called Liouville equation (evolution equation)

$$\frac{\partial \boldsymbol{\rho}(\boldsymbol{p},\boldsymbol{q},\boldsymbol{t})}{\partial \boldsymbol{t}} = -i\mathcal{L}\ \rho(\mathbf{p},\mathbf{q},t) \ , \tag{5.42}$$

where $\mathcal{L}$ is the Liouville operator. Thus, by virtue of (5.42) the evolution operator $\mathcal{L}$ determines the dynamical properties of the statistical system. The specific form of this operator is dependent on the Hamiltonian function H [226-230] as

$$\mathcal{L}g = -i\{H, g\} \ , \tag{5.43}$$

where $\{H, g\}$ are the Poisson brackets. In the classical statistical mechanics

$$\{H, g\} = \sum_k \left(\frac{\partial H}{\partial q_k}\frac{\partial g}{\partial p_k} - \frac{\partial H}{\partial p_k}\frac{\partial g}{\partial q_k} \right) . \tag{5.44}$$

In quantum mechanics the functions H, g become operators $\hat{H}$ and $\hat{g}$, and $\{\hat{H}, \hat{g}\}$ obtains the commutator form $\{\hat{H}, \hat{g}\} = \frac{2\pi}{ih}\left(\hat{H}\ \hat{g} - \hat{g}\ \hat{H}\right)$, where h is the Plank constant.

Therefore, the consistent study of many-particle system dynamics should start by establishing the H and then solving the evolution equation (5.42). Unfortunately, examples of such calculations are very rare and are only valid for limited classes of model systems (such as the Ising model) since these are quite extended calculations. In particular, to the best of our knowledge, the relaxation patterns (2.23)-(2.25) are as yet not being derived this way. In this section, we consider the problem from a different side. We will assume that (2.23)-(2.25) are

given and try to guess what statistical properties leads to the "strange kinetic" behavior. Let us first examine the equilibrium state (5.41), whose formal solution gives

$$\rho(\boldsymbol{p},\boldsymbol{q};t) = const \quad . \tag{5.45}$$

Recently the new concept of fractional time evolution was introduced [45]. In addition to the usual equilibrium state (5.45), this concept leads to the possibility of the existence of an equilibrium state with power-law long time behavior. In this case the infinitesimal generator of time evolution is proportional to the Riemann-Liouville fractional differential operator ${}_0D_t^{\nu}$. By definition of the Riemann-Liouville fractional differentiation operator [231,232]

$${}_0D_t^{\nu}\left[h(t)\right] = \frac{d}{dt}\,{}_0D_t^{\nu-1}\left[h(t)\right] \quad , \quad 0 < \nu \le 1 \tag{5.46}$$

,

where

$${}_0D_t^{-\nu}\left[g(t)\right] = \frac{1}{\Gamma(\nu)}\int_0^t (t-t')^{\nu-1} g(t')dt', \quad 0 < \nu \le 1 \tag{5.47}$$

is the Riemann-Liouville fractional integration operator and $\Gamma(\nu) = \int_0^{\infty} y^{\nu-1}\exp(-y)dy$ is the Gamma-function. Obviously, the derivation of order υ should be dependent on the properties of the cooperative system; although there is no clear understanding for the time being how υ depends on these properties.

Nevertheless, let us call the "fractional equilibrium state" the state of the statistical system that under the condition of time independence obeys the following:

$${}_0D_t^{\upsilon}\rho(\boldsymbol{p},\boldsymbol{q};t) = 0 \quad . \tag{5.48}$$

We will discuss this state in relation to the recent approaches of the anomalous diffusion theory [31]. It is well known [226-230] that by virtue of the divergent form of Poisson brackets (5.44) the evolution of the distribution function $\rho(\boldsymbol{p},\boldsymbol{q};t)$ can be regarded as the flow of a fluid in the phase space. In this interpretation the Liouville equation (5.42) becomes analogous to the continuity equation for a fluid

$$\frac{\partial \rho}{\partial t} + \mathrm{div}(\rho \boldsymbol{v}) = 0 \quad , \tag{5.49}$$

where distribution function ρ is interpreted as the density of a fluid and $\boldsymbol{v}$ is its local velocity. Let us extend this analogy. The continuity equation accompanied by the relationship between the gradient of the fluid density and its flux (Darcy's law for the liquid flow or Fourier's law for heat flow for instance) [233,234]

$$\mathrm{grad}(\rho) = -\vartheta \rho \boldsymbol{v} \tag{5.50}$$

gives

$$\frac{\partial \rho}{\partial t} = \vartheta \Delta \rho \quad , \tag{5.51}$$

where ϑ is the appropriate constant that characterizes permeability of the space and Δ is the Laplace differential operator. From a mathematical point of view (5.51) is analogous to the diffusion equation where ρ is regarded as the density of diffusing particles and ϑ is proportional to the appropriate diffusion coefficient.

It is well known that the diffusion equation can be obtained in two ways. The first is based on the equation of continuity and the relationship between the fluid density gradient of its flux (5.49-5.51). The second way is the probabilistic approach developed from the theory of Brownian motion [31,226,227,235]. This approach does not appeal to the local differential equations like (5.49) and (5.50), but considers the probability of jumps between the sites of some lattice. There is an extension of this approach for the case when the lengths of the jumps as well as the waiting times between jumps are random. This is the so-called continuous time random walk (*CTRW*) scheme [31,236-238]. By applying different probability distribution functions for waiting time and jump length one can obtain different types of diffusion patterns [31]. In particular, if the characteristic waiting time diverges because of a long-tailed waiting time probability distribution function (proportional to $t^{-(1+\upsilon)}$), but the jump length variance is still kept finite, then diffusion (5.51) obtains a fractional derivation [31] instead of the first derivation in time on its left hand side.

$$ {}_0D_t^{\upsilon} \rho = \vartheta_{\upsilon} \Delta \rho \quad . \tag{5.52}$$

Here the parameter ϑ_{υ} has a physical meaning similar to ϑ in (5.51), but with different a physical dimension. In the general case a term proportional to $\rho(t=0)$ should be added to the

right hand side of (5.52) but by choosing the appropriate initial conditions it can be subtracted. Thus, we will not discuss this term.

Let us reiterate that diffusion defined by (5.51) can be derived using the Brownian motion approach and a continuity equation. Moreover, one can imply that (5.52), a generalization of (5.51), can be derived not only in the framework of the *CTRW* scheme but also by using some analogy of the continuity equation as well. The difference between (5.51) and (5.52) is only in time derivation. Thus, the analogy of continuity (5.49) that corresponds to the anomalous diffusion (5.52) is

$$ {}_0D_t^{\upsilon}\rho + \mathrm{div}(\rho\, \boldsymbol{v}_{\upsilon}) = 0 . \tag{5.53}$$

Let us call it the "anomalous continuity equation". There are two main features that distinguish this equation from (5.49). The first is that (5.53) becomes non-local in time by virtue of the convolution form of the fractional derivation operator ${}_0D_t^{\upsilon}$. Second, in spite of the different physical dimension [m·s$^{-\upsilon}$], the quantity $\boldsymbol{v}_{\upsilon}$ has a physical meaning similar to the local velocity $\boldsymbol{v}$.

Let us return back to the Liouville equation that can be regarded as a continuity equation. There is a possibility to establish an evolution equation not only in the usual form (5.42) but also based on the anomalous continuity (5.53)

$$ {}_0D_t^{\upsilon}\rho(\boldsymbol{p},\boldsymbol{q};t) = -iL\rho(\boldsymbol{p},\boldsymbol{q};t) . \tag{5.54}$$

This equation implies an equilibrium state in the form (5.48).

Thus, the fractional equilibrium state (5.48) can be considered a consequence of the anomalous transport of phase points in the phase space that results in the anomalous continuity (5.53). Note that the usual form of evolution (5.42) is a direct consequence of the canonical Hamiltonian form of microscopic motion equations. Thus, the evolution of (5.54) implies that the microscopic equations of motion are not canonical. The actual form of these equations has not yet been investigated. However, there is great suspicion that in this case dissipative effects on the microscopic level become important.

If we assume factorization of time dependency in the distribution function then the formal solution of (5.48) is

$$\rho_f(\boldsymbol{p},\boldsymbol{q};t)=\rho_f(\boldsymbol{p},\boldsymbol{q};\tau_f)\left(\frac{t}{\tau_f}\right)^{\upsilon-1}, \tag{5.55}$$

where $t \geq \tau_f$, $\rho_f(\boldsymbol{p},\boldsymbol{q};\tau_f)$ and τ_f depend on the initial conditions. Obviously, the assumption about factorization of time dependency for the distribution function is not universal. However, this type of factorization is justified when the equilibrium and non-equilibrium (in the ordinary sense) parts of distribution function $\rho(\boldsymbol{p},\boldsymbol{q};t)$ are orthogonal to each other in the phase space [230].

The interpretation of any distribution function as a probability density function in the phase space leads to the requirement

$$\iint \rho(\boldsymbol{p},\boldsymbol{q};t)\frac{d\boldsymbol{p}d\boldsymbol{q}}{N!h^{3N}}=1, \tag{5.56}$$

where $3N$ is the number of degrees of freedom. This normalization is based on the uncertainty relation that establishes the minimal phase cell as $dp_k\, dq_k \geq h$. Substitution of the solution (5.55) in (5.56) gives

$$\iint \rho_f(\boldsymbol{p},\boldsymbol{q};t)\,d\boldsymbol{p}d\boldsymbol{q}=\frac{\Xi}{N!h^{3N}}\left(\frac{t}{\tau_f}\right)^{\upsilon-1}=1, \tag{5.57}$$

where $\Xi=\iint \rho_f(\boldsymbol{p},\boldsymbol{q};\tau_f)d\boldsymbol{p}d\boldsymbol{q}$ is a constant. Thus from (5.57) one can get

$$\frac{N!h^{3N}}{\Xi}=\left(\frac{t}{\tau_f}\right)^{\upsilon-1} \tag{5.58}$$

which for $\upsilon < 1$ indicates a decrease in the number of degrees of freedom.

From one point of view, (5.58) can be interpreted as a manifestation of the non-canonical nature of the microscopic motion equation and supports the idea of an impact of dissipative effects on the microscopic level (for time scale $t < \tau_f$). From another point of view (5.58) can be related to the "coarse graining" of the phase volume minimal cells. The concept of fractional evolution is the result of consequent acting of the averaging operator [45]. Each application of the averaging operator is equal to the loss of information regarding the short time mobility and is closely associated with the renormalization approach ideas [239].

A simple example of this "coarse graining" is that of two masses in the viscous media connected by a spring. The spring here represents an interaction between the microscopic

particles while viscosity reflects the dissipative effects. Now let us discuss the situation when one mass is exposed by some mechanical perturbation with a wide spectrum (say the δ-impulse of force). In the beginning the motions of the masses are almost independent of each other. The viscosity effect then leads to a decay of the high frequency modes of mobility and the motions of masses become more and more correlated. At the initial times, one should observe the motion of two centers of gravity while at the longer time interval it is enough to know the position of the joint center of gravity. Thus, the "coarse graining" effect leads to a reduction in the number of degrees of freedom [240].

The reduction of degrees of freedom can also be regarded as the transition from the non-correlated state to the state with long-range space correlations, and can be accompanied by phase transition. This is the reason the renormalization approach was used initially to describe phase transition phenomena [226,228,239]. The theory of the phase transitions investigates the dependency of macroscopic physical quantities (like sample magnetization or polarization vectors) on the external parameter (like external fields or temperature) values. The changes of the degrees of freedom are the result of competition between external perturbations (say temperature) and internal interactions.

In contrast to phase transitions in the fractional equilibrium state (5.46) the statistical system loses degrees of freedom during evolution in time. The degrees of freedom, independent at the short time limit, become dependent later due to the interactions (in the wide sense coupling, constraint etc.) and dissipative effects. The distribution function for the fractional equilibrium state (5.55) can be utilized to calculate the macroscopic dipole correlation function (2.22). The statistical averaging designated <....> in (2.22) is performed over the equilibrium ensemble (in the usual sense) with a distribution function that does not depend explicitly on time. If we regard the evolution of the *DCF* as a fractional equilibrium state (5.46), then by using properties of statistical averaging and the Liouville operator [229,230] we can transfer time dependence of the dynamic variable $\boldsymbol{M}(t)$ to time dependence of the distribution function $\rho_f(\boldsymbol{p},\boldsymbol{q};t)$. Thus, instead of $<\boldsymbol{M}(0)\boldsymbol{M}(t)>$ in (2.22) we use $<\boldsymbol{M}(0)\boldsymbol{M}(0)>_f$, where subscript f means that statistical averaging was performed with distribution function (5.55). In this case one will get

$$\phi(t) \cong \frac{<\boldsymbol{M}(0)\boldsymbol{M}(t)>}{<\boldsymbol{M}(0)\boldsymbol{M}(0)>} = \frac{<\boldsymbol{M}(0)\boldsymbol{M}(0)>_f}{<\boldsymbol{M}(0)\boldsymbol{M}(0)>} =$$

$$= \frac{\iint \boldsymbol{M}(\boldsymbol{p},\boldsymbol{q};0)\boldsymbol{M}(\boldsymbol{p},\boldsymbol{q};0)\rho_f(\boldsymbol{p},\boldsymbol{q};t)\,d\boldsymbol{p}d\boldsymbol{q}}{\iint \boldsymbol{M}(\boldsymbol{p},\boldsymbol{q};0)\boldsymbol{M}(\boldsymbol{p},\boldsymbol{q};0)\rho(\boldsymbol{p},\boldsymbol{q};0)\,d\boldsymbol{p}d\boldsymbol{q}} \sim \left(\frac{t}{\tau_f}\right)^{\upsilon-1}, \quad t \geq \tau_f \ . \tag{5.59}$$

Thus, one can regard the power law dependence of relaxation function (2.24) as a result of the fractional equilibrium state (5.48).

In order to understand the stretched exponential behavior of *DCF* (2.23) let us discuss Gibb's phase exponent $\eta_G = -ln\,\rho(\boldsymbol{p},\boldsymbol{q};t)$. This quantity plays a special role in statistical mechanics and relates to the entropy of the system. If Gibb's exponent obeys fractional evolution equation

$$_0D_t^{\nu}\eta_G = 0, \tag{5.60}$$

then the distribution function is

$$\rho_\eta(\boldsymbol{p},\boldsymbol{q};t) = \rho_\eta(\boldsymbol{p},\boldsymbol{q};0)\exp\left(-\left(\frac{t}{\tau_\eta}\right)^{\nu-1}\right), \tag{5.61}$$

where $\rho_\eta(\boldsymbol{p},\boldsymbol{q};0)$ and τ_η depend on the initial conditions. A calculation analogous to (5.59) shows that this distribution function leads to the *KWW* dependency of the *DCF*. Thus, in the framework of the fractional time evolution concept the power-law time dependence of the relaxation function behavior (2.24) and the stretched exponential relaxation (2.23) can be regarded as two different realizations: the fractal equilibrium state of the distribution function and the fractal evolution of Gibb's phase exponent.

A similar ideology can also be the basis of the relaxation pattern (2.24) when these two different types of fractal evolution simultaneously coexist for two subspaces ($\boldsymbol{p}_f, \boldsymbol{q}_f$) and ($\boldsymbol{p}_\eta, \boldsymbol{q}_\eta$) of the total statistical system phase space ($\boldsymbol{p}, \boldsymbol{q}$). In this case the total distribution function $\rho_{f\eta}(\boldsymbol{p},\boldsymbol{q};t)$ is the product of two statistically independent distribution functions $\rho_f(\boldsymbol{p}_f, \boldsymbol{q}_f;t)$ and $\rho_\eta(\boldsymbol{p}_\eta, \boldsymbol{q}_\eta;t)$

$$\rho_{f\eta}(\boldsymbol{p},\boldsymbol{q};t) = \rho_\eta(\boldsymbol{p}_\eta,\boldsymbol{q}_\eta;0)\rho_f(\boldsymbol{p}_f,\boldsymbol{q}_f;\tau_f)\left(\frac{t}{\tau_f}\right)^{\upsilon-1}\exp\left(-\left(\frac{t}{\tau_\eta}\right)^{\nu-1}\right), \tag{5.62}$$

that can be related to the relaxation pattern (2.24).

The relaxation law (5.62) has been observed in the case of dynamic percolation in ionic micro-emulsions (see section 5.2). Below the percolation threshold, the relaxation process is provided by two types of mobility: mobility of the pre-percolation clusters and mobility of the charge carriers inside these clusters. The first type of mobility is governed by the power-law (2.23) while the second type exhibits stretched exponential behavior (2.22) [152]. Thus, there are two subspaces of degrees of freedom: the first is related to the mobility of pre-percolation clusters as a whole and the second reflects the mobility inside the clusters. Approaching the percolation threshold pre-percolation clusters grow and become an infinite (or very large for a real finite size system) percolation cluster at the threshold. At this point mobility of the cluster is impossible, as first subspaces of degrees of freedom disappear and the relaxation function obtains the stretched exponential pattern (2.22). Far from the percolation, one finds the opposite situation. The pre-percolation clusters are small, second subspace degrees of freedom are not yet developed and the relaxation function obeys the power-law (2.23).

In this section we made an attempt to interpret our main results in static and dynamic percolation in terms of statistical mechanics and to find the link to several other approaches and models that have describe different aspects of "strange kinetic" phenomena. Obviously, the arguments represented in this section are not rigorous. They are hints rather than the proofs. Nevertheless, our attempts to find a unified ideology can result in a deeper understanding of the statistical background of “strange kinetics” and to draw the following general picture.

As we have discussed above, the non-canonical nature of the motion on the microscopic level can be considered as the initial basis of “strange kinetics“. In general, this non-canonical motion of one elementary microscopic unit reflects the cooperativity due to the different kinds of interaction in the statistical many particles ensembles. Such interactions, which are specific for each complex system, lead to energy dissipation and can be reduced to the integral term associated with the memory effect in the different kinds of evolution equations. For any processes, which display scaling properties (such as percolation, or phase transition), the non-canonical motion can be described in terms of the fractional Liouville equation (5.54). According to the integral representation of the fractional derivation by (5.46) and (5.47) the scaling properties are contained in the kernel of the convolution integral. As was shown the fractional Liouville equation can be considered as the base equation for different approaches and models (percolation, anomalous diffusion, damping oscillations, renormalization approach, etc).

5.4 Universal scaling behavior in H-bonding networks

The properties of H-bonded liquids were already reviewed earlier in section 4.4. Here we would like to continue the consideration of these samples this time with regard to their universal scaling behavior. We have separated this discussion into two parts, which consider two different kinds of glycerol-water mixtures.

5.4.1 Glycerol-rich mixtures

The analyses of the master plots presented in Figure 27 in the glycerol rich region showed that the use of known phenomenological relations and their superposition for the simultaneous fitting of the *EW*, the main process and dc-conductivity provide satisfactory results only with a significant number of fitting parameters. Therefore, we propose a new phenomenological function with a lesser number of fitting parameters as follows:

$$\varepsilon^*(\omega) - \varepsilon_\infty = \frac{\Delta\varepsilon \cdot \left[1 + A(\omega\tau)^q\right]}{(1 + i\omega\tau)^\beta} + \frac{B\Delta\varepsilon}{i\varepsilon_0\omega\tau}, \tag{5.63}$$

where $\sigma = B\Delta\varepsilon/\tau$ is the dc-conductivity, B is a constant, β is a parameter describing asymmetrical relaxation peak broadening (similar to β_{CD}), and A and q are parameters to describe the *EW*, respectively [208]. For glycerol-water mixtures in the present temperature- and concentration-range:

$$q = 1 - \beta + \gamma, \tag{5.64}$$

where γ is equal to 0.08 for the entire range of the observed concentrations. The nature of this parameter is not clear yet. Figure 35 shows a good fitting of both real and imaginary parts of the raw dielectric spectra using relationship (5.63).

Moreover this fitting shows that in the considered temperature-frequency landscape only the temperature dependence of $\Delta\varepsilon = \Delta\varepsilon(T)$ and $\tau = \tau(T)$ are observed, while the other parameters *B*, *β*, *A*, and *q* are not temperature dependent. Thus, the proposed phenomenological model (5.63) as a modification of the CD function (2.21) with a conductivity term could be successfully applied for simultaneous fitting of dc-conductivity, the main process and the *EW* presented in the master plots (see Figure 27). At the same time, parameters *β*, *A* and *q* have a concentration dependence where *A* and *β* decrease with a decrease of glycerol content (Figure 36), while parameter *q* increases according to (5.64).

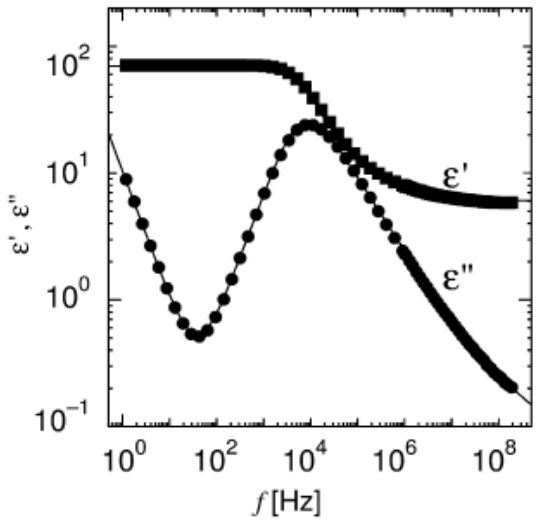

Figure 35. A typical fitting result by the function (114) for the dielectric spectrum (75 mol% at 224 K, both real and imaginary parts are shown) where parameters β and A were fixed to be the same values obtained in the master plot of 75 mol% of glycerol (see Fig. 27b) with τ = 25 μs and $\Delta\varepsilon$ = 64.1. (Reproduced with permission from Ref. 208. Copyright 2005, American Chemical Society.)

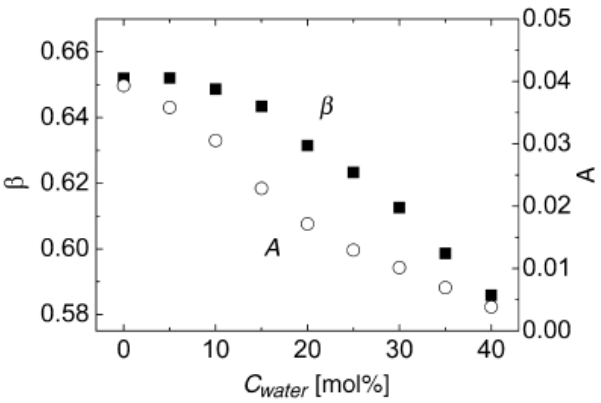

Figure 36. Water concentration dependence of the shape parameters (β, filled box; A, unfilled circle) in (114) obtained by curve fittings of the master plots. (Reproduced with permission from Ref. 208. Copyright 2005, American Chemical Society.)

Note, that the parameters A and q can be associated with some characteristic mesoscopic relaxation time τ_0 as follows:

$$A(\omega\tau)^q = (\omega\tau_0)^q \quad , \qquad \tau/\tau_0 = A^{-\frac{1}{q}} . \tag{5.65}$$

Since the parameters A and q of the master plot are not dependent on temperature, the ratio τ/τ_0 becomes independent of temperature as well, i.e. the scale τ_0 follows the same *VFT* law as the main relaxation time τ (Figure 37).

Temperature dependencies of τ_0 that were obtained by (5.63) and (5.64) and representation by the *VFT* model (full lines) where D and T_v have the same values as those for τ_{max} presented in Fig.26 as well as in the legend (100 to 60 mol%). The pre-exponential factor such as ln (τ_{v0}) is shown in the legend.

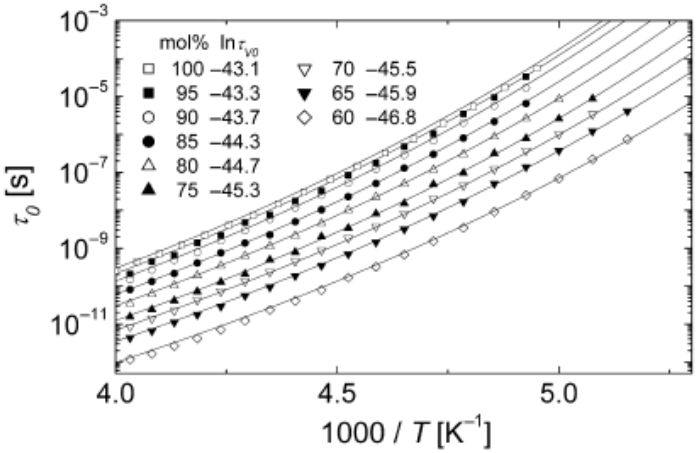

Figure 37. Temperature dependence of τ_0 obtained by (114) and (115) and representation by the VFT model (full lines) where D and T_v are the same values as those for τ_{max} presented in Fig. 26 as well as in the legend (100 to 60 mol%). The preexponential factor such as ln(τ_{v0}) is shown with the legend.

In this context, the value τ_0 should be associated with the minimal cooperative relaxation time that reflects the *EW* dynamics and keeps the same *VFT* temperature law as for the main relaxation time τ and τ_{max} (see Figure 26). At the same time, the ratio τ / τ_0 is strongly dependent on concentration (Figure 38). The increase of the ratio τ / τ_0 with the increase of water content indicates that the *EW* of glycerol is eroded by water molecules much faster than the main relaxation process. In order to clarify such a mechanism, let us assume that the *EW* is the result of some fast short-range cooperative dynamics which can be associated with the so-called "cage level" [183]. This means that for anhydrous glycerol at the mesoscopic scale we are considering only the glycerol-glycerol interaction. In the case of glycerol-water mixtures in the range of the master plot universality, the *EW* is caused mostly by two kinds of interactions: glycerol-glycerol and glycerol-water interactions. It is manifested by the decreasing of τ_0 due to fast mobility of water molecules contributing to the cooperative dynamics at the "cage level". However, the glycerol-glycerol molecular interactions remain the dominant relaxation mechanism at the scale of the whole H-bond network. A simplified picture of interaction for the 60 mol% of glycerol in water where the master plot universality is still observed could be presented as follows. It is well known [241] that in the liquid phase three OH groups of a glycerol molecule may be involved in approximately $n_g \cong 6$ hydrogen bonds with neighboring molecules, while a water molecule may establish $n_w = 4$ hydrogen bonds. The critical mole fraction where glycerol H-bonds are balanced with water H-bonds, may be roughly estimated as $x = 100\% \cdot n_w / (n_w + n_g) = 40$ mol%. However, water-water

interactions may still appear at higher concentrations of glycerol because of density fluctuations, as is suggested by the breakdown of the universality only at 55 mol%. Most probably the mechanism of the observed universality is related to the H-bond dynamic structures of the glycerol-water mixture. In this case the *EW* is a projection of a short-range fast dynamic of H-bond structures, the main relaxation process results from a larger scale of H-bond clusters and dc-conductivity relates to the transfer of charge carriers through the percolated H-bond network.

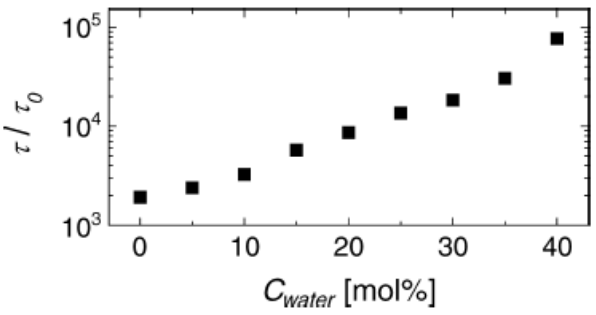

Figure 38. Water concentration dependence of the ratio of characteristic times (τ / τ_0) obtained by (16). (Reproduced with permission from Ref. 208. Copyright 2005, American Chemical Society.)

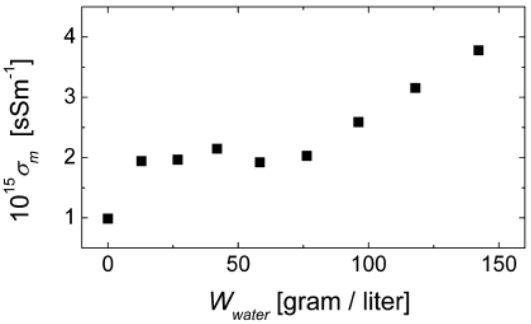

Figure 39. Water content dependence of the normalized conductivity on the master plots (117), where $\sigma_m \sim 1.6 \times 10^{-16}$ sSm^{-1}. Note that our data of densitymeasurements for glycerol–water mixtures at 288 K were used to obtain water content, W_{water}, [gram/liter] from the mole fractions. (Reproduced with permission from Ref. 208. Copyright 2005, American Chemical Society.)

Figure 39 shows water content dependence of normalized conductivity on the master-plots evaluated by

$$\sigma_m = \frac{2\pi\tau_{\max}}{\varepsilon''_{\max}}\sigma \quad . \tag{5.66}$$

The nature of charge carriers is not clear yet and there could be two possibilities: ionic impurities or H-bond network defects (so-called orientation and ionic defects) similar to those considered in the conduction and relaxation of ice [242,243]. Conductivity behavior due to ionic impurities is expected to increase linearly with the impurities concentration per unit volume, and the impurities would be proportional to water content. However, the normalized conductivity did not show such a linear behavior (Figure 39), although some tendency of increase with water content can be observed. This increase of the normalized conductivity

does not immediately contradict the concept of defect-conductivity, because the number of defects can also be increased by increasing water content. At the least, diffusion of ions should also be accompanied by breaking or changing of H-bond networks around the ion molecule. Such rearrangements of H-bond networks around ions can affect the *EW* and may influence the main relaxation process on a cluster level. Thus, the existence of universality is most likely based on the presence of an H-bond network and its defect structure.

Moreover, the experimental data through dc-conductivity, the main process and the *EW* could be described by the new phenomenological function (5.63). If concentration remains the same, only two variable parameters, $\Delta\varepsilon$ and τ, with a set of constants, can describe the whole temperature dependence of spectra. The universality in the master plots of dielectric spectra for glycerol and glycerol-water mixtures is related to the same origin of elementary molecular processes that is most probably a "defect" formation and its percolation in an H-bond network.

5.4.2 Water-rich mixtures

Such universal dielectric behavior disappeared at higher water concentrations (lower than 60 mol% of glycerol) due to the appearance of water-water interaction coexisting with the glycerol-glycerol and glycerol-water interactions in the glycerol domains. These water-water interactions were also observed recently by Sudo et al. [190]. Therefore, we can assume that H-bond networks in water rich mixtures are not homogeneous on a mesoscopic level, although the detailed features of such heterogeneous structures are not fully known. With increasing of amounts of water, the water pools grow in size, which lead to their freezing at low temperatures. In the case of H-bonding liquid mixtures, however, dynamical and structural properties in frozen states have not yet been extensively studied. The *BDS* and differential scanning calorimetry (*DSC*) measurements of glycerol-water mixtures in the high water concentration range and temperature intervals including the water-frozen state were reported recently [244].

Let us consider the dynamics of glycerol-water mixtures in terms of the characteristic time $\tau_{\max} = 1/(2\pi f_{\max})$ and temperature dependences of the main relaxation process. In the glycerol rich region (100-40 mol%), as mentioned in Section 4.4 and as shown in Figure 40, $\tau_{\max}$ is well described by the *VFT* law with the same value of fragility (D = 22.7) and almost the same values of pre-exponent factor ($\ln \tau_v$ = –35.9 to –36.4).

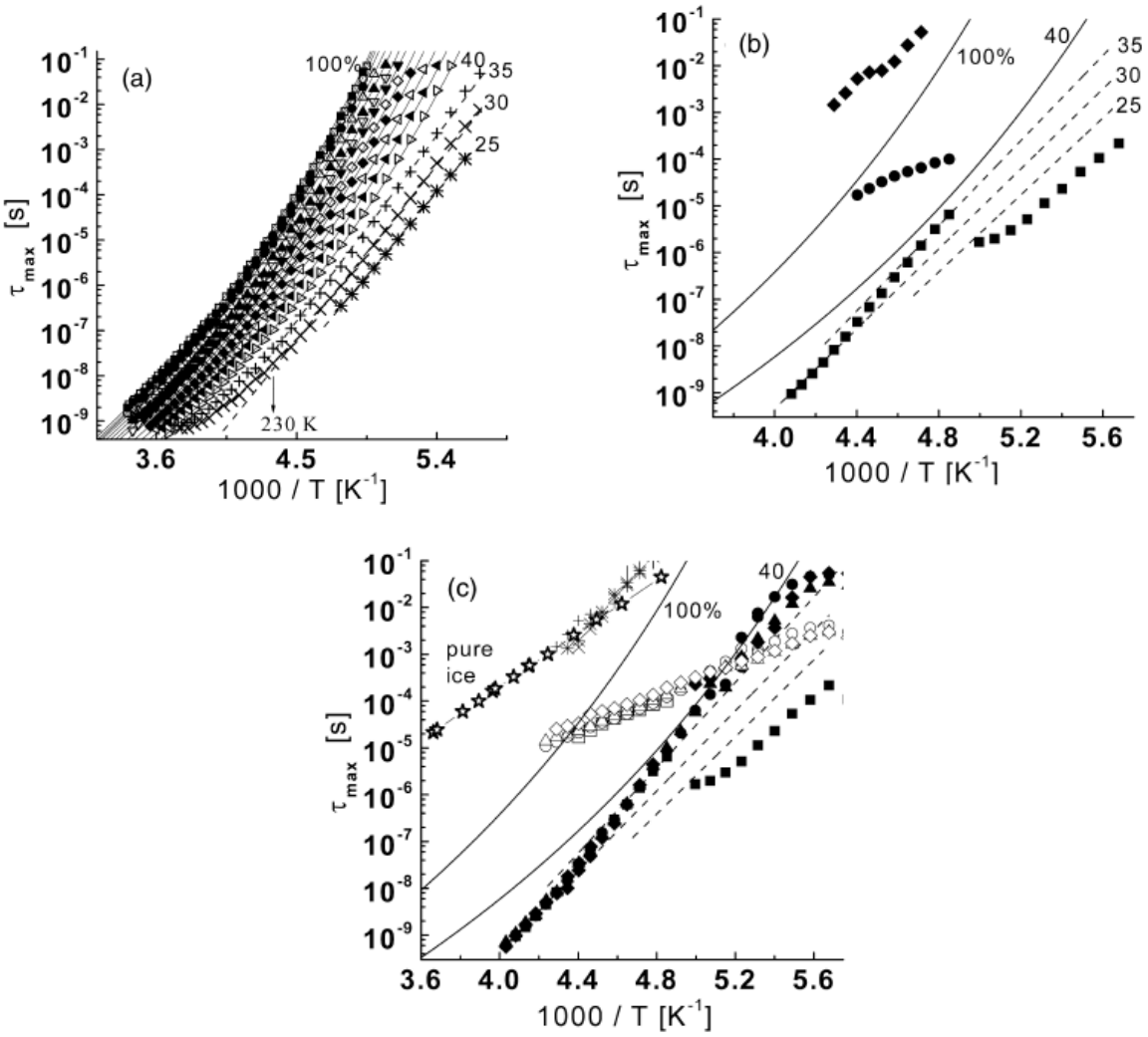

Figure 40. (a) Temperature dependence of τ_{max} for the main relaxation process of glycerol–water mixtures in 100 to 25 mol%. (b) Temperature dependence of τ_{max} for 20 mol% (filled box represents main relaxation process; filled diamond represents relaxation process due to ice; filled circle represents relaxation process due to interfacial water). The solid curves are the same as the curves shown in (a) for 100 and 40 mol% as well as the dashed lines for 35, 30, and 25 mol%. (c) Temperature dependence of τ_{max} for water-rich mixtures. The filled and unfilled symbols show the main relaxation process and the relaxation process due to interfacial water, respectively (box, 20 mol%; circle, 15 mol% triangle, 10 mol%; diamond, 5 mol%). Temperature dependence of τ_{max} for the relaxation process due to ice are also shown (plus, 20 mol%; cross, 15 mol% asterisk, 10 mol%; vertical bar, 5 mol%), and the unfilled stars show the experimental results for bulk ice [244]. (Reproduced with permission from Ref. 244. Copyright 2005, American Chemical Society.)

The plots in Figure 40a represent the experimental data, for glycerol-water mixtures, where the glycerol concentration is systematically changed with the steps of 5 mol%, and the solid lines show the fitting results according to the *VFT* law. The results indicate that the relaxation mechanisms and H-bond networks for the glycerol-rich mixtures are similar to those of pure glycerol. Below 40 mol% of glycerol and at lower temperatures (below

~230 K), the temperature dependence of the τ_{max} was continuously changed from *VFT* to Arrhenius shape, as shown in Figure 40a (dashed lines). Our analyses and comparison with the literature [190] shows that τ_{max} temperature behavior in the water-rich region can depend on the temperature history, although no differences were found in glycerol-rich regions above T_g (here T_g is the glass transition temperature). These results may indicate that mesoscopic structures of H-bond networks in glycerol-rich regions are quite homogeneous. In contrast, in water-rich regions, such mixtures have a more complicated dynamic behavior. Glycerol molecules cannot provide all water molecules with H-bond networks, and correspondingly the system forms so-called glycerol and water cooperative domains, respectively. Dynamic structures of such domains can depend on the temperature hysteresis. The critical molar fraction (x_g) would then relate to the number of H-bonds of glycerol and would be approximately 40 mol% as it was shown above (See Section 5.4.1).

The existence of this critical concentration of 40 mol% of glycerol is well supported by the results obtained from further study of the water-rich region. Figure 40b shows the temperature dependence of τ_{max} for 20 mol% of glycerol. At lower temperatures, τ_{max} demonstrates a behavior similar to that of higher glycerol concentrations. However, when the temperature was increased and approached T = 206 K, a crystallization of the extra water occurred and τ_{max} increased up to nearly the same vales as that of 35 mol% of glycerol. After the crystallization, two additional Arrhenius type relaxation processes were observed (Figure 41 shows the typical dielectric spectra of before- and after- the crystallization). One of these relaxation processes is due to the presence of ice cores, since the relaxation time and its activation energy (~ 77 kJ / mol) is similar to the well known values for bulk ice which were reported by Auty and Cole [245] (Figure 40c). Another relaxation process may relate to the presence of some interfacial water between the ice core and the mesoscopic glycerol- water domain. The glycerol concentration of this domain was enriched up to the critical concentration ~40 mol% by the freezing of the extra water that was free from the glycerol H-bond networks.

In the cases of 15-, 10-, and 5- mol% of glycerol-water mixtures, the ice cores have already been formed during the quenching down to the starting temperature of the *BDS* measurements and τ_{max} of the main relaxation process for all these mixtures shows values that are similar to those of 35 or 40 mol% glycerol-water mixtures (see Figure 40c). Furthermore, the two additional relaxation processes (due to ice and interfacial water) also traced the same

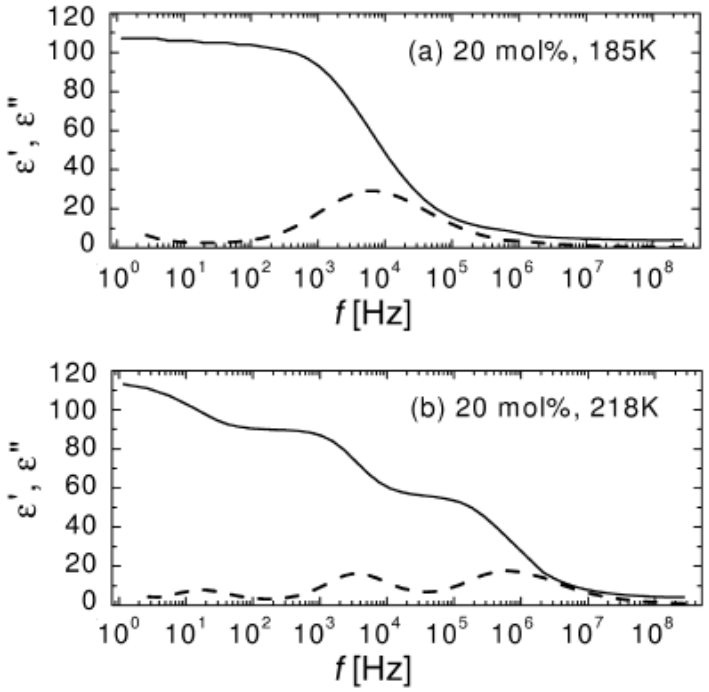

Figure 41. Typical dielectric spectra of 20 mol% of glycerol—water mixtures at (a) 185 K (supercooled state) and (b) 218 K (frozen state), where solid and dashed curves show the real and imaginary parts of complex dielectric permittivity. Each relaxation process in the frozen state was fitted by (114) and by Cole–Cole and Debye relaxation functions, respectively, in order to separate the main process, the process due to interfacial water, and the process due to ice. (Reproduced with permission from Ref. 244. Copyright 2005, American Chemical Society.)

lines, respectively. It is worth noting that the activation energy of ~33 kJ/mol of the relaxation process resulting from interfacial water is similar to the reported values ~28 kJ/mol for bound water on protein-surfaces in aqueous solutions [246] and ~30-40 kJ/mol for surface water on porous glasses, depending on the porous glass preparation [256]. The relaxation time for this interfacial water is ~100 times larger than that for the bound water reported in protein solutions [246]. In the case of bound water in protein solutions, this interfacial water is surrounded by fast-mobile water molecules from the solvent. In the case of the water-rich glycerol-water mixtures the interfacial water molecules would be confined between two slow regions such as the ice and glycerol-water domains, therefore, mobility of the interfacial water in water-glycerol mixtures would be highly restricted.

The glass transition temperature (T_g), which is defined as the temperature where the relaxation time is 100 sec [247,248], was evaluated for glycerol-water mixtures using

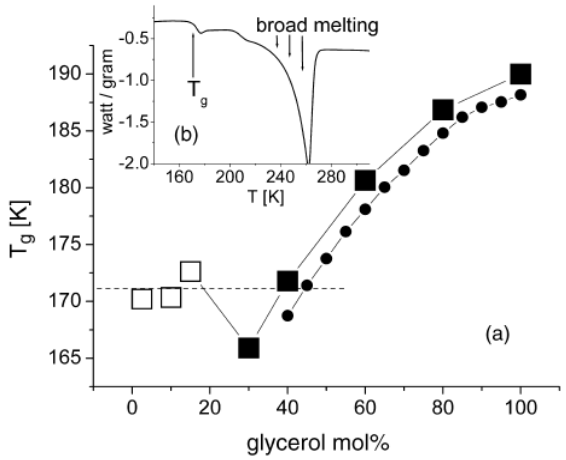

Figure 42. (a) Glycerol concentration dependence of the glass-transition temperature obtained by DSC measurements (filled box represnts supercooled state, unfilled box represents frozen state) and by BDS data (filled circle) (b) Typical raw data of DSC measurements (10 mol% of glycerol), where the glass transition and a broad melting behavior were observed. (Reproduced with permission from Ref. 244. Copyright 2005, American Chemical Society.)

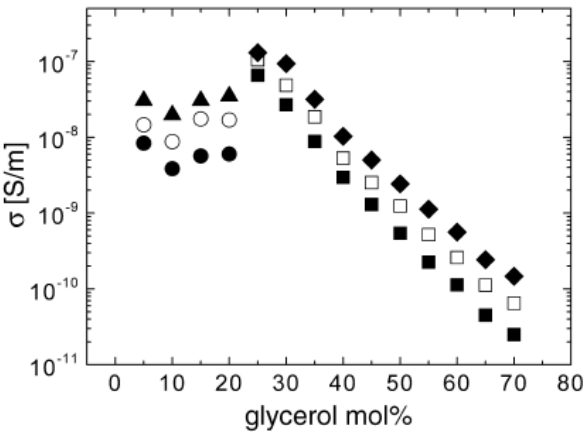

Figure 43. Glycerol concentration dependence of dc-conductivity (filled box represents supercooled state at 209 K, filled circle represents frozen state at 209 K, open box represents supercooled state at 212 K, open circle represents frozen state at 212 K, filled diamond represents supercooled state at 215 K, and filled triangle represents frozen state at 215 K). (Reproduced with permission from Ref. 244. Copyright 2005, American Chemical Society.)

temperature dependencies of τ_{max} for the main dielectric relaxation process (See Figure 40a). As shown in Figure 42a, the glass transition temperatures (T_g) obtained by *DSC* measurements were in good agreement with *BDS* data. It is worth pointing out that T_g for 2.5-, 10-, and 15- mol% of glycerol-water mixtures in the frozen state all have the same values as the T_g for 40 mol% of the glycerol-water mixture. This result indicates that the glass transition observed in frozen state results from the mesoscopic glycerol-water domains of 40 mol% glycerol. Moreover, even simple dc-conductivity data obtained by *BDS* at particular temperatures show concentration independent behaviors in the frozen state, and the values are close to that of 40- or 35- mol% of glycerol (Figure 43). Note that these results support the hypothesis that the mechanism of dc-conductivity in a supercooled state is most likely that of defect translocation as discussed recently [208], possible because the increase of ionic impurities did not affect the frozen state as shown in Figure 43.

In order to estimate the ratio between the amounts of water in the mesoscopic glycerol-water domains, interfacial water and ice in glycerol-water mixtures, one can use the melting-enthalpy ΔH obtained from *DSC* data. Note that in this specific case, the total

melting-enthalpy (ΔH) was obtained by integration of the transition heat capacity (ΔC_P) over the broad melting temperature interval:

$$\Delta H = \int_{T_1}^{T_2} \Delta C_P dT = \int_{T_1}^{T_2} \left(C_P - C_{P(baseline))} \right)_p dT \quad , \tag{5.67}$$

where T_1 is the starting temperature of the broad melting (223 K for 10 mol% glycerol, see Fig. 42b), T_2 is the temperature of the phase transition, and $C_{P(base\ line)}$ is the extrapolated heat capacitance base line in the same temperature interval [226]. Thus, amount of ice below the starting temperature of the broad melting was estimated by the ratio (ΔH / ΔH_0) where ΔH_0 is the melting-enthalpy of bulk ice [249]. Using the known total amount of water and the critical 40 mol% concentration, we can estimate that in the 10 mol% of the glycerol-water mixture, for example, we have approximately 50 mol% of ice, 15 mol% of water in the mesoscopic domains, and 25 mol% of interfacial water. This estimation using *DSC* data also shows the presence of a significant amount of interfacial water in the frozen state of glycerol-water mixtures.

According to this fact the existence of three water states: water in glycerol H-bond networks ($H_2O_{(GW)}$), water in ice structure ($H_2O_{(ice)}$) and the interfacial water ($H_2O_{(interface)}$) can be considered. Let us discuss a possible kinetic mechanism of the broad melting behavior. The relations between the three states of water can be described by

$$H_2O_{(GW)} \underset{k_2}{\overset{k_1}{\rightleftharpoons}} H_2O_{(interface)} \underset{k_4}{\overset{k_3}{\rightleftharpoons}} H_2O_{(ice)} , \tag{5.68}$$

where k_1, k_2, k_3, and k_4 are the reaction rates (e.g., the reaction velocity from $H_2O_{(GW)}$ to $H_2O_{(interface)}$ is described by $v_1 = k_1\ [H_2O_{(GW)}]$, where $[H_2O_{(GW)}]$ is the mole concentration of $H_2O_{(GW)}$). If the system is in an equilibrium state, apparently $[H_2O_{(interface)}]$ does not change. Therefore it can be described as $k_1\left[H_2O_{(GW)}\right] + k_4\left[H_2O_{(ice)}\right] = \left(k_2 + k_3\right)\left[H_2O_{(interface)}\right]$. Let us consider one particular concentration of glycerol-water mixture in the water-rich region. Due to the critical concentration of the 40 mol%, it is reasonable to assume that $[H_2O_{(GW)}]$ is not dependent on temperature, and it is clear that the total mole concentration of water (C_{total}) is constant. Therefore, the concentration of $H_2O_{(interface)}$ can be described by $\left[H_2O_{(interface)}\right] = C_{total} - \left[H_2O_{(ice)}\right]$. Thus, one can obtain:

$$\left[\mathrm{H_2O_{(interface)}}\right] = \frac{k_1\left[\mathrm{H_2O_{(GW)}}\right] + k_4 C_{total}}{k_2 + k_3 + k_4} \quad . \tag{5.69}$$

It is reasonable to assume that $k_1 \cong k_2$ because the water exchange in both directions between $[H_2O_{(GW)}]$ and $[H_2O_{(interface)}]$ are caused by the same rearrangement of mesoscopic structures of H-bond networks of the glycerol-water mixture. In other words, both k_1 and k_2 are related to the relaxation time of the mesoscopic glycerol-water domain. Furthermore, it is clear that the probability of a water molecule to return back to the interface from the ice core is much smaller than in the reverse direction and hence $k_3 >> k_4$. Thus, finally we can obtain

$$\left[\mathrm{H_2O_{(interface)}}\right] \cong \frac{\frac{k_2}{k_3}\left[\mathrm{H_2O_{(GW)}}\right]}{1+\frac{k_2}{k_3}} \cong \frac{C\frac{k_2}{k_3}}{1+\frac{k_2}{k_3}} \quad , \tag{5.70}$$

where C is a constant. Taking into account that the total water amount is a constant value the relation (5.70) shows that any increase of the ratio k_2/k_3 leads to a decrease of ice core and an increase of $H_2O_{(interface)}$. It clarifies the broad melting behavior of the glycerol-water mixture shown by *DSC* measurements, and explains why τ_{max} does not follow the 40 mol% curve at higher temperatures (Figure 40c). In this temperature region, a faster replacement between $H_2O_{(GW)}$ and $H_2O_{(interface)}$ allows the mixture to retain more water in the supercooled phase than the expected amount based on the critical concentration of 40 mol%.

Hence, we can assume the following physical picture of dynamic and structural behavior of water-glycerol mixtures in the considered frequency-temperature landscapes for different concentrations of components (See Figure 44). As one can see, for high concentrations of glycerol including pure dehydrated glycerol, the universality evident in the master plots of temperature and concentration is related to the same origin of the elementary molecular process. It is most likely the result of a "defect" formation and its resultant percolation though the H-bond network.

The proposed new dielectric function (See (5.63)) can describe the whole spectra (*dc* conductivity, the main process and the excess wing) using only two free variables and a set of universal parameters.

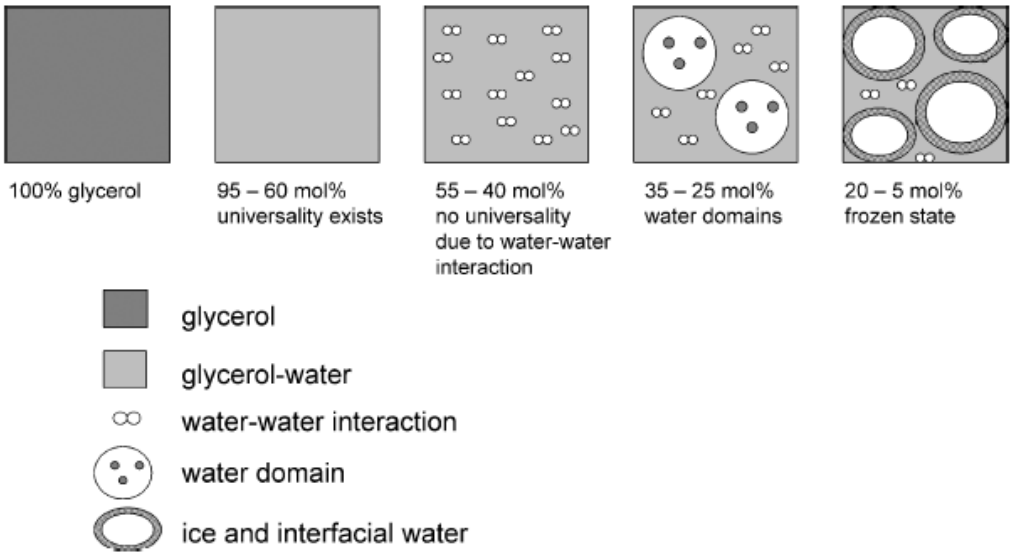

Figure 44. A schematic model of glycerol–water H-bonding liquids in different concentration of components.

Below 40 mol% of glycerol-water domains appear. This critical concentration is related to the numbers of H-Bonds of glycerol and of water respectively. *DSC* studies also confirm the same critical concentration. In water-rich mixtures, some water is frozen and as a result three relaxation processes where observed. These were related to ice like structures, interfacial bound-water and glycerol-water mixtures in the mesoscopic domains, where the concentration remains at 40 mol%.

Thus, concluding this section, we can summarize that H-bond liquids can be regarded as a model systems which reproduce many basic features of liquid glass forming materials. The reasoning behind this is that the interaction between their constituents provides cooperative properties of the system as a whole. In particular glycerol-water mixture, depending on their composition, may exhibit a variety of relaxation properties: from properties of homogeneous solutions to those of binary mixtures.

5.5 Liquid-like behavior in doped ferroelectric crystals

In the previous section we considered in detail the behavior of liquid glass forming substances. However, such liquid-like behavior can be also inherent to the dielectric properties of crystalline samples.

Now let us discuss such behavior as was recently observed in doped ferroelectric crystals in the paraelectric phase (See Section 4.3). As Process **B** was observed only in crystal #1 (see Figure 18) it must be attributed to the presence of the Cu impurities embedded at random in the KTN crystal. The Arrhenius nature of the process at elevated temperatures above 354 K indicates normal relaxation of the independent Cu^+ ions [179]. These ions are significantly smaller than the K^+ sites in which they reside (The radii of the Cu^+ and the K^+ ions are 0.77 Å and 1.52 Å respectively [250]), leading to off-center displacements. The Cu^+ ions can therefore hop between the eight symmetrical minima of their potential wells. Indeed, the energy of activation of $E_a^B = 0.37\,eV$ corresponds to the activation energies for the hopping of transition metal ion impurities in $KTaO_3$ [251].

VFT behavior has been noted in crystal systems with a dipole glass phase [176]. However the *VFT* behavior in crystal #1 is related to the relaxation of the Cu^+ ions in the paraelectric phase and is more akin to relaxations in glass forming liquids [179]. The formulism of Adam and Gibbs [63] (A&G) has been successfully applied to such systems. According to the A & G theory, this behavior originates from the cooperative rearrangement of some clusters. It is well established that in KTN crystals in the paraelectric phase the Nb^{+5} ions are displaced from the center of inversion of the unit cells [172]. These displacements form dipolar clusters with a correlation length that increases as the system is cooled towards the ferroelectric phase transition. We propose that the cooperative relaxation observed at T<354 K is produced by the interaction between such dipolar clusters that form around the relaxing Cu^+ ions, and that act as the rearranging clusters in the A & G model. Adopting the formalism of A & G [63] the minimum cluster size *z*, is related to the rate of relaxation *P(T,z)* by

$$P(T,z) \propto \exp\left(-z\frac{\Delta\mu}{k_B T}\right). \tag{5.71}$$

VFT behavior is obtained by equating $z = \frac{T}{T - T_{VFT}}$ and noting that $\Delta\mu = E_{VFT}$ [65]. Fitting the *VFT* model to the experimental results of τ^B in the paraelectric phase gives T_{VFT}=228 and

$\Delta\mu$=0.02 eV. Identifying the temperature at which τ^B deviates from the Arrhenius model with the onset of cooperativity yields a minimum cluster size given by

$$z = \frac{T_x}{T_x - T_k} = 2.8 \ . \tag{5.72}$$

This coincides well with an estimation of the minimum size of the dipolar cluster formed around nearest neighbors Nb^{+5} ion given by $\left[Nb^{+5}\right]^{-1} = \left[0.38\right]^{-1} \approx 2.63$. At elevated temperatures (T>354 K), the Nb^{+5} ions hop at random between equivalent minima of their potential wells within their site in the unit cell. As the phase transition is approached these ions form a dipolar cluster around the Cu^{+} ions that are randomly distributed far apart from each other. These clusters are at first of a minimum size containing only the Nb^{+5} ions that are closest to the Cu^{+} ion. As the phase transition is approached further the cluster size around the Cu^{+} ion grows accordingly. These represent the rearranging clusters of the A & G theory.

An independent assessment of the validity of the A & G interpretation to the Cu^{+} induced relaxation (Process **B**) was provided by direct estimation of the configurational entropy at the ferroelectric phase transition. The phase transition is dominated by a shift in the position of the Nb^{5+} ion in relation to the lattice. The coupling between the Cu^{+} ions and the Nb^{5+} polar clusters, evident in the paraelectric phase, will further contribute to the configuational entropy of the phase transition.

It is well known that the configurational entropy can be evaluated from the heat capacitance of the crystal, derived from *DSC* measurements, by the integral

$$S_C(\Delta T) = \int_{\ln T_1}^{\ln T_2} \left[C_p(\ln T) - C_p(baseline)\right] d(\ln T) \ , \tag{5.73}$$

where T_1 is the onset and T_2 is the completion of the phase transition, and $C_P(baseline)$ is the extrapolated baseline heat capacitance in the temperature interval [226]. The results for the pure KTN crystal (#2) and the Cu-doped KTN crystal (#1) are presented in Figure 45. The resulting difference was found to be $\Delta S = 0.79\times10^{-3} Jg^{-1}$. Normalized to the Cu^{+} -ion content we have per Cu^{+} -ion $\Delta S_{Cu} = 2.068\times10^{-21} J \approx 0.013\ eV$. This result is in a good agreement with $\Delta\mu = 0.02\ eV$ derived from fitting the *VFT* model to τ^{B}(T), given the spatial variation of the Cu concentration in the crystal.

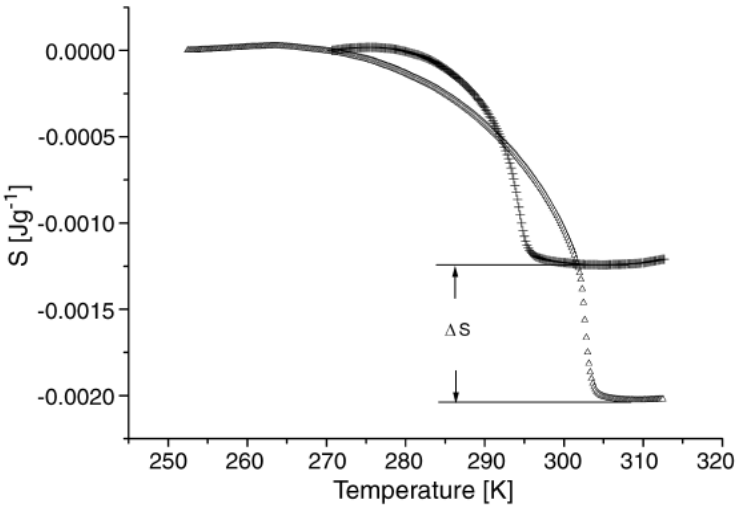

Figure 45. The configurational entropies of the ferroelectric phase transition for crystals #1 (Δ) and #2 (+). The difference in entropy between the two crystals, ΔS, is 0.79×10^{-3} Jg^{-1} and this is assigned to the Cu^{+} dopants. The DSC measurements were made with the cooling and heating rates 5 K/min in an interval ranging from 373 K to 220 K using a DSC 2920 calorimeter (TA Instruments) [179]. (Reproduced with permission from Ref. 179. Copyright 2004, The American Physical Society.)

At the onset of the ferroelectric phase transition the Cu^{+} ions are frozen and no longer constitute the seed of the relaxation process. In this respect the ferroelectric phase transition "quenches" the glass-forming liquid. Below the phase transition temperature, the dipolar clusters surrounding the Nb^{5+} ions merge to yield the spontaneous polarization of the (now ferroelectric) crystal, and due to the strong crystal field, the off-center potential minima of the Cu^{+} ions are no longer symmetrical.

Thus, one may summarize the physical picture of the relaxation dynamics in KTN crystal doped with Cu^{+}-ions in the following way: In the paraelectric phase, as the ferroelectric phase transition is approached, the Nb^{5+} ions form dipolar clusters around the randomly distributed Cu^{+} impurity ions. The interaction between these clusters gives rise to a cooperative behavior according to the AG theory of glass-forming liquids. At the ferroelectric phase transition the cooperative relaxation of the Cu^{+} -ions is effectively "frozen."

5.6 Relaxation Kinetics of Confined Systems

It was already mentioned in Section 2.3 of this paper that kinetics associated with relaxation parameters measured by dielectric spectroscopy can provide significant information about the substance under study. Even without the quantitative data, having only qualitative information, one can, for example, identify a glassy material by non liner *VFT* relaxation time dependence. In this section we will discuss another type of relaxation kinetics which is associated with confined systems and we will illustrate this type using some experimental examples.

5.6.1 Model of relaxation kinetics for confined systems

The model we utilize here, was first introduced to describe the relaxation properties of water adsorbed on the inner surfaces of porous glasses [155] and which was then reviewed in [78]. The main idea of this model is that the relaxation kinetics in this case is provided in this case by a process that must satisfy two statistically independent conditions. Thus, if one assigns the probability p_1 to satisfy the first condition and p_2 to satisfy the second condition, then the probability p for a relaxation act to occur in such a system is

$$p = p_1 p_2 . \tag{5.74}$$

Let us discuss a system, which consists of a number of particles where their relaxation is provided by the reorientations (a jump or another type of transition) of particles between two local equilibrium states. In the spirit of the Arrhenius model (2.26), the first requirement for the relaxation is that the particles have enough energy to overcome the potential barrier E_a between the states of local equilibrium for the elementary constituents of the system under consideration. Thus,

$$p_1 = \exp\left(-\frac{E_a}{k_B T} \right) . \tag{5.75}$$

The essential idea of the new model is that p_2 is the probability that there will be enough free volume, v_f, in the vicinity of a relaxing particle with its own volume, v_0, to allow reorientation [69,70,78,155]. In other words we imply that in order to participate in a relaxation a particle must have a ‘defect’ in its vicinity. Then,

$$p_2 = \exp\left(-\frac{v_0}{v_f}\right). \tag{5.76}$$

In itself this probability represents a kind of constraint for the entire relaxation process and slows down the relaxation. Combining (5.73)-(5.76) and taking into account the relationship $\tau \sim 1/p$ the following expression can be obtained:

$$\ln\left(\frac{\tau}{\tau_0}\right) = \frac{E_a}{k_B T} + \frac{v_0}{v_f}. \tag{5.77}$$

As mentioned earlier in Section 2.3 it is usually assumed that free volume grows with increasing temperature. This idea reflects thermal expansion, i.e. if the number of relaxing particles in the system is kept constant, then the thermal expansion leads to an increase of free volume with temperature growth. However, this assumption may be wrong for the case of the confined system where the total volume is kept constant, but the number of relaxing particles varies. In our case we implied earlier that the microscopic act of relaxation is conditional to the presence of a defect in the vicinity of the relaxing particle. As a first approximation one may assume that the number of defects, n, obeys the Boltzmann law $n = n_0 \exp(-E_b / k_B T)$. Then, the free volume per relaxing particle, $v_f = V/n$, where V is the total volume of the system. Thus, instead of (5.77) one immediately obtains [78,155]

$$\frac{\tau}{\tau_0} = \exp\left[\frac{E_a}{k_B T} + C\exp\left(-\frac{E_b}{k_B T}\right)\right], \tag{5.78}$$

where E_b is the energy to enable an inert particle to participate in relaxation (or alternatively the energy required to form a so-called "defect"), $C = v_0 n_0 / V$ is a confinement factor, and n_0 is the maximal possible number of defects in the considered system. In contrast to all other kinetics models (5.78) exhibits a non-monotonic temperature dependency since it is related to two processes of a different natures: the Arrhenius term reflecting the activated character of the relaxation process, and the exponential term reflecting a decrease of free volume per relaxing particle with temperature growth. This second term is a consequence of constant volume constraint and the implication that the number of relaxing particles obeys Boltzmann law. If the total volume of the system V is sufficiently large and the maximum possible concentration of relaxing particles is sufficiently small $n_0 / V << 1/v_0$, then the free volume

arguments become irrelevant and relaxation kinetics maintain Arrhenius form. However, in the case of a constraint, when the volume of a system is small and $n_0/V \approx 1/v_0$, an increase of temperature leads to a significant decrease of free volume and slows down the relaxation. As we will show, this situation usually occurs for "small" systems where relaxing particles become able to participate in relaxation due to the formation of some "defects" in the ordered structure of the system. In this case n_0 could be regarded as the maximum possible defect concentration. Therefore, confinement provides a comparatively large concentration of defects n_0/V since for such a system the confining geometry affects comparatively larger amount of system constituents.

5.6.2 Dielectric relaxation of confined water

It is known [52] that the dielectric relaxation of water is due to the reorientation of water molecules that have a permanent dipole moment ($6\cdot10^{-30}$ C m or 1.8 D). It is also known that in bulk water and ice water molecules are embedded in the network structure of hydrogen bonds. Thus, the reorientation of a water molecule leading to the dielectric relaxation may occur only in the vicinity of a defect in the hydrogen bonds network structure. This mechanism fits perfectly to the relaxation model described in the section above. Thus, one may expect that a confined water sample could exhibit the non-monotonous relaxation kinetics predicted by (5.78). In this case, E_a could be regarded as the activation energy of reorientation of a water molecule, and E_b as the defect formation energy. Here we discuss the dielectric relaxation of water confined in porous glasses [153,155]. The main features of this relaxation were already described in Section 4.2.1 of this tutorial. In Figure 14 one can clearly see the non-monotonous saddle-like process (Process II) which will be discussed here. Similar non-monotonous relaxation behavior was also observed for water confined in zeolites [252,253].

Figure 46 shows three curves corresponding to the three different porous glasses samples **A**, **B** and **C** that differ in their structure (average pore diameter) and chemical treatment [153]. The fitting curves presented in these figures show that the model (5.78) is in good agreement with the experimental data.

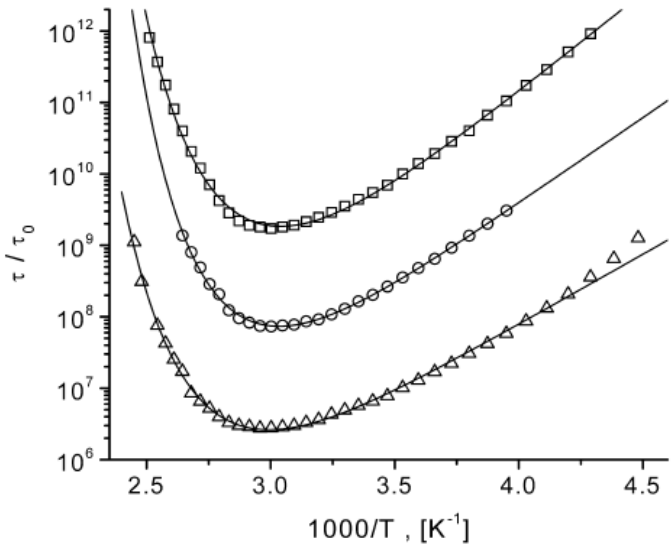

Figure 46. Temperature dependency of the dielectric relaxation time of water confined in porous glasses [153,155]. Symbols represent experimental data. Full lines correspond to the best fit according to Eq. (129). Sample A (cycles) $\ln\tau_0 = -27 \pm 0.5$, $E_a = 46 \pm 1$ kJ/mol, $E_b = 33 \pm 1$ kJ/mol, $C = 27\times10^4 \pm 9\times10^4$. Sample B (boxes) $\ln\tau_0 = -33 \pm 0.5$, $E_a = 53 \pm 1$ kJ/mol, $E_b = 29 \pm 1$ kJ/mol, $C = 7\times10^4 \pm 2\times10^4$. Sample C (triangles) $\ln\tau_0 = -26 \pm 0.3$, $E_a = 38 \pm 1$ kJ/mol, $E_b = 32 \pm 1$ kJ/mol, $C = 12\times10^4 \pm 3\times10^4$. (Reproduced with permission from Ref. 78. Copyright 2004, The American Physical Society.)

The fitted values of E_a and E_b for all the samples are in fair agreement with the energies attributed to the water molecules reorientation and defect formation for the bulk *ice I*, that are evaluated as 55.5 kJ/mol and 32.9 kJ/mol, respectively [78]. This fact leads to the conclusion that most probably the water confined in small pores is quite immobile and represents a kind of ice-like structure. For the further discussion more detailed information about the samples should be recalled. For example, let us discuss the relationship between the pore network structure and fitted activation energies E_a and E_b. The pore diameters of samples **A** and **B** are nearly the same (~50 nm), while the chemical treatment of these samples is different. Glass **B** was obtained from Glass **A** via an additional immersion in KOH solution. Sample **C** has pores with an average diameter of 300 nm and, as in the case of sample **A**, was not especially purified with KOH [153,155].

It follows from the fit presented in Figure 46 that E_b energies for all porous glass samples are about the same value of 33 kJ/mol. However, for sample **B** the value of E_b is about 10% less than those for samples **A** and **C**. This fact can most likely be explained by the additional chemical treatment of sample **B** with KOH, which removes the silica gel from the inner surfaces of the pore networks. It is reasonable to assume that the defects generally form

at the water interfaces, and only then penetrates into the water layer. Thus, it seems that the KOH treatment decreases the interaction between the water and inner pore surfaces and, consequently, decreases the defect formation energy E_b.

5.6.3 Dielectric relaxation in doped ferroelectric crystal

As discussed in Section 5.5, the appearance of the "saddle-like" relaxation process in KTN:Cu crystal is linked to two facts: (i) it appears only in the Cu doped crystals, and (ii) its appearance coincides with the onset of the ferroelectric phase transition.

We propose that following the onset of the phase transition the small Cu+ ions residing in the large K+ sites, are shifted to an off-center position and produce a distortion in the neighboring unit cells. This gives part of each of these unit cells the latitude to behave as a relaxing dipole. In a pure (copper free) crystal these dipoles are closely interlaced with the complementary part of their respective unit cells, and hence do not have the latitude to reorient. For this reason, the relaxation process that is linked with these dipoles is not observed in the pure KTN crystal.

In order to derive the temperature dependence of the relaxation time associated with this process we shall consider a one-dimensional model in which the Cu^+ ions reside in an asymmetric double potential well as illustrated qualitatively in Figure 47.

At a given temperature, the Cu^+ ions are distributed between two states: "high" and "low". If $[Cu^+]$ is the molar concentration of the Cu^+ ions in the crystal, then according to Boltzman statistics, the concentrations of the Cu^+ ions in their respective states are given by

$$[Cu^+]_H = [Cu^+] \cdot \exp\left(-E_b / k_B T\right), \tag{5.79}$$

$$[Cu^+]_L = [Cu^+] \cdot \left[1 - \exp\left(-E_b / k_B T\right)\right], \tag{5.80}$$

where $[Cu^+]_H$ and $[Cu^+]_L$ are the molar concentration of the Cu^+ ions in the "high" and "low" states respectively.

As the crystal is cooled below the phase transition temperature, the relaxation time decreases until it reaches a minimum, after which it follows an Arrhenius law. It is therefore reasonable to assume that the minimum point coincides with the temperature at which the great majority of the Cu^+ ions are at the "low" state. From this point onwards, as the crystal continues to be cooled, all the dipoles that are available to participate in the process are relaxing, yielding an Arrhenius relaxation time.

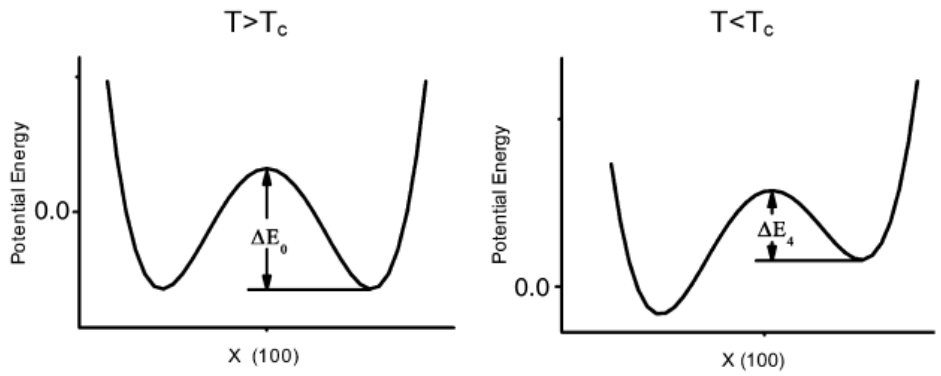

Figure 47. A schematic representation of the double-well potential of the Cu^+ ions. In the ferroelectric phase, local fields distort it and it becomes asymmetrical. (Reproduced with permission from Ref. 257. Copyright 2005, Elsevier Science B.V.)

Based on this argumentation we claim that (v_o/v_f) in equation (5.76) is inversely proportional to the number of Cu^+ ions that are in the low state such that

$$p_2 = \exp\left(-Ce^{-E_b/k_BT}\right). \tag{5.81}$$

This leads to the saddle-like behavior of the relaxation time as described in equation (5.78). The fitting of (5.78)) to the experimental data of the ferroelectric phase is presented in Figure 21. As can be seen, in the temperature range 230K to 290K the model fits the experimental data very well, yielding: $\tau_o{}^B$=1.5±0.7·10^{-9} sec., E_a=0.12±0.01 eV, and E_b=0.34±0.12 eV. A comparison of E_b to the energetic barrier separating equivalent sites for Cu^+ ions in the paraelectric phase, ΔE=0.37±0.01 eV [179], strongly indicates that the Cu^+ ions assume the role of the defect.

In summary, we maintain that while the free volume concept is an intuitively natural concept for liquids confined in a host matrix, it is not an obvious model for ionic/covalent crystals. Saddle-like relaxation is not a universal feature of all crystals. Hence, V_f, the free volume necessary for the relaxation to occur cannot be attributed to the presence of any defect that causes an irregularity in the crystal structure. In the special case of KTN:Cu crystal, the Cu^+ ion has an effective ionic radius that is smaller than to that of the original occupant of its site (K^+), while having the same ionization state. Below the ferroelectric phase transition temperature the Cu^+ ions are shifted to an off-center position in their respective sites. This allows some of the constituents of the original KTN unit cells in the vicinity of the Cu^+ ions to assume the behavior of relaxing dipoles. As the number of these dipoles is constrained by the number of Cu^+ ions that are frozen in the off-centre position, this yields a saddle- like

relaxation process. The question remaining is what is the relaxing dipole? A number of authors have noted dynamic relaxation of the octahedra in various perovskites and related structures [254-256]. In general the relaxation is Arrhenius in nature with energies of activation ranging between 0.05 eV to 0.24 eV. The soft mode phonon is dominated by the oxygen octahedra and its interaction with the Nb ion. As noted above, there is a strong coupling of the Cu^{+} ions to the soft mode phonon. Given that the activation energy of the Arrhenius tail of the saddle is in the range noted it is not unreasonable to assign dynamic relaxations of the octahedra as the relaxing dipole [257].

5.6.4 Possible modifications of the model

All the examples described above show that confinement in different cases may be responsible for non-monotonous relaxation kinetics and can lead to a saddle-like dependence of relaxation time versus temperature. However, this is not the only possible reason for non-monotonous kinetics. For instance, work [258] devoted to the dielectric study of an antiferromagnetic crystal, discusses a model based on the idea of screening particles. Starting from the Arrhenius equation and implying that the Arrhenius activation energy has linear dependency on the concentration of screening charge carriers, the authors of [258] also obtained an expression that can lead to non-monotonic relaxation kinetics under certain conditions. However, the experimental data discussed in that work does not show clear saddle-like behavior of relaxation time temperature dependence. The authors of [258] do not even discuss such a possibility.

At the same time, model (5.78) is also open to modifications. This model is based on the assumptions (5.75) and (5.76) regarding temperature dependencies for the probabilities p_1 and p_2. Assuming, instead of the Arrhenius law (2.26), a cooperative term of the *VFT* (2.28) type for p_1, the temperature dependence of the relaxation time is obtained in the form

$$\ln\left(\frac{\tau}{\tau_0}\right) = \frac{D\,T_k}{T - T_k} + C\exp\left(-\frac{E_b}{k_B T}\right), \tag{5.82}$$

where the first term of the *VFT* type on the right hand side of Eq. (5.78) could express the idea of cooperative behavior in accordance with the Adam-Gibbs model [63].

5.6.4.1 Confined glassy water

The experimental data for water confined in the porous glass sample **C** that was discussed previously (see Figure 46) is well fitted with (5.82) as presented in Figure 48.

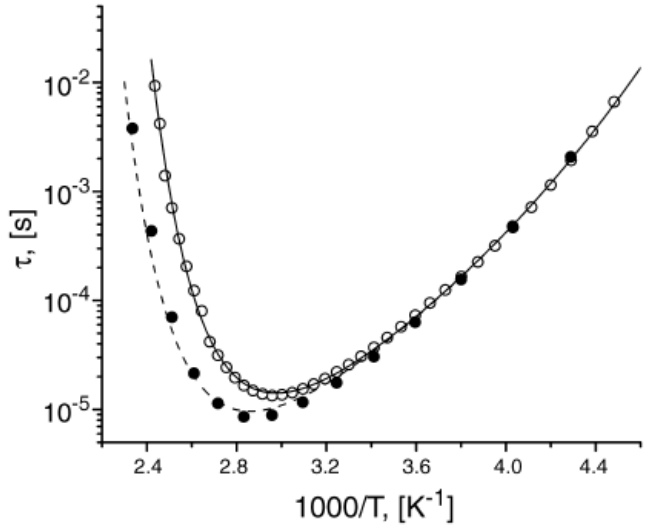

Figure 48. Temperature dependence of dielectric relaxation time for water confined in sample C. The data were measured under different conditions and contain a different amount of water: Unfilled circles correspond to the data presented early in Fig. 46; filled circles represent the experiment with reduced water content [78]. Full line is the best fit according to (133): $\ln\tau_0 = -17.8 \pm 0.5$, $E_b = 39 \pm 1$ kJ/mol, $T_k = 124 \pm 7$ K, $D = 10 \pm 2$, $C = 9\times10^5 \pm 3\times10^5$. The dashed line was simulated from (133) for the same $\ln\tau_0$, E_b, T_k and D, but with C divided by a factor 1.8 (explanation in the text). (Reproduced with permission from Ref. 78. Copyright 2004, The American Physical Society.)

Compared to the other samples, this porous glass has the largest pore diameter and humidity [153,156]. Therefore, it is reasonable to assume that the cooperative relaxation properties, described by the *VFT* term, should be more pronounced for this sample. It is worth noting that the fitted value of the Kauzmann temperature $T_k = 124 \pm 7$ K (see caption for Figure 48). From T_k, using the empirical rule $T_g \sim 1.1 \div 1.2\ T_k$ [14], the estimation $T_g \sim 145$ K of the water glass transition temperature could be obtained. This value is in fair agreement with usual estimations of T_g for water that are expressed by interval $T_g \approx 130 \pm 6$ K [259,260]. The fitted value of fragility $D = 10 \pm 2$ is close to the estimations of this parameter $D \approx 8$ that have been derived from the diffusivity data for the amorphous solid water in work [260]. These findings may also support the idea that the porous glass samples treated in the preceding discussion dealt with a kind of non-crystalline state of water. The most probable reason for this is that the pore walls provide the necessary confinement. Note that in the

porous glasses, the glassy properties of water can be observed at comparatively high temperatures such as room temperature, whereas the usually quite low temperatures and special treatment [259,260] are required to obtain glassy water. However, further investigations are required to support these experimental findings.

5.6.5 Relationships between the static properties and dynamics

Let us now consider the relationship between the data obtained from the kinetics to the amplitude of this process. The data for water confined in porous Glass **C** can be discussed in terms of equilibrium properties of the considered relaxation processes obtained in the two different experiments [78]. The two experimental runs presented in Figure 49 are quite similar at low temperatures. However, in the high temperature range, they exhibit a remarkable difference from each other.

In Figure 49, the temperature dependencies of the so-called dielectric strength $\Delta\varepsilon$ for these experiments are presented. The dielectric strength is the difference between the high and low frequency limits of the real part of the complex dielectric permittivity of the process under consideration. This quantity reflects the concentration of dipole moments n_d in a sample and, in its simplest approximation, is in linear proportion to the concentration

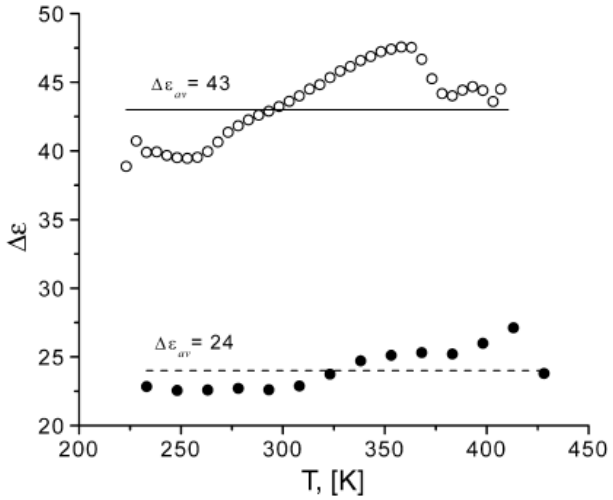

Figure 49. Temperature dependence of the dielectric strength $\Delta\varepsilon$ for sample C. Symbols represent experimental data corresponding to the relaxation times presented in Fig. 48: unfilled circles correspond to the data presented early in Fig. 46; filled circles represent the experiment with reduced water content [78]. The lines mark values of the averaged dielectric strength $\Delta\varepsilon_{av}$ for these experiments. (Reproduced with permission from Ref. 78. Copyright 2004, The American Physical Society.)

$\Delta\varepsilon \sim n_d$ [6,7], i.e. the dielectric strength is proportional to the water content. Thus, the two experimental runs presented in Figure 49, as well as the data in Figure 48, correspond to the two different amounts of water in sample **C**.

Recall that the pre-exponential factor $C = v_0 n_0 / V$, where n_0 is the maximum possible number of defects. This number is proportional to the water content and $C \sim n_0 \sim n_d \sim \Delta\varepsilon$. The dielectric strength $\Delta\varepsilon$ for these runs is almost constant (the variations of $\Delta\varepsilon$ are about 5% of the averaged value for both runs). By comparing the averaged values of $\Delta\varepsilon$ for these runs the difference in water content between these experiments has been estimated to be 1.8 times (see Figure 49). The pre-exponential factors C for these two runs should also be different by the same factor. The comparison in Figure 48 shows that this is indeed so.

Finally we can conclude that confinement could be responsible for the non-monotonic relaxation kinetics and could provide a specific saddle-like temperature dependency of relaxation time. The experimental examples discussed show that this type of kinetics may be inherent to systems of completely different natures: confined liquids, ferroelectric crystals, and it was even demonstrated recently macromolecular folding kinetics [78]. In each case, the specific interpretation of the parameters of model (5.78) depends on the discussed experimental situation. We are far from the opinion that confinement is the only reason for non-monotonic relaxation kinetics. However, for all the examples discussed in this paper, the non-monotonic dependence of the relaxation time on temperature has the same origin, that is, confinement either in real or configurational space.

5.7 Dielectric Spectrum Broadening in disordered materials

In the previous sections, we presented several examples of the non-exponential dielectric response in time domain. We also discussed the dielectric response in H-bonding networks and liquid like behavior in doped ferroelectric crystals. The models we presented in time domain enable us to determine some of the topological properties of the investigated complex systems. We also observed that frequency representation has its own advantages. In particular, the non-dissipative part of the system response to an external perturbation and the dissipative part are clearly separated in frequency domain as the real and imaginary part of the complex permittivity, while in time domain these effects are "mixed" together in the relaxation function. The separation of the response itself and the dissipative effects in time domain is not obvious, although it is possible to do in principle by using the appropriate integral transform.

In spite of the existence of a single mapping between the time and frequency domain by the Laplace transform, the separation in frequency representation may at times be more convenient for analysis of the dynamic processes in complex systems.

In Section 2.2 we classified several types of non-Debye relaxation and mentioned a few particular approaches which were developed in order to explain the origins of these relaxation patterns. Below we will discuss a model that considers one particular case of such non-exponential relaxation.

5.7.1 Symmetric Relaxation peak broadening in complex systems

As mentioned in Section 2.2, the dielectric response in frequency domain for most complex systems cannot be described by a simple Debye expression (2.17) with a single dielectric relaxation time. In a most general way this dielectric behavior can be described by the phenomenological Havriliak-Negami (*HN*) formula (2.21).

Usually, the exponents α and β are referred to as measures of symmetrical and unsymmetrical relaxation peak broadening. These names are a consequence of the fact that the imaginary part of the complex susceptibility for the *HN* dielectric permittivity shows power-law asymptotic forms $Im\{\varepsilon^*(\omega)\} \sim \omega^{\alpha}$ and $Im\{\varepsilon^*(\omega)\} \sim \omega^{-\alpha\beta}$ in the low- and high-frequency limits, respectively.

The experimental data shows that α and β are strictly dependent on temperature, structure, composition, pressure and other controlled physical parameters [87,261-265].

In this section we will consider the specific case of the *HN* formula $\beta = 1$, $0 < \alpha < 1$, corresponding to symmetric relaxation peak broadening or to the so-called Cole-Cole (*CC*) law [16]. The complex dielectric permittivity $\varepsilon^*(\omega)$ for the *CC* process is represented in the frequency domain as

$$\varepsilon^*(i\omega) = \varepsilon_\infty + \frac{\varepsilon_S - \varepsilon_\infty}{1 + (i\omega\tau)^{\alpha}} \quad . \tag{5.83}$$

In order to explain the non-Debye response (5.83) it is possible to use the memory function approach [22, 23, 31, 266-268]. Thus, the normalized dipole correlation function $\Psi(t)$ (2.22) corresponding to a non-exponential dielectric relaxation process obeys the equation

$$\frac{d\Psi(t)}{dt} = -\int_0^t m(t-t')\Psi(t')\,dt' \quad , \tag{5.84}$$

where $m(t)$ is the memory function, and t is the time variable. The specific form of the memory function is dependent on the features of relaxation.

After Laplace transform (2.15), in virtue of the convolution form, Eq. (5.84) reads as

$$pF(p)-1=-M(p)F(p) \quad , \tag{5.85}$$

where $F(p)$ and $M(p)$ are Laplace images of $\Psi(t)$ and $m(t)$. Combining (5.85) with (5.83) and taking into account the relationship between the complex susceptibility and the correlation function, (2.14), one can obtain the Laplace image of the memory function for the *CC* process in the form

$$M(p)=p^{1-\alpha}\tau^{-\alpha} \quad . \tag{5.86}$$

Since $0 < \alpha < 1$ the exponent in Eq.(5.86) $1-\alpha > 0$. The mathematical implication is that $M(p)$ (5.86) is a multi-sheet function of complex variable p. In order to represent this function in the time domain one should to select the Schlicht domain using supplementary physical explanations [135]. These computational constraints can be avoided by using the Riemann-Liouville fractional differential operator ${}_0D_t^{1-\alpha}$ (see definitions (5.46) (5.47)). Thus, one can easily see that the Laplace image of ${}_0D_t^{1-\alpha}[\Psi(t)]$ is

$$\hat{L}[{}_0D_t^{1-\alpha}[\Psi(t)]]=p^{1-\alpha}F(p)-C$$

where (5.87)

$$C=D_0^{-\alpha}[\Psi(t)]\Big|_{t=+0}.$$

Taking (5.87) into account we can rewrite Eq. (5.84) with the memory function (5.86) as follows

$$\frac{d\Psi(t)}{dt}=-\tau^{-\alpha}\,{}_0D_t^{1-\alpha}[\Psi(t)] \quad . \tag{5.88}$$

Note that the relationship between the complex susceptibility and correlation function (2.14), together with Eq. (5.83) leads directly to the requirement that C=0.

Equation (5.88) was already discussed elsewhere [22, 23, 31] as a phenomenological representation of the dynamic equation for the *CC* law. Thus, Eq. (5.88) shows that since the fractional differentiation and integration operators have a convolution form it can be regarded

as a consequence of the memory effect. A comprehensive discussion of the memory function (5.86) properties is presented in [22, 23]. Accordingly, Eq. (5.88) holds for some cooperative domain and describes the relaxation of an ensemble of microscopic units. Each unit has its own microscopic memory function $m_\delta(t)$, which describes the interaction between this unit and the surroundings (interaction with the statistical reservoir). The main idea of such an interaction was introduced in [22, 23] and suggests that $m_\delta(t) \sim \sum_i \delta(t_i - t)$ (see Figure 50).

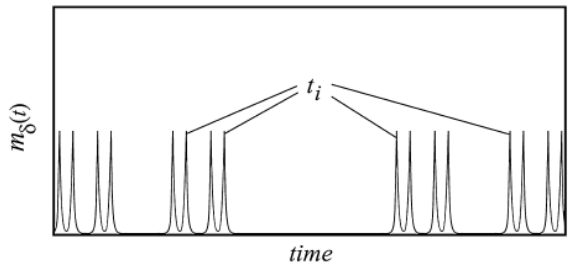

Figure 50. Schematic picture of $m_\delta(t)$ dependence. t_i are the time moments of the interaction that construct in time a fractal Cantor set with dimension $d_f = \frac{\ln 2}{\ln 3} \cong 0.63$. (Reproduced with permission from Ref. 2. Copyright 2002, Elsevier Science B.V.)

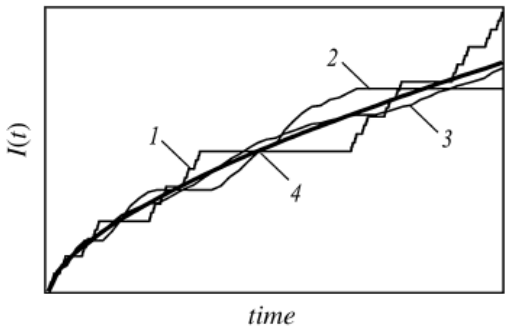

Figure 51. Schematic presentation which illustrates averaging of $m(t)$ over an ensemble of microscopic units. Curve 1 corresponds to the cooperative ensemble of a single microscopic unit with t_i distributed by the Cantor set. Curve 2 represents the ensemble of 3 units of the same type, Curve 3 represents 10 units. Curve 4 corresponds to 1000 units in the ensemble. The latter exhibits the power-law behavior $I(t) \sim t^{\ln 2/\ln 3}$. (Reproduced with permission from Ref. 2. Copyright 2002, Elsevier Science B.V.)

This term reflects the interrupted interaction between the relaxing unit and its neighbors. The time moments t_i (the time position of the delta functions) are the moments of the interaction. The sequence of t_i, constructs a fractal set (the Cantor set for example) with a fractal dimension $0 < d_f \leq 1$. This statement is related to the idea that cooperative behavior provides some ordering and long lasting scaling. Following these assumptions the memory function $m(t)$ for a cooperative domain can be obtained as a result of averaging over the ensemble of $m_\delta(t)$ (see Figure 51, where for more convenient representation $I(t) = \int_0^t m(t')dt'$

is plotted instead of $m(t)$). The requirements of measure conservation in the interval $[0, 1/\zeta]$ and conservation of the fractal dimension d_f for all $m_\delta(t)$ give this averaging as

$$m(t) = \int_{-1/2}^{1/2} m_\delta(\zeta^{-u} t)\zeta^{-u(1-d_f)} du$$

and (5.89)

$$M(p) \sim p^{1-d_f} \quad .$$

Thus, the memory function (5.86) is a cooperative one and the *CC* behavior appears on the macroscopic level after averaging over the ensemble of microscopic dipole active units. Comparing (5.86) and (5.89) one can establish that $\alpha = d_f$. This result once again highlights the fact that in this model the fractal properties on a microscopic level induce the power-law behavior of memory functions (5.86), (5.89) and *CC* permittivity (5.83) on a macroscopic level.

By definition [213, 220], the fractional dimension is given by

$$d_f = \alpha = \frac{\ln(N)}{\ln(\zeta)} \quad . \tag{5.90}$$

Here the scaling parameter ζ is the dimensionless time interval size and N is the number of delta functions (relaxation acts) in that interval. However, a characteristic time constant of the *CC* process is the relaxation time τ. Thus, the scaling parameter ζ and the relaxation time should be proportional to each other

$$\zeta = \frac{\tau}{\tau_0} \quad . \tag{5.91}$$

The constant minimal τ_0 is the cutoff time of the scaling in time.

In the general case, different physical conditions can determine the fractal properties of the microscopic memory function $m_\delta(t)$ and, consequently, the power-law time dependence of the macroscopic memory function (5.89). However, there is a computer simulation proof [269] that an anomalous relaxation on a fractal structure exhibits *CC* behavior. Therefore, one may assume that the memory function (5.89) has its origin in the geometrical self-similarity of the investigated system. Thus, the scaling parameter N is actually the number of points where the relaxing units are interacting with the statistical reservoir (i.e. by the ergodic assumption - the

number of relaxation acts on a microscopic level for a cooperative domain). The assumption of geometrical self-similarity of the considered system suggests that this number is

$$N = G\left(\frac{R}{R_0}\right)^{d_G} \quad . \tag{5.92}$$

Here, d_G is a spatial fractal dimension of the point set where relaxing units are interacting with the surroundings. R is the size of a sample volume section where movement of one relaxing unit occurs. R_0 is the cutoff size of the scaling in the space or the size of the cooperative domain. G is a geometrical coefficient about unity, which depends on the shape of the system heterogeneity. For example, the well-known two-dimensional recurrent fractal Sierpinski carpet has $d_G = \ln(8)/\ln(3) \approx 1.89,\ G = \sqrt{3}/4 \approx 0.43$ [213].

The relaxation process may be accompanied by a diffusion act. Consequently, the mean relaxation time for such kinds of disordered systems is the time during which the relaxing microscopic structural unit would move a distance R. The Einstein-Smoluchowski theory [226,235] gives the relationship between τ and R as

$$R^2 = 2d_E D\tau \quad , \tag{5.93}$$

where D is the diffusion coefficient and d_E is the Euclidean dimension. Thus, combining the relationships (5.90)-(5.93) one can obtain the relationship between the Cole-Cole parameter α and the mean relaxation time τ in the form

$$\alpha = \frac{d_G}{2}\frac{\ln(\tau\omega_s)}{\ln(\tau/\tau_0)} \quad , \tag{5.94}$$

where $\omega_s = 2d_E G^{2/d_G}\dfrac{D}{R_0^2}$ is the characteristic frequency of the diffusion process. This equation establishes the relationship between the *CC* exponent α, the relaxation time τ, the geometrical properties (fractal dimension d_G), and the diffusion coefficient (through ω_s).

5.7.2 Polymer-water mixtures

The first mention of the $\alpha(\tau)$ dependencies was in the experimental work [265]. The dielectric relaxation data of water in the mixtures of seven water-soluble polymers was presented there. It was found that in all these solutions relaxation of water obeys the *CC* law, while the bulk water exhibits the well-known Debye-like pattern [270,271]. Another observation was that α is dependent not only on the concentration of solute but also on the hydrophilic (or hydrophobic) properties of the polymer. The seven polymers were: poly(vinylpyrrolidone) (*PVP*; weight average molecular weight (Mw) = 10,000), poly(ethylene glycol) (*PEG*; Mw = 8,000), poly(ethylene imine) (*PEI*; Mw = 500,000), poly(acrylic acid) (*PAA*; Mw = 5,000), poly(vinyl methyl ether) (*PVME*; Mw = 90,000), poly(allylamine) (*PAlA*; Mw = 10,000), and poly(vinyl alcohol) (*PVA*; Mw = 77,000). These polymers were mixed with different ratios (up to 50% of polymer in solution) to water and measured at a constant room temperature (25°C) [265].

We would like to sketch a recent application [46] of model (5.94) to these systems. In Figure 52 the experimental dependencies of *CC* exponent α versus τ together with the fitting curve are presented. The values of the fitting parameters are listed in Table 3.

Table 3. The space fractional dimension d_G, the cutoff time of the scaling in the time domain τ_0, the characteristic frequency ω_s and estimated self-diffusion coefficient for the polymer water mixtures[b].

Sample	d_G	τ_0 [ps]	$\omega_s \times 10^{-11}$ [Hz]	$D\times 10^{9}$ [m^2s^{-1}]
PVA	1.56±0.09	7.18±0.74	1.47±0.21	3.31
PAlA[b]	1.43	6.46	1.74	3.92
PAA	1.12±0.17	6.34±0.83	2.08±0.68	4.68
PEI	1.33±0.02	4.89±0.45	2.67±0.40	6.01
PEG	1.54±0.04	4.45±0.74	2.78±0.63	6.26
PVME	1.38±0.10	3.58±1.23	4.24±2.47	9.54
PVP	1.00±0.01	0.79±0.11	127±34	286

[b]For the sample *PAlA* there are only three experimental points. For this reason it is impossible to determine the mean square deviation value and consequently the confidence intervals for the fitting parameters. Source: (Reproduced with permission from Ref. 46. Copyright 2002, American Institute of Physics.

It is well known [54,270] that the macroscopic dielectric relaxation time of bulk water (8.27ps at 25°C) is about ten times greater than the microscopic relaxation time of a single water molecule, which is about one hydrogen bond lifetime [206,272-274] (about 0.7 ps). This fact follows from the associative structure of bulk water where the macroscopic relaxation time reflects the cooperative relaxation process in some cluster of water molecules.

In the framework of the model presented above the microscopic relaxation time of water molecule is equal to the cut off time of the scaling in time domain τ_0.

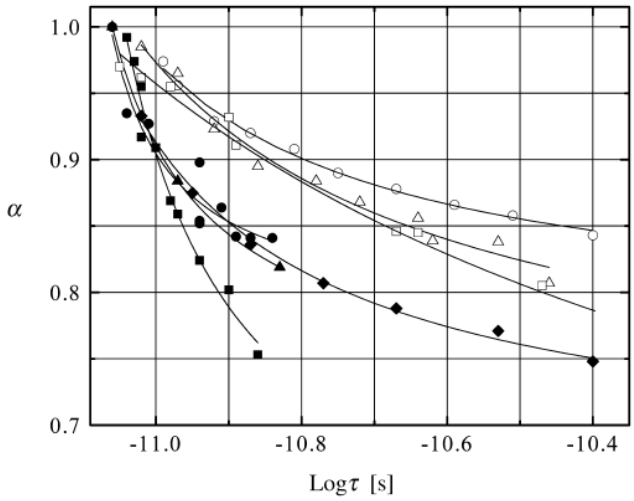

Figure 52. Cole–Cole exponent α versus relaxation time τ for *PVA* (●), *PAlA* (▲), *PAA* (■), *PEI* (♦), *PEG* (○), *PVME* (Δ), and *PVP* (□) samples. The curves correspond to the model described in this section. The filled symbols correspond to the hydrophilic polymers and the open symbols correspond to the hydrophobic samples. (Reproduced with permission from Ref. 2. Copyright 2002, Elsevier Science B.V.)

For the most hydrophilic polymer, *PVA*, the strong interaction between the polymer and the water molecule results in the greatest value of microscopic relaxation time τ_0, only 10% less than the macroscopic relaxation time of the bulk water. The most hydrophobic polymer, *PVP*, has the smallest value of a single water molecule microscopic relaxation time, which is almost equal to the microscopic relaxation time of bulk water (see Table 3). Therefore, weakening the hydrophilic properties (or intensifying the hydrophobic properties) results in a decreasing of interaction between the water and the polymer and consequently in the decrease of τ_0.

The interaction between the water and the polymer occurs in the vicinity of the polymer chains and only the water molecules situated in this interface are affected by the interaction. The space fractal dimension d_G in this case is the dimension of the macromolecule chain. If a polymer chain is stretched as a line, then its dimension is 1. In any other conformation, the

wrinkled polymer chain has a larger space fractal dimension, which falls into the interval $1 < d_G < 2$. Thus, it is possible to argue that the value of the fractal dimension is a measure of polymer chain meandering. Straighter (probably more rigid) polymer chains have d_G values close to 1. More wrinkled polymer (probably more flexible) chains have d_G values close to 2 (see Table 3).

The presence of a polymer in the water affects not only the relaxation but the diffusion of the solvent as well. For an estimation of the diffusion coefficient, we can use the following expression

$$D \cong \frac{\omega_s R_0^2}{2 d_E} \quad , \tag{5.95}$$

which is directly derived from the definition of the characteristic frequency ω_s. It was assumed in this last expression that the geometrical factor $G=1$. In our case the scaling cut-off size in space is equal to the diameter of a water molecule $R_0 \approx 3$ Å [52]. The Euclidean dimension of the space where diffusion occurs is the nearest integer number greater than the fractal dimension. Thus, $d_E = 2$. The results of this estimation are in Table 3. The diffusion coefficient for bulk water [52] at 25°C is $2.57 \cdot 10^{-9}$ $m^2 s^{-1}$. The presence of a polymer in the water prevents clusterization of water and relieves the diffusion. However, the strong interaction between polymer and water for hydrophilic samples slows down the diffusion. The competition between these two effects leads to the clear tendency of the diffusion coefficient to increase with an increase of hydrophility (see Table 3).

Note that the polymer affects only water molecules situated in the vicinity of the polymer chains. Thus, the estimated diffusion coefficient corresponds only to these water molecules and is not dependent on the polymer concentration. The averaged self-diffusion coefficient estimated for the entire polymer-water mixture should be different depending on the polymer concentration.

5.7.3 Micro-composite material

Another example of an application of Eq. (5.94) is on micro-composite polymer materials. We have performed dielectric measurements of the glass transition relaxation process in a Nylon 6,6 sample quenched in amorphous (*QN*), a crystalline nylon 6,6 sample (*CN*) and a micro-composite sample (*MCN*), which is the same crystalline nylon 6,6 but with incorporated kevlar fibers [275,276].

The quantitative analysis of the dielectric spectra of the glass-transition process was carried out by fitting the isothermal dielectric loss data according to the *HN* law (2.21). It was found from the fitting that β=1 for the glass-transition process in all of the samples measured. The glass-transition relaxation process in these systems is due to the motion of a polymer chain that is accompanied by a diffusion act. In general, the diffusion of a polymer chain is more complex than the Brownian model for diffusion [277,278]. However, in all the models the dependence of $<R^2>$ on time t is linear in the time scales associated with a monomeric link and in the time scale associated with the mobility of the entire chain. For this particular example, Eq. (5.93) describes the mobility of the polymer groups at the microscopic levels, i.e. at the scale of a monomeric link.

The experimental α versus τ dependencies for these samples, together with the fitting curves, are shown in Figure 53. Note that in contrast with the previous example these data are obtained at a constant sample composition. In this case, variations of parameters α and τ are induced by temperature variation. As mentioned above, the exponents α as well as the relaxation time τ are the functions of the different experimentally controlled parameters. The same parameters can affect the structure or the diffusion simultaneously. In particular, both α and τ are functions of temperature.

Thus, the temperature dependence of the diffusion coefficient in (5.93) should be considered. Let us consider the temperature dependence of the diffusion coefficient D

$$D = D_0 K(T) \ , \tag{5.96}$$

where $K(T)$ is a dimensionless function that represents the temperature dependence of the diffusion coefficient. D_0 is the appropriate constant with dimensions [$m^2 s^{-1}$]. An increase of the diffusion

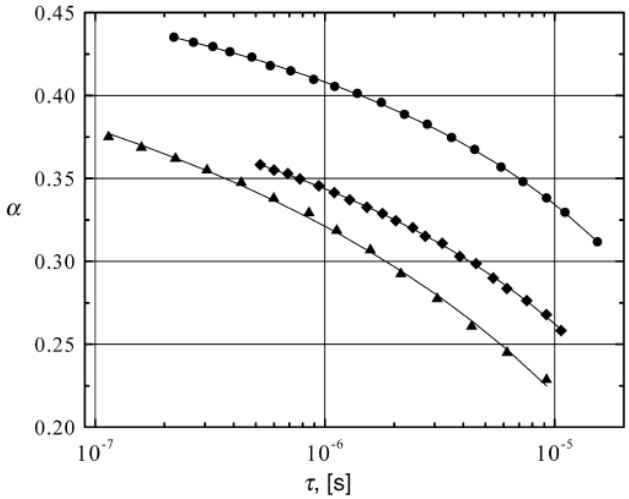

Figure 53. The dependence of α versus relaxation time τ for *QN* (●), *CN* (▲), and *MCN* (♦) samples. The curves correspond to the model described in this section. (Reproduced with permission from Ref. 2. Copyright 2002, Elsevier Science B.V.)

coefficient with increasing temperature also signifies an increase of the characteristic spatial scale R_0 (cut-off size of the scaling in the space). Let us assume that R_0^2 is proportional to the diffusion coefficient *D* and obeys the Einstein Smoluchowski theory

$$R_0^2 = 2d_E D\,\tau_{max} \quad , \tag{5.97}$$

where τ_{max} is the long-time limit of the scaling. Thus, combining together (5.96) and (5.97) with (5.91)-(5.93) we can obtain the relationship between the *CC* exponent α and relaxation time τ in a form similar to (5.94)

$$\alpha = \frac{d_G}{2}\frac{\ln(\tau\omega_0)}{\ln(\tau/\tau_0)} \quad , \tag{5.98}$$

with substitution of ω_s by $\omega_0 = \dfrac{G^{2/d_G}}{\tau_{max}}$. The latter relationship shows that under assumption (5.97) the temperature dependence of the diffusion coefficient does not change the form of the α versus τ relationship.

The average length of a nylon 6,6 polymer chain is about 50-100 μm (each polymer chain contains about 10^5 groups while the length of a polymer group r_g is about 10 Å). This length is comparable to the thickness of a sample 120-140 μm [275]. Thus, the movement of the chains is most likely occurring in the plane of the sample. This fact correlates with the values

of the space fractional dimension d_G. For all of the samples $d_G \in (1, 2)$ (see Table 4). Thereby, the Euclidean dimension of the space in which chain movement occurs is $d_E = 2$.

Table 4. The space fractional dimension d_G, the cutoff time of the scaling in the time domain τ_0 and the characteristic frequency ω_0 for quenched polymer (*QN*), crystalline (*CN*) and micro-composite samples (*MCN*). *Source*: Reproduced with permission from Ref. 2. Copyright 2002, Sage Publications.

Sample	d_G	τ_0 [ms]	ω_0 [kHz]
QN	1.12±0.01	1.1±0.1	5.9±0.3
CN	1.20±0.05	5.8±4.4	9.7±1.9
MCN	1.04±0.02	1.5±0.4	8.1±0.7

Although there is no unambiguous data for the mesoscale structure of the samples under investigation at this time, nevertheless it is possible to estimate the order of magnitude of some physically significant quantities from the cutoff time τ_0 and characteristic frequency ω_0 values. Despite the fact that ω_0 and ω_s have different physical significance, for the estimation one can neglect the temperature dependence of the diffusion coefficient and assume that $R_0^2 \approx 10^{-16}$ m^2 (R_0 is the cube root of the volume occupied by one polymer chain), $G \approx 1$. Then, the self-diffusion coefficient evaluated by expression (5.15) falls into the interval 10^{-14} to 10^{-13} m^{2}s^{-1}, which is typical for such polymer materials [279-281].

The cutoff time τ_0 is related to the size of the cooperative domain l_c by $l_c^2 = 4D\tau_0$. Thus, in the two-dimensional case one can estimate the number of polymer groups, n_g in the cooperative region as $n_g = l_c^2 / r_g^2 \approx 10^2$, which is in fair agreement with the results obtained in the paper [282].

One can also see from Table 4 that the presence of either the crystalline phase or the kevlar fibers in a sample leads to an increase of the cutoff time τ_0, indicating a slowdown of the relaxation process. Their presence also leads to an increase of the ω_0 value as well. This is a manifestation of a decreasing mobile polymer chain length.

Concluding this section we can summarize as follows: the model of symmetric relaxation peak broadening presented here is not universal. However, it was illustrated through two examples that this model can describe some common features of relaxations of this type. Thought, not a universal model, it, nevertheless, provides the relationship between

microscopic parameters of experimental samples and properties of experimentally measured macroscopic correlation functions. Thus, we hope that it may be useful in other cases where a dielectric relaxation of the Cole-Cole type is present.

6 Summary

In conclusion, we would like to recapitulate the main goals of this tutorial. We demonstrated the effectiveness of dielectric spectroscopy as a tool for investigating complex materials. The unique capabilities of *DS* allowed us to investigate materials in a broad time scale range, to identify general relaxation phenomena and to discover new ones for the studied complex systems, independent of the particularity of the material. *DS* makes it possible to cover extremely wide continuous ranges of experimentally controlled parameters, a feature that no other existing spectroscopic method today can offer. Moreover, this method, once again as compared to the conventional radio spectroscopic techniques such as electron paramagnetic or nuclear magnetic resonance, is much simpler in terms of hardware realization. We also presented current state-of-the-art applications of *DS* including the resolution of some of the critical issues related to hardware and modern data treatment procedures, which make possible the recent achievements of this method. Last, but not least, in this tutorial we discussed some contemporary ideas that are currently employed by the dielectric community. In this regard the *DS* studies of different complex materials presented in this tutorial demonstrate the capability to generate new knowledge about the cooperative dynamics in quite different complex structures [283-286]. It was shown that despite the morphological differences of the systems studied, the most general feature of the relaxation processes observed by *DS* is the Non-Debye Dielectric Response, which is a consequence of the cooperative dynamics and confinement that also lead to Non-Arrhenius kinetics.

7 Acknowledgements

We would like to thank Alexander Puzenko, Anna Greenbaum and Paul Ben Ishai from Department of Applied Physics, The Hebrew University of Jerusalem, Israel for numerous discussions and stimulating advice.

8 References

1. M.F. Shlesinger, G.M. Zaslavsky, and J. Klafter, *Nature* **363**, 31 (1993).
2. Yu. Feldman, A. Puzenko and Ya. Ryabov, *Chem. Phys.* **284**, 139 (2002).
3. F. Kremer and A. Schönhals, eds., *Broadband Dielectric Spectroscopy,* Springer-Verlag, Berlin, 2003.
4. R.N. Clarke, ed., *A Guide to the characterization of dielectric materials of RF and microwave frequencies*, NPL, London, 2004.
5. Yu. Feldman, I. Ermolina, and Y. Hayashi, *IEEE Trans. Dielectr. Electr.Insul.* **10**, 728 (2003).
6. H. Fröhlich, *Theory of dielectrics. Dielectric constant and Dielectric Loss* second edition, Clarendon Press, Oxford, 1958.
7. C.J.F. Böttcher, *Theory of Electric Polarization*, vol. 1, second edition, Elsevier Science B.V., Amsterdam, 1993.
8. N.E. Hill, W.E. Yaughan, A. H. Price and M. Davis, *Dielectric Properties and Molecular Behavior,* Van Nostrand, London, 1969.
9. N. Kozlovich, A. Pusenko, Yu. Alexanadrov, and Yu. Feldman, *Colloids and Surfaces A.* **140**, 229 (1998).
10. A. Volmari and H. Weingärtner, *J. Mol. Liq.* **98–99**, 293 (2002).
11. J.F. Böttcher and P. Bordewijk, *Theory of Electric Polarisation*, vol. 2, second edition, Elsevier Science B.V., Amsterdam, 1992.
12. B.K.P. Scaife, *Principles of Dielectrics*, Oxford University press, Oxford, 1989.
13. A.N. Tikhonov and V.Y. Arsenin, *Solutions of Ill-Posed Problems*, J. Wiley, New York, 1977.
14. H. Schäfer, E. Sternin, R. Stannarius, M. Arndt and F. Kremer, *Phys. Rev. Let.* **76**, 2177 (1996).
15. S. Havriliak and S. Negami, *J. Pol. Sci.: Part C* **14**, 99 (1966).
16. K.S. Cole and R.H. Cole, *J. Chem. Phys.* **9**, 341 (1941).
17. D.W. Davidson and R.H. Cole, *J. Chem. Phys.* **19**, 1484 (1951).
18. A.K. Jonscher, *Dielectric Relaxation in Solids,* Chelsea Dielectric press, London, 1983.
19. A.K. Jonscher, *Universal Relaxation Law,* Chelsea Dielectric Press, London, 1996.
20. J.C. Dyre and T.B. Schrøder, *Rev. Mod. Phys.* **72**, 873 (2000).
21. N.F. Mott and E.A. Davis, *Electronic Processes in Non-Crystalline Materials*, Clarendon Press, Oxford, 1978.

22. R.R. Nigmatullin and Ya.E. Ryabov, *Phys. Solid State* **39**, 87 (1997).
23. L. Nivanen, R. Nigmatullin and A. LeMehaute, *Le Temps Irreversible a Geometry Fractale*, Hermez, Paris, 1998.
24. S. Alexander, J. Bernasconi, W.R. Schneider and R. Orbach, *Rev. Mod. Phys.* **53**, 175 (1981).
25. M. Ben-Chorin, F. Möller, F. Koch, W. Schirmacher and M. Eberhard, *Phys. Rev. B* **51**, 2199 (1995).
26. W.T. Coffey, *J. Mol. Liq.* **114**, 5 (2004).
27. G. Williams, *Chem. Rev.* **72**, 55 (1972).
28. R.H. Cole, in: *Molecular Liquids NATO ASI Ser. C* **135**, 59 (1984).
29. R. Kohlrausch, *Ann. Phys.* **12**, 393 (1847).
30. G. Williams and D.C. Watts, *Trans. Farad. Soc.* **66**, 80 (1970).
31. R. Metzler and J. Klafter, *Phys. Rep.* **339**, 1(2000).
32. A. Blumen, J. Klafter and G. Zumofen, in: I. Zschokke (Ed.) *Optical Spectroscopy of Glasses*, Reidel, Dordrecht, Netherlands, p. 199, 1986.
33. G.H. Weiss, *Aspects and Applications of the Random Walk*, North-Holland, Amsterdam, 1994.
34. E. Barkai, R. Metzler and J. Klafter, *Phys. Rev. E* **61**, 132 (2000).
35. T. Zavada, N. Südland, R. Kimmich and T.F. Nonnenmacher, *Phys. Rev. E* **60**, 1292 (1999).
36. R. Kimmich, *Chem. Phys.* **284**, 253(2002).
37. T. Wadayama, S. Yamamoto and A. Hatta, *Appl. Phys. Lett.* **65**, 1653 (1994).
38. V. Degiorgio, R. Piazza, F. Mantegazza and T. Bellini, *J. Phys.: Condens. Matter* **2**, SA69 (1990).
39. J.E. Martin, D. Adolf and J.P. Wilcoxon, *Phys. Rev. A* **39,** 1325 (1989).
40. A. Bello, E. Laredo and M. Grimau, *Phys. Rev. B* **60,** 12764 (1999).
41. F. Alvarez, A. Alegría, J. Colmenero, *Phys. Rev. B* 44, 7306 (1991).
42. G. Katana, E.W. Fischer, Th. Hack, V. Abetz and F. Kremer, *Macromolecules* **28**, 2714 (1995).
43. R.V. Chamberlin, *Phys. Rev. Lett.* **82**, 2520 (1998).
44. K. Weron and A. Klauzer, *Ferroelectrics* **236**, 59 (2000).
45. *Application of Fractional Calculus in Physic*s, edited by R. Hilfer, World Scientific, Singapore, 2000.

46. Y.E. Ryabov, Y. Feldman, N. Shinyashiki and S. Yagihara *J. Chem. Phys.* **116**, 8610 (2002).
47. Yu. Feldman, N. Kozlovich, Y. Alexandrov, R. Nigmatullin and Y. Ryabov, *Phys. Rev. E.* **54** 5420 (1996).
48. S. Arrhenius, *Z. Physik. Chem.* **4**, 226 (1889).
49. H. Eyring, *Chem. Rev.* **17**, 65 (1935).
50. H. Eyring, *J. Chem. Phys.* **3**, 107 (1935).
51. H. Eyring, *Trans. Faraday. Soc.* **34**, 41 (1938).
52. D. Eisenberg and W. Kauzmann, *The structure and Properties of Water*, Clarendon, Oxford, 1969.
53. J. Barthel, R. Buchner and B. Wurm, *J. Mol. Liq.* **98-99**, 51 (2002).
54. R. Buchner, J. Barthel and J. Stauber, *Chem. Phys. Lett.* **306**, 57 (1999).
55. C.A. Angell, *J. Non-Cryst. Solids* **73**, 1 (1985).
56. C.A. Angell, *J. Non-Cryst. Solids* **131-133**, 13 (1991).
57. R. Böhmer, K.L. Ngai, C. A. Angell and D. J. Plazek, *J. Chem. Phys.* **99**, 4201 (1993).
58. R. Richert and C.A. Angell, *J. Chem. Phys*. **108**, 9016 (1998).
59. R. Brand, P. Lunkenheimer and A. Loidl, *J. Chem. Phys*. **116**, 10386 (2002).
60. H. Vogel, *Physik. Z.* **22**, 645 (1921).
61. G.S Fulcher, *J. Am. Ceram. Soc.* **8**, 339 (1925).
62. G.Tammann and W. Hesse, *Z. Anorg. Allg. Chem.* **156**, 245 (1926).
63. G. Adam and J. H. Gibbs, *J. Chem. Phys.* **43**, 139 (1965).
64. W. Kauzmann, *Chem. Rev.* **43**, 219 (1948).
65. C.A. Angell, *Chem. Rev.* **102**, 2627 (2002).
66. T.G. Fox and P. J. Flory, *J. App. Phys.* **21**, 581 (1950).
67. T.G. Fox and P. J. Flory, *J. Phys. Chem.* **55**, 221 (1951).
68. T.G. Fox and P. J. Flory, *J. Pol. Sci.* **14**, 315 (1954).
69. A.K. Doolittle, *J. App. Phys.* **22**, 1471 (1951).
70. D. Turnbull and M.H. Cohen, *J. Chem. Phys.* **34**, 120 (1961).
71. J.T. Bendler and M.F. Shlesinger, *J. Mol. Liquids* **36**, 37 (1987).
72. J.T. Bendler, M.F. Shlesinger, *J. Stat. Phys.* **53**, 531 (1988).
73. J.T. Bendler, J.J. Fontanella and M.F. Shlesinger, *Phys. Rev. Lett.* **87**, 195503 (2001).
74. W. Götze and L. Sjögren, *Rep. Prog. Phys.* **55**, 241 (1992).
75. U. Bengtzelius, W. Götze and A. Sjölander, *J. Phys. C: Solid State Phys.* **17**, 5915 (1984).
76. P. Taborek and R.N. Kleiman, D.J. Bishop, *Phys. Rev. B* **34**, 1835 (1986).

77. R. Richert and H. Bässler, *J. Phys.: Condens. Matter* **2**, 2273 (1990).
78. Y.E. Ryabov, A. Puzenko and Yu. Feldman, *Phys. Rev B.* **69**, 0142041 (2004).
79. R.H. Cole, J.G. Berberian, S. Mashimo, G. Chryssikos, A. Burns and E. Tombari, *J. Appl. Phys*. **66**, 793 (1989).
80. V.L. Odivanov, Yu.A. Gusev, *The journal Pribory i tekhnika eksperimenta*, **6**, 114 (1986).
81. J.G. Berberian and E. King, *J. Non.-Crys. Solids*, **305**, 10 (2002).
82. S. Mashimo, T. Umehara, T. Ota, S. Kuwabara, N. Shinyashiki and S. Yagihara, *J. Molec. Liq.* **36**, 135 (1987).
83. D. Bertolini, M. Cassettari, G. Salvetti, E. Tombari and S. Veronesi, *Rev. Sci. Instrum.* **62**, 450 (1991).
84. R. Nozaki and T. K. Bose, *IEEE Trans. Instrum. Meas.* **39**, 945 (1990).
85. B. Gestblom, E. Noreland and J. Sjöblom, *J. Phys Chem.* **91**, 6329 (1987).
86. Yu. Feldman, A. Andrianov, E. Polygalov, I. Ermolina, G. Romanychev, Yu. Zuev and B. Milgotin, *Rev. Sci. Instrum.* **67**, 3208 (1996).
87. A. Schönhals, F. Kremer and E. Schlosser, *Phys. Rev. Lett.* **67**, 999 (1991).
88. U. Kaatze, V. Lonneckegabel and R. Pottel, *Zeitschrift Fur Physikalische Chemie-International Journal of Research in Phys.* **175**, 165 (1992).
89. V.L. Odivanov, L.M. Ismagilov, R.M. Shagiev, Yu.A. Gusev, *The journal Phizicheskoi khimii*, Vol. LXIII, **2**, 568 (1989).
90. F. Kremer, D. Boese, G. Meier, E.W. Fischer, *Prog Colloid Polym Sci* **80**,129 (1989).
91. U. Kaatze and K. Giese *J.Phys.E: Sci Instrum* **13**,133 (1980).
92. R. Böhmer, M. Maglione, P. Lunkenheimer and A. Loidl, *J. Appl. Phys.* 65, 901 (1989).
93. J.R. Birch, and T.J. Parker, *Dispersive Fourier Transform Spectroscopy* Chapter 3 in K.J. Batton (Ed) *Infrared and Millimeter Waves* Vol. 2: Instrumentation" Academic Press, NY, pp.137-271, 1979.
94. H.P. Schwan, *Determination of biological impedances.* In: W.L. Nastuk, editor. *Physical techniques in biological research,* vol. VI. New York: Academic Press; p. 323–407. Part B. 1963.
95. K. Asami, *Prog. Polym. Sci.* **27**, 1617 (2002).
96. E.H. Grant, R.J Sheppard and G.P. South *Dielectric Behavior of Biological Molecules in Solution*, Oxford: Oxford University Press, chapter 3, 1978.
97. R.E. Collin *Foundations for microwave engineering*, 2nd dn. McGraw-Hill, NY 1966.
98. F. Kremer *J.Non.-Crys.Solids* **305**, 1 (2002).

99. F.I. Mopsic, *Rev. Sci. Instrum.* **55**, 79 (1984).
100. R. Richert, *Rev. Sci. Instrum.* **67**, 3217 (1996)
101. R. Richert, *Physica A* **287**, 26 (2000).
102. R. Richert, *J.Non.-Crys.Solids*, **305**, 29 (2002).
103. Yu.D. Feldman, Yu.F. Zuev, E.A. Polygalov and V.D. Fedotov, *Colloid & Polymer Science* **270**, 768 (1992).
104. B. Gestblom and P. Gestblom, *Macromolecules*, **24**, 5823 (1991)
105. R.H. Cole, *Dielectric Polarization and Relaxation*, in: NATO ASI Ser., Ser. C Vol. 135, "Molecular Liquids", 1984, p. 59-110.
106. Yu.D. Feldman and V.V. Levin, *Chem. Phys. Lett*, **85**, 528 (1982).
107. A.M. Bottreau and A. Merzouki, *IEEE Trans Instrum. Meas*. **42**, 899 (1993).
108. *Time Domain Measurements in Electromagnatics*, (E.K. Miller, ed.) Van Nostrand Reinhold Co, New York, 1986.
109. R. Nozaki and T.K. Bose, *IEEE Trans. Instrum. Meas.* **39**, 945 (1990).
110. N. Miura, N. Shinyashiki, S. Yagihara and M. Shiotsubo, *J. Amer. Ceramic. Soc.* **81**, 213 (1998).
111. R. Buchner and J. Barthel *Ber. Bun. Phys. Chem. Chem. Phys.* **101**, 1509 (1997).
112. N.E. Hager III, *Rev. Sci. Instrum*. **65**, 887 (1994).
113. Yu. Feldman, T. Skodvin and J. Sjöblom, *Dielectric Spectroscopy on Emulsion and Related Colloidal Systems-A Review* in Encyclopedic Handbook of Emulsion Technology, Marcel Dekker, Inc., New York, Basel, (2001), pp.109-168.
114. O. Göttmann, U. Kaatze and P. Petong, *Meas. Sci. Tech*. **7**, 525 (1996).
115. A. Oka, R. Nozaki and Y. Shiozaki, *Ferroelectrics* **230,** 459 (1999).
116. J.G. Berberian and R.H. Cole, *Rev. Sci. Instr.* **63**, 99 (1992).
117. J.P. Grant, R.N. Clarke, G.T. Symm and N.M Spyrou, *Phys. Med. Biol.* **33**, 607 (1988).
118. J.P. Grant, R.N. Clarke, G.T. Symm and N.M Spyrou, *J. Phys. E: Sci. Istrum.* **22**,757 (1989).
119. B. Gestblom, H. Førdedal and J. Sjöblom, *J. Disp. Sci. Tech.* **15**, 449 (1994).
120. T. Skodvin, T. Jakobsen and J. Sjöblom, *J. Disp. Sci. Tech.* **15**, 423 (1994).
121. G.Q. Jiang, W.H. Wong, E.Y. Raskovich, W.G. Clark, W.A. Hines and J. Sanny, *Rev. Sci. Instrum.* **64**, 1614 (1993).
122. T. Jakobsen and K. Folgerø, *Meas. Sci. Tech.* **8**, 1006 (1997).
123. Y.J. Lu, H.M. Cui, J. Yu and S. Mashimo, *Bioelectromagnetics*, **17**, 425 (1996).
124. S. Naito, M. Hoshi and S. Mashimo, *Rev. Sci. Instr.* **67**, 3633 (1996).

125. J.Z. Bao, S.T. Lu and W.D. Hurt, *IEEE Trans. Microw. Theory Tech.* **45**, 1730 (1997).

126. G. Bitton, Yu. Feldman, and A.J. Agranat, *J. Non.-Crys. Solids* **305**, 362 (2002).

127. T. Skodvin and J. Sjöblom, *Colloid Polym. Sci.*, **274**, 754 (1996).

128. M.S. Seyfried and M.D. Murdock, *Soil Science*, **161**, 87 (1996).

129. J.M. Anderson, C.L. Sibbald and S.S. Stuchly, *IEEE Trans. Microw. Theory Tech.* **42**, 199 (1994).

130. D.V. Blackham and R.D. Pollard, *IEEE Trans. Instrum. Meas.* **46**, 1093 (1997).

131. S. Jenkins, A.G.P. Warham, R.N. Clarke, *IEE Proc.-H Microw. Anten. & Prop.* **139**, 179 (1992).

132. N. Axelrod, E. Axelrod, A. Gutina, A. Puzenko, P. Ben Ishai, and Yu. Feldman, *Meas. Sci. Tech.* **15**, 755 (2004).

133. P.J. Verveer, M.J. Gemkow and T.M. Jovin, *J. Microsc.* **193**, 50 (1999).

134. M. Wübbenhorst, and J. van Turnhout, *J. Non. Crys. Solids*, **305**, 40 (2002).

135. G.A. Korn and T.M. Korn *Mathematical Handbook*, McGraw-Hill, New York, 1968.

136. F. Castro and B. Nabet, *J. Franklin Inst. B* **336**, 53 (1999).

137. B.G. Sherlock, *Signal Process.* **74**, 169(1999).

138. S.E. Friberg, *Microemulsions: Structure and Dynamics*, CRC Press, Boca Raton, Florida, 1987.

139. *Surfactants, Adsorption, Surface Spectroscopy and Disperse Systems.* (B. Lindman, ed.) Steinkopff, Darmstadt, 1985.

140. D. Langevin, *Annu. Rev. Phys. Chem.*, **43**, 341 (1992).

141. J. Sjöblom, R. Lindberg and S.E. Friberg, *Adv. Colloid Interface Sci.* **65**, 125 (1996).

142. M.A. van Dijk, G. Casteleijn, J.G.H. Joosten and Y.K. Levine, *J. Chem. Phys.* **85**, 626 (1986).

143. Yu. Feldman, N. Kozlovich, I. Nir and N. Garti, *Phys. Rev. E*. **51**, 478 (1995).

144. C. Cametti, P. Codastefano, P. Tartaglia, S.-H. Chen and J. Rouch, *Phys. Rev. A*, **45,** R5358 (1992).

145. F. Bordi, C. Cametti, J. Rouch, F. Sciortino and P. Tartaglia, *J. Phys. Condens. Matter* **8,** A19 (1996).

146. Yu. Feldman, N. Kozlovich, I. Nir and N. Garti, *Colloids Surfaces A* **128**, 47 (1997).

147. Yu. Feldman, N. Kozlovich, I. Nir, N. Garti, V. Archipov, Z. Idiyatullin, Y. Zuev and V. Fedotov, *J. Phys. Chem.* **100**, 3745 (1996).

148. A.L.R. Bug, S.A. Safran, G.S. Grest and I. Webman, *Phys. Rev. Lett.* **55** 1896 (1985).

149. N. Kozlovich, A. Puzenko, Yu. Alexandrov and Yu. Feldman, *Colloids and Surfaces A* **140**, 299 (1998).

150. G.S. Grest, I. Webman, S.A. Safran and A.L.R. Bug, *Phys. Rev. A* **33** 2842 (1986).

151. C. Cametti, P. Codastefano, A. Di Biasio, P. Tartaglia and S.-H. Chen, *Phys. Rev. A* **40**, 1962 (1989).

152. D. Stauffer and A. Aharony, *Introduction to Percolation Theory*, revised second edition, Taylor & Francis, London, 1994.

153. A. Gutina, E. Axelrod, A. Puzenko, E. Rysiakiewicz-Pasek, N. Kozlovich and Yu. Feldman, *J. Non-Cryst. Solids* **235-237**, 302 (1998).

154. A. Puzenko, N. Kozlovich, A. Gutina and Yu. Feldman, *Phys. Rev. B* **60**, 14348 (1999).

155. Ya. Ryabov, A. Gutina, V. Arkhipov and Yu. Feldman, *J. Phys. Chem. B* **105**, 1845 (2001).

156. A.Gutina, T. Antropova, E. Rysiakiewicz-Pasek, K. Virnik, and Yu. Feldman, *Microporous Mesoporous Matt.* **58**, 237 (2003).

157. A. Gutina, Ya. Haruvy, I. Gilath, E. Axelrod, N. Kozlovich and Yu. Feldman, *J. Phys. Chem. B,* **103**, 5454 (1999).

158. T.Saraidarov, E. Axelrod, Yu. Feldman and R. Reisfeld, *Chem. Phys. Lett.* **324**, 7 (2000).

159. M. Kraus, F. Kopinke and U. Roland, *Phys. Chem. Chem. Phys.*, **13**, 4119 (2011).

160. E. Axelrod, A. Givant, J. Shappir, Yu. Feldman and A. Sa'ar, *Phys. Rev. B* **65**, 165429 (2002).

161. E. Axelrod, A. Givant, J. Shappir, Yu. Feldman and A. Sa'ar, *J. Non-Cryst. Solids*, **305**, 235 (2002).

162. E. Rysiakiewicz-Pasek and K. Marczuk, *J. Porous Materials* **3**, 17 (1996).

163. M. Ben-Chorin, F. Moller and F. Koch, *Phys. Rev. B* **49**, 2981 (1994).

164. L.T. Canham, *Appl. Phys. Lett*. 57, 1046 (1990).

165. A.G. Cullis, L.T. Canham and P.D.J. Calcott, *J. Appl. Phys.* **82**, 909 (1997).

166. R. Hilfer, in: I. Prigogine and A. Rice (Eds.) *Advances in Chemical Physics*. Volume XCII, John Wiley, New York, 1996, p. 299.

167. Y. Lubianiker and I. Balberg, *Phys. Rev. Lett.* **78**, 2433 (1997).

168. J. Kočka, J. Oswald, A. Fejfar, R. Sedlačik, V. Železný, Ho The-Ha, K. Luterová and I. Pelant, *Thin solid Films* **276,** 187 (1996).

169. S. Triebwasser, *Phys. Rev.* **114**, 63 (1959).

170. Y. Girshberg and Y. Yacoby, *J. Phys. Condens. Matter* **13**, 8817 (2001).

171. R. Comes, R. Currat, F. Denoyer, M. Lambert and A.M. Quittet, *Ferroelectrics* **12**, 3 (1976).

172. Y. Yacoby, *Z. Phys. B* **31**, 275 (1978).

173. M.D. Fontana, G. Metrat, J.L. Servoin and F. Gervais, *J.Phys. C: Solid State Phys.* **17**, 483 (1984).

174. M.D. Fontana, H. Idrissi and K. Wojcik, *Europhys. Lett.* **11**, 419 (1990).

175. C.H. Perry, R.R. Hayes and N.E. Tornberg, in *Proceeding of the international conference on light scattering in solids*, 1975, edited by M. Balkansky, Wiley, New York, 1975, p. 812.

176. B.E.Vugmeister and M.D. Glinchuk, *Rev. Mod. Phys.* **62**, 993 (1990).

177. A.J. Agranat, V. Leyva and A. Yariv, *Opt. Lett.* **14**, 1017 (1989).

178. A.J. Agranat, in *Infrared Holography for Optical Communications*, Topics in Appl. Phys. 86, edited by P. Boffi, P. Piccinin and M.C. Ubaldi (Springer-Verlag, Berlin Heidelberg, 2003), p. 129.

179. P. Ben Ishai, C.E.M. de Oliveira, Y. Ryabov, Yu. Feldman and A.J. Agranat *Phys. Rev. B* **70**, 132104 (2004).

180. R. Hofineister, S. Yagi, A. Yariv and A.J. Agranat, *J. Cryst.Growth* **131**, 486 (1993)

181. I. Segal, E. Dorfman and O. Yoffe, *Atomic Spect.* **21**, 46 (2000).

182. O. Mishima and H.E. Stanley, *Nature* **396**, 329 (1998).

183. E. Donth, *The Glass Transition: Relaxation Dynamics in Liquids and Disordered Materials*; Springer-Verlag: Berlin, 2000.

184. K. Watanabe, T. Kawasaki, H. Tanaka, *Nature Materials*, **10**, 512 (2011).

185. N. Ito, W. Huang, R. Richert, *J. Phys. Chem. B*, **110** (9), 4371 (2006).

186. Ya.E. Ryabov, Y. Hayashi, A. Gutina and Yu. Feldman, *Phys. Rev. B*, **67**, 132202 (2003).

187. V.B. Koksheneva, P.D. Borges, N.S. Sullivan, *J. Chem. Phys.* **122**, 114510 (2005).

188. P. Lunkenheimer, A. Pimenov, M. Dressel, Yu. G. Goncharov, R. Böhmer and A. Loidl, *Phys. Rev. Lett.* **77**, 318 (1996).

189. P.G. Wolynes, V. Lubchenko, *Structural Glasses and Supercooled Liquids: Theory, Experiment, and Applications, First Edition*, John Wiley & Sons, Inc., 2012.

190. S. Sudo, M. Shimomura, N. Shinyashiki and S. Yagihara, *J. Non-Cryst. Solids* **307-310**, 356 (2002).

191. A. Van Hook, *Crystallization Theory and Practice*, Reinhold, New York, 1961.

192. Van Koningsveld, *Recl. Trav. Chim. Pays-Bas*. **87**, 243 (1968).
193. A. Schönhals, F.Kremer, A. Hofmann, E.W. Fischer, and E. Schlosser, *Phys. Rev. Lett.* **70**, 3459 (1993).
194. A.P. Sokolov, W. Steffen, and E. Rössler, *Phys. Rev. E* **52**, 5105 (1995).
195. P. Lunkenheimer and A. Loidl, *Chem. Phys.* **284**, 205 (2002).
196. H. Sillescu, *J. Non-Cryst. Solids* **243**, 81 (1999).
197. R. Richert, *J. Phys.-Cond. Matt.* **14**, R703 (2002).
198. *Handbook of Chemistry and Physics*, edited by R.C. Weast, CRC press, Cleveland, 1974.
199. F. Petrenko and R.W. Whitworth, *Physics of Ice*, Oxford University Press, Oxford, 1999.
200. P.V. Hobbs, *Ice Physics*, Clarendon Press, Oxford, 1974.
201. U. Schneider, R. Brand, P. Lunkenheimer and A. Loidl, *Phys. Rev. Lett.* **84**, 5560 (2000).
202. S. Hensel-Bielowka and M. Paluch, *Phys. Rev. Lett.* **89**, 025704 (2002).
203. S. Adichtchev, T. Blochowicz, C. Tschirwitz, V.N. Novikov and E.A. Rössler, *Phys. Rev. E*, **68**, 011504 (2003).
204. U. Kaatze, R. Behrends and R. Pottel, J. *Non-Cryst. Solids*, **305**, 19 (2002).
205. C. Rønne, L. Thrane, P.O. Astrand, A. Wallqvist, K.V. Mikkelsen and S.R. Keiding, *J. Chem. Phys*. **107**, 5319 (1997).
206. V. Arkhipov and N.Agmon, *Israel J. Chem. Phys*. **43**, 363 (2003).
207. G. P. Johari and M. Goldstein, *J. Chem. Phys.* **53,** 2372 (1970).
208. A. Puzenko, Y. Hayashi, Ya.E. Ryabov, I. Balin, Yu. Feldman, U. Kaatze and R. Behrends, *J. Phys. Chem. B.* **109**(12), 6031 (2005).
209. R.R. Nigmatullin, *Phys. Stat. Sol.* **153**, 49 (1989).
210. J. Klafter and A. Blumen, *Chem. Phys. Lett.* **119**, 377 (1985).
211. J. Klafter and M.F. Shlesinger, *Proc. Natl. Acad. Sci.* USA **83**, 848 (1986).
212. B.B. Mandelbrot, *The Fractal Geometry of Nature*, Freeman, New York, 1982.
213. E. Feder, *Fractals*, Plenum Press, New York, 1988.
214. U. Even, K. Rademann, J. Jortner, N. Manor and R. Reisfeld, *Phys. Rev. Lett.* **52**, 2164 (1984).

215. U. Even, K. Rademann, J. Jortner, N. Manor and R. Reisfeld, *Phys. Rev. Lett.* **58**, 285 (1987).
216. R.R. Nigmatullin, L.A. Dissado and N.N. Soutougin, J. Phys. D **25**, 32 (1992).
217. W.D. Dozier, J.M. Drake and J. Klafter, *Phys. Rev. Lett.* **56**, 197 (1986).
218. I. Webman, *Phys. Rev. Lett.* **47**, 1496 (1981).
219. T. Odagaki and M. Lax, *Phys. Rev. B*, **24**, 5284 (1981).
220. S. Havlin and A. Bunde, *Percolation II*, in *Fractals in disordered systems*, edited by A. Bunde and S. Havlin, Sprinder-Verlag Berlin Heidelberg, New York, 1996.
221. F. David, B. Duplantier and E. Guitter, *Phys. Rev. Lett.* **72**, 311 (1994).
222. G.A.Baker and N.Kawashima, *Phys. Rev. Lett.* **75**, 994 (1995).
223. F.F. Assaad and M. Imada, *Phys. Rev. Lett.* **76**, 3176 (1996).
224. K.B. Lauritsen, P. Fröjdh and M. Howard, *Phys. Rev. Lett.* **81**, 2104 (1998).
225. Yu. Alexandrov, N. Kozlovich, Yu.Feldman, and J. Texter, *J. Chem. Phys.* **111**, 7023 (1999).
226. P.K. Pathria, *Statistical Mechanics*, Pergamon Press, Oxford, 1972.
227. L.D. Landau and E.M. Lifshitz, *Statistical Mechanics*, Pergamon Press, Oxford, 1980.
228. Sh.K. Ma, *Statistical Mechanics*, World Scientific, Singapore, 1985.
229. D.N. Zubarev, *Nonequilibrium Statistical Thermodynamics*, Consultant Bureau, New York, 1974.
230. R.W. Zwanzig, in: W. E. Brittin, B. W. Downs and J. Downs (Eds.) *Lectures in Theoretical Physics*, Vol. III, Interscience Publishers, Inc., New York, 1996.
231. K. Oldham and J. Spanier, *The Fractional Calculus, Academic press*, New York, 1974.
232. K. Miller and B. Ross, *An Introduction to the Fractional Calculus and Fractional Differential Equations*, Wiley, New York, 1993.
233. H. Darcy, *Fontanies Publiques de la Ville de Dijon*, Libraire des Corps Imperiaux des Ponts et Chausses et des Mines, Paris, 1856.
234. J.B.J. Fourier, *Théorie analytique de la chaleur, Firmin Didot*, Père et Fils, Paris, 1822.
235. A. Einstein, *Ann. Phys.* **322**, 549 (1905).
236. E.W. Montroll and G.H. Weiss, *J. Math. Phys.* **6**, 167 (1965).
237. H. Scher and M. Lax, *Phys. Rev. B* **7**, 4491 (1973).
238. H. Scher and M. Lax, *Phys. Rev. B* **7**, 4502 (1973).
239. K.G. Wilson and J. Kogut, *Phys. Rep.* **2**, 75(1974).

240. Ya.E. Ryabov and A. Puzenko, *Phys. Rev. B,* **66**, 184201 (2002).

241. J. A. Padró, L. Saiz and E. Guàrdia, *J. Mol. Struct*. **416**, 243 (1997).

242. R. Podeszwa and V. Buch, *Phys. Rev. Lett.* **83**, 4570 (1999).

243. R. Mittal and I. A. Howard, *Phys. Rev. B* **53**, 14171 (1996).

244. Y. Hayashi, A. Puzenko, I. Balin, Y. E. Ryabov and Yu. Feldman, *J. Phys. Chem. B* **109**(18), 9174 (2005).

245. R.P. Auty and R.H. Cole, *J. Chem. Phys.* **20**, 1309 (1952).

246. N. Miura, Y. Hayashi, N. Shinyashiki and S. Mashimo, *Biopolymers*, **36**, 9 (1995).

247. C.T. Moynihan, P.B. Macedo, C.J. Montrose, P.K. Gupta, M.A. DeBolt, J.F. Dill, B.E. Dom, P.W. Drake, A.J. Easteal, P.B. Elterman, R.P. Moeller, H. Sasabe, J.A. Wilder, *Ann. N.Y. Acad. Sci.* **279,** 15 (1976).

248. Y. Hayashi, N. Miura, N. Shinyashiki, S. Yagihara and S. Mashimo, *Biopolymers*, **54**, 388 (2000).

249. S. Naoi, T. Hatakeyama and H. Hatakeyama, *J. Therm. Anal. Calorim.* **70**, 841 (2002).

250. R.D. Shannon, *Acta Cryst. A* **32**, 751 (1976).

251. K. Leung, *Phys. Rev. B* **65**, 012102 (2001).

252. L. Frunza, H. Kosslick, S. Frunza, R. Fricke and A. Schönhals, *J. Non-Cryst. Solids* **307**-**310**, 503 (2002).

253. L. Frunza, A. Schönhals, S. Frunza, V.I. Parvulescu, B. Cojocaru, D. Carriazo, C. Martín, and V. Rives, *J. Phys. Chem. A*, **111**(24), 5166 (2007).

254. A. Hushur, J.H. Ko, S. Kojima, S.S. Lee and M.S. Jang, *J. Appl. Phys.* **92**, 1536 (2002).

255. J.H. Ko and S. Kojima, *J. Korean Phys. Soc.* **41**, 241 (2002).

256. F. Cordero, A. Campana, M. Corti, A. Rigamonti, R. Cantelli and M. Ferretti, *Intl. J. Mod. Phys. B* **13**, 1079 (1999).

257. P. Ben Ishai, C.E.M. de Oliveira, Y. Ryabov, A.J. Agranat and Yu. Feldman, *J. Non-Cryst. Solids* **351**, 2786 (2005).

258. A. A. Bokov, M. Mahesh Kumar, Z. Xu and Z.-G. Ye, *Phys. Rev. B* 64, 224101 (2001).

259. G.P. Johari, A. Hallbruker and E. Mayer, *Nature* **330**, 552 (1987).

260. R.S. Smith and B.D. Kay, *Nature* **398**, 788 (1999).

261. J. Kakalios, R. A. Street, W. B. Jackson, *Phys. Rev. Lett.* **59**, 1037 (1987).

262. E.W. Fischer, E. Donth and W. Steffen, *Phys. Rev. Lett.* **68**, 2344 (1992).

263. J. Colmenero, A. Alegía, A. Arbe and B. Frick, *Phys. Rev. Let.* **69**, 478 (1992).

264. M. Salomon, M. Z. Xu, E.M. Eyring and S. Petrucci, *J. Phys. Chem.* **98**, 8234 (1994).

265. N. Shinyashiki, S. Yagihara, I. Arita and S. Mashimo, *J. Phys. Chem. B* **102**, 3249 (1998).

266. H. Mori, *Prog. Theor. Phys.* **33**, 423 (1965).

267. H. Mori, *Prog. Theor. Phys.* **34**, 399 (1965).

268. I.M. Sokolov, *Phys. Rev. E* **63**, 011104 (2001).

269. S. Fujiwara and F. Yonezawara, *Phys. Rev. E* **51**, 2277 (1995).

270. J.B. Hasted, in: F. Franks (Ed.) *Water, A Comprehensive Treaties*, Plenum Press New York, 1972, p. 255.

271. U. Kaatze, *J. Chem. Eng. Data* **34**, 371 (1989).

272. M.D. Fayer, *Acc. Chem. Res.* **45**(1), 3 (2012).

273. U. Kaatze, *J. Mol. Liq.* **56**, 95 (1993).

274. C. Rønne, P.-O Åstrad and S.R. Keiding, *Phys. Rev. Lett.* **82**, 2888 (1999).

275. H. Nuriel, N. Kozlovich, Yu. Feldman and G. Marom, *Composites: Part A* **31**, 69 (2000).

276. Y.E. Ryabov, G. Marom and Yu. Feldman, *J. Therm. Comp. Mat.* **17**, 463 (2004).

277. P.G. DeGennes, *J. Chem. Phys.* **55**, 572 (1971).

278. W.W. Graessley, *J. Polym. Sci.: Polym. Phys.* **18**, 27 (1980).

279. F. Joabsson, M. Nyden and K. Thuresson, *Macromolecules* **33**, 6772 (2000).

280. J.E.M. Snaar, P. Robyr and R. Bowtell, *Mag. Res. Im.* **16**, 587 (1998).

281. P. Gribbon, B.C. Heng and T.E. Hardingham, *Biophys. J.* **77**, 2210 (1999).

282. E. Donth, *J. Non-Cryst. Solids* **131-133**, 204 (1991).

283. Y. Feldman, A. Puzenko, and Ya. Ryabov, in *Advances in Chemical Physics*, edited by Y. P. Kalmykov,W. T. Coffey, and S. A. Rice (Wiley, New York, 2006), Vol. 133, Part A, p. 1.

284. A. Puzenko, P. Ben Ishai and Yu. Feldman, *Phys. Rev. Lett.*, 105, 037601 (2010).

285. E. Levy, A. Puzenko, U. Kaatze, P. Ben Ishai, and Yu. Feldman, *J. Chem. Phys.* **136**, 114502 (2012).

286. E. Levy, A. Puzenko, U. Kaatze, P. Ben Ishai, and Yu. Feldman, *J. Chem. Phys.* **136**, 114503 (2012).